Structural and Dynamical Correlations Linked to Smaller Thermal Resistance at a Classical Liquid/Solid Interface

Thesis by
Hiroki Kaifu

In Partial Fulfillment of the Requirements for the
Degree of
Doctor of Philosophy

CALIFORNIA INSTITUTE OF TECHNOLOGY
Pasadena, California

2024
Defended May 30, 2024

Hiroki Kaifu
ORCID: 0009-0003-2507-6810

ACKNOWLEDGEMENTS

Before anything else, I would like to express my greatest appreciation to Prof. Sandra M. Troian who invited me to join her research group, the Laboratory of Interstitial & Small Scale Transport (LIS^{2}T). Throughout the course of my graduate study, I have gained tremendous amount of knowledge on fluid dynamics, thermal transport, and molecular dynamics simulation from her. Furthermore, she has taught me how to formulate a scientific problem as a true professional scientist, and the importance of challenging conventional wisdom for a new frontier of science. Your invaluable insights, continuous encouragement, and sense of humor profoundly enriched my life at Caltech, and I cannot thank you enough for all that you have done for me.

I would also like to thank the rest of my thesis committee, Prof. Keith C. Schwab, Prof. Frank C. Porter, and Prof. Olexei I. Motrunich who have provided me with insightful comments from the perspectives outside of my field through inspiring conversations.

I would like to express my sincere appreciation to NASA for the financial support which allowed me not only to undergo professional training as a computational physicist but also to acquire deeper understanding of potential end applications of my work to various space technology efforts. This support also provided me with opportunities to attend wonderful conferences like those sponsored by the American Physical Society. I also wish to thank Dr. Artem I. Baskin, my assigned NASA mentor, who spent considerable time discussing with me the many interesting NASA-related problems involving space-related technologies like battery science and related interfacial phenomena.

I also thank my fellow colleagues, Dillon Chang and Cheolmin Im, for interesting discussions we had, and it was a joy to motivate each other through our lunch meetings, and for all the fun we have had together over the last four years. I'm also indebted to the system administrator of our lab, Dr. Peter A. Thompson, who devoted significant fraction of his time ensuring that computer hardware and software were always up-to-date and that database was properly backed up. Thanks to his technological assistance, my simulations on the computing cluster were greatly expedited.

Outside of academics, I am truly grateful to my parents Masaki and Yuko Kaifu who have provided me with unconditional moral, emotional, and financial support throughout my entire academic career. I would like to especially thank my mother with whom I have always shared good times and hard times. Her laughs and a sense of humor alleviated my stress more than a few times. My little sister Mayo Kaifu has been my good friend who helped me relieve intense stress through video games and other fun activities. My three feline friends Nicky, Cookie, and Pocky who always cheered me up whenever I was going through a tough time. It would not have been possible to conduct this Ph.D research without

their precious support. I'm also in debt to many other family members not mentioned here.

Last, but by no means the least, I would like to acknowledge my paternal grandfather Toshiki Kaifu, who served as the 77th prime minister of Japan and sadly passed away just two years ago. I know for sure that he would be proud of my accomplishment, and I will forever remember all the exciting times we played shogi (Japanese chess) together. Hence, this thesis is dedicated to you.

ABSTRACT

Ever more powerful and densely packed chips for applications like cryptocurrency mining and artificial intelligence generate such enormous heat fluxes that designers are pivoting from gas to liquid cooling to forestall damage from thermal runaway. Even with optimal flow patterns however, the intrinsic thermal boundary resistance at the liquid/solid (L/S) interface poses an additional source of thermal impedance. There is a lingering misconception in the field that the higher the liquid contact density, the more frequent the L/S collision rate and the smaller the thermal slip length. Here we present an insightful counterexample based on non-equilibrium molecular dynamics simulations of a classical liquid confined between different facets of a face centered cubic crystal held at different temperature. We have conducted a comprehensive study to quantify thermal exchange and propagation across the interface by varying the L/S interaction energy, L/S repulsive distance, facet orientation, thermal flux and local temperature with particular emphasis on the properties of the liquid contact layer (i.e., liquid monolayer adjacent to the solid surface). Numerous static and dynamic quantities characterizing the contact layer reveal the ways in which long range order, anisotropy of the L/S potential and correlated motion act to reduce the thermal slip length. Systems with the smallest thermal slip length exhibit two distinct features: 2D caged motion with string-like alignment of liquid particles unlike that observed in glassy systems and larger non-ergodicity parameter but shorter, not longer, caging times.

These simulations have revealed two master curves which help unify the various influences at play. The first relation directly links the thermal slip length to the temperature modified 2D static structure factor representing long-range order in the contact layer. The second relation directly links the thermal slip length to the temperature modified dominant frequencies of the first solid and liquid layer as extracted from the density of states. These correlations, which represent power law dependencies, offer a new paradigm for the design of L/S interfaces to maximize thermal exchange across a classical L/S interface.

PUBLISHED CONTENT AND CONTRIBUTIONS

1. Hiroki Kaifu, Sandra M. Troian and Artem Baskin, *How Caged Motion in the Contact Layer Enhances Thermal Tunneling Across a Liquid/Solid Interface*, to be published in Phys. Rev. Research (2024).

   Basis: The article is in large part based on the material in Chapter 2.

   Contribution: HK carried out the numerical simulations, collected and helped analyze the data, prepared figures and movies for distribution and provided material for the manuscript.

2. Hiroki Kaifu and Sandra M. Troian, *Dependence of the Thermal Slip Length on In-Plane Long-Range Order and Frequency Mismatch Across a Liquid/Solid Interface*, to be submitted for publication.

   Basis: The material in Chapter 4 forms the basis for this article.

   Contribution: HK carried out the numerical simulations, collected and helped analyze the data, prepared figures and movies for distribution and provided material for the manuscript.

3. Hiroki Kaifu and Sandra M. Troian, *Correspondence Between Small Thermal Slip Length, Bond-Orientational Order and Non-Gaussian Dynamics in the Contact Layer at a Liquid/Solid Interface*, to be submitted for publication.

   Basis: The material in Chapter 3 and some in Chapter 2 forms the basis for this article.

   Contribution: HK carried out the numerical simulations, collected and helped analyze the data, prepared figures and movies for distribution and provided material for the manuscript.

TABLE OF CONTENTS

LIST OF ILLUSTRATIONS

Number *Page*

LIST OF TABLES

Chapter 1

INTRODUCTION

1.1 Background

Phononic thermal transport through an interface between two dissimilar materials is undermined by a thermal jump ΔT which deteriorates the effective thermal gradient applied to the system. This thermal jump is known to result from the thermal boundary resistance (TBR) or Kapitza resistance defined as [30]

$$\mathcal{R} = \frac{J_z}{\Delta T} , \tag{1.1}$$

where J_z is a thermal flux in the direction normal to the interface. TBR is often considered to play critical roles in heat dissipation across the interface, especially when the system size is small. In analogue of the velocity slip length which describes the momentum transfer across a liquid/solid (L/S) interface, the characteristic length scale known as the thermal slip length L_T is often used to quantify TBR as follows:

$$L_T = k(T)\mathcal{R} = \frac{\Delta T}{\left|dT/dz\right|_{liq}} . \tag{1.2}$$

Here, $k(T)$ the local thermal conductivity and $|dT/dz|_{liq}$ is the thermal gradient in the bulk liquid region obeying the Fourier's law:

$$J_z = k(T) \left|\frac{dT}{dz}\right|_{liq} . \tag{1.3}$$

A simple illustration in Fig. 1.1 schematically shows that L_T is the distance within the solid where the linear extrapolation of the liquid temperature profile matches the solid temperature at the interface. Physically, the thermal slip length represents the thickness of a liquid film that covers the temperature difference equivalent to the thermal jump induced by TBR.

The newest generation of integrated chips for machine learning and artificial intelligence generate enormous power densities, so much so that the extraction of waste heat is now considered the limiting factor in information processing. Without rapid extraction of waste heat, densely packed chips easily malfunction from hot spot formation and subsequent thermal runaway. Early studies of heterogeneous bipolar transistors, for example, indicated how current or voltage instabilities generate thermal runaway from rapidly increasing junction temperatures [39]. For this reason, the newest generation of compact chips designed for power intensive applications such as data mining and machine learning require single phase

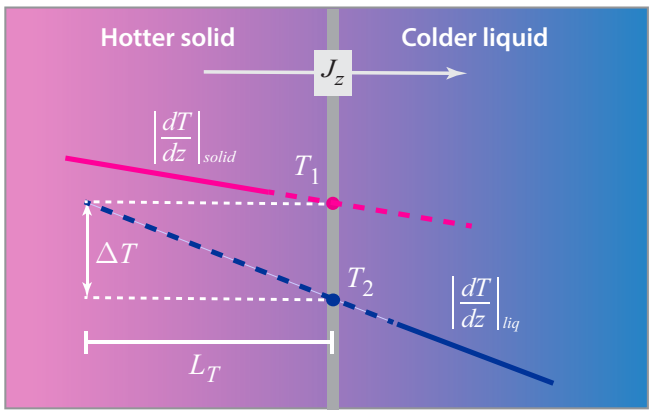

Figure 1.1: Schematic diagram (not drawn to scale) illustrating the definition of the thermal slip length [Eq. (1.2)]. With this definition, the extent of the interfacial region is intended to be infinitesimally small in comparison to the thickness of the adjacent solid and liquid layers.

liquid cooling. The switch from gas to liquid cooling [79], which relies on circulation of a coolant through a network of embedded microfluidic channels has proven fairly successful in this regard. Even for optimal circulation patterns, however, thermal extraction remains suboptimal due to the intrinsic thermal boundary resistance at the L/S interface, which must be overcome for optimal performance.

1.1.1 Predictions of thermal boundary resistance at cryogenic temperatures

Researchers long ago developed two main models for predicting TBR at cryogenic temperatures for systems in which phonons are the dominant heat carrier. The acoustic mismatch model (AMM) assumes specular reflection of phonons at the interface, somewhat akin to specular reflection of electromagnetic waves described by the Fresnel equations. This idealized model overestimates TBR in some systems by over two orders of magnitude, e.g., Fig. 1 in Ref. [69]. Interesting, it also predicts a finite value of TBR for two identical contacting media by virtue of the fact that the interface introduces a discontinuity [69]. The diffuse mismatch model (DMM), which tends to underestimate TBR, assumes all incident phonons undergo scattering at the interface. Generally then, the smaller the acoustic impedance mismatch of the two adjoining materials or the fewer number of surface defects, the smaller the degree of phonon scattering and the smaller the value $\mathcal{R}$, e.g., Fig. 14 in Ref. [69]. Both the AMM and DMM model suffer from the limitation that the input values to $\mathcal{R}$ rely exclusively on material constants characterizing the adjoining media and therefore don't incorporate consideration of the interfacial bonding energy or surface defects. Despite these shortcomings, however, at low temperatures below about 30 K, the predictions they yield offer reasonable estimates for solid/solid (S/S) systems when treated to minimize surface defects and pressed together tightly to minimize voids and asperities [70]. Closer to room temperature however, where inelastic phonon scattering and other surface effects

play a significant role, neither model provides a reliable estimate of $\mathcal{R}$. Researchers have recently introduced a "phonon model of thermodynamics," an equilibrium based concept able to predict with surprising accuracy over a wide range in temperature and pressure the specific heat of many liquids ranging from noble and metallic to hydrogen-bonded fluids [8]. Whether elements of this successful model can perhaps be extended to non-equilibrium systems maintaining a thermal gradient remains to be seen.

1.1.2 Necessity of non-equilibrium molecular dynamics simulations

There exist but a few experimental techniques for measuring TBR or L_T at interfaces in microscale systems due to limitations in resolution and restrictions on the thermal penetration depth of the heat source. Although improvements are underway to enhance measurement sensitivity of the thermal slip length at S/S [88] and L/S [91] interfaces, the latter is particularly challenging at non-cryogenic temperatures. Researchers have therefore come to rely heavily on particle-based simulation methods for quantifying thermal exchange across the L/S barrier. In particular, non-equilibrium molecular dynamics (NEMD) simulations are well poised to offer solutions to this challenge. The intermolecular potential of choice for a spherically symmetric two-body interaction of simple neutral particles is the Lennard-Jones (LJ) potential, which has allowed highly accurate predictions of thermophysical values for gaseous, liquid and solid argon. The LJ potential scales as $\varepsilon U(r/\sigma)$, where ε is the inter particle interaction energy, U is the potential function, r is the particle separation distance and σ is the approximate repulsive distance (sometimes called the particle diameter). According to the principle of corresponding states [24], the thermodynamic, structural and dynamic behavior of many other liquids and solids can also be modeled by the LJ potential by different choice of ε and σ - hence, the ubiquitous use of NEMD studies based on the LJ potential [24].

Early NEMD benchmark studies of a bulk homogeneous isotropic fluid confined between two unstructured walls at different temperature confirmed that thermal conduction within the interior liquid and solid is well described by Eq. (1.3) for fluid density, pressure and temperature ranging from gas-liquid coexistence to the freezing [71] point. With this finding established, researchers began exploring the influence of the L/S interaction energy ε_{LS} and repulsive distance on the degree of liquid density stratification near a wall, a layering phenomenon first detected in equilibrium systems [16, 25, 67]. The first and largest oscillation in the liquid density profile, which always occurs next to the wall, is known as the *contact layer* and its contact density ρ_c determined by the first liquid density peak immediately adjacent to the L/S interface. The value ρ_c should not be confused with the peak density of the contact layer, a local value signifying the maximum amplitude of the first oscillation. As is common, the separation distance between the peak density of the first solid and liquid layers is known as the depletion layer thickness. Subsequent studies unveiled numerous correlations between the thermal slip length in L/S systems and parameters such

as the LJ interaction energy [5, 42–44, 84, 90], liquid pressure [21, 50], wall surface temperature [3, 47], wall roughness [84], wall symmetry [51, 77], liquid thickness [33], spring constant used in popular wall-spring models [33] and more. During the last twenty years, NEMD simulations have been extended to the study of structured fluids including hydrogen bonded liquids and solids describing metal, dielectric and insulating material.

1.1.3 Importance of the contact layer

Somewhat analogous to the transmission and reflection of light at the boundary separating media of different refractive index, the L/S interface also plays a significant role in regulating the transmission and reflection of thermal energy. As first reported [5, 41], the stronger the L/S interaction energy, the smaller the thermal slip length but the mechanisms responsible for this connection are not well understood. Studies have since attributed this correspondence to an increase in the density of adsorptive/absorptive particles in the contact layer onto the solid surface [49, 53], which some have quantified by the contact density ρ_c [17, 21, 29]. Larger values of the contact density can be had by lowering the system temperature, increasing the liquid pressure or using a denser bulk fluid. It has also been reported in NEMD simulations of L/S systems consisting of water in contact with various orientations of solid silicon that a higher thermal boundary conductance (i.e., lower thermal boundary resistance) correlates closely with a smaller depletion layer thickness [59], which has been attributed to two possible effects. The higher the contact density ρ_c, the denser the first liquid layer and presumably the more frequent the collisions with the solid layer. Secondly, the smaller the depletion layer thickness, the stronger the influence of the corrugations in the solid surface potential, which presumably enhances thermal exchange. Motivated by such findings, NEMD studies have tended to focus on the amplitude, number and character of density oscillations representing the degree of liquid layering against a structured solid. In this work we focus almost exclusively on stationary and dynamic properties associated with the planar (2D) motion of particles within the contact layer. Subscripts c shall refer to particles in the contact layer and the symbol $\parallel$ to measurements associated with 2D motion in the plane defined by the L/S interface.

1.1.4 Frequency analysis of the interfacial thermal transport

It is common to explore the underlying mechanism of interfacial thermal transport across the L/S interface in view of vibrational modes. In particular, a classical model of phononic heat transfer (e.g., the acoustic mismatch model [32, 69]) suggests that there exists a correlation between TBR and overlap of density of states (the DOS; i.e., the number of vibrational modes distributed per unit frequency) of two dissimilar materials forming the interface. Strictly speaking, this picture is valid only at cryogenic temperatures where anharmonic modes are nearly non-existent so that phonon scattering at the interface is perfectly specular. Nevertheless, the concept of the DOS overlap is still widely used as a convenient tool

for understanding vibrational dynamics driving the interfacial thermal transport. Recent computational works have reported the correlation between the TBR and the DOS overlap not only for S/S interfaces [75, 87] but also for L/S interfaces [9, 18, 86, 93] even though phonon may not be a suitable as a picture of thermal energy carrier in liquids. In the meanwhile, several computational works reported that TBR at L/S interfaces is negligibly influenced by a degree of the DOS overlap [1, 83]. Therefore, there exists no universal agreement on the extent to which the phonon-based model is applicable to thermal conduction across the L/S interface.

1.2 Overview of our work

We preformed a series of NEMD simulations to investigate a correlation between TBR across the L/S interface and structural/dynamical properties characterizing the liquid layering at the interface. The simulations to be described are based on a simple monatomic liquid confined between two identical crystalline walls oriented along one of three facets and whose exterior boundaries are maintained at a given temperature difference. The quantities that were varied include the macroscopic temperature difference applied to the system, the energy and length parameters characterizing the L/S interaction potential, and the orientation of the crystal lattice comprising the solid substrates. The computational details and methods of analysis used to quantify various stationary and dynamic quantities are detailed in Section 1.3.

In Chapter 2, we first benchmark the system by showing how crystal facet orientation, L/S interaction energy and contact layer temperature influence stationary properties such as the liquid density profile, liquid contact density, temperature profiles, thermal flux and thermal slip length. We then examine features of the 2D (i.e., in-plane) radial distribution function and 2D static structure factor describing particle organization throughout the contact layer. This is followed by examination of the 2D and 3D velocity autocorrelation function, 2D mean square displacement and 2D self-intermediate scattering function. The discussion in Section 2.4 focuses on the main finding that a smaller thermal slip length correlates positively with a larger non-ergodicity parameter but shorter – not longer – caging time.

In Chapter 3, we first examine the vibrational modes that contribute to energy exchange between the liquid and solid particles by computing the spectral heat flux [Eq. (1.17)] decomposed into the in-plane (i.e., along the x- and y-axes) and out-of-plane (i.e., along the z-axis) components. We then analyze heterogeneous dynamics in the contact layer using NGP given by Eq. (1.14) to extract characteristic times for the short-time ballistic motion and subsequent caging motion. The frequencies corresponding to these characteristic times are used to analyze the frequency range where the normal modes in the contact layer are most abundant. Then, we analyze the DOS of the first liquid and contact layers to quantify a degree of overlap between the distributions and study its impact on TBR. Finally, we propose a master curve relation for TBR in terms of contact layer temperature and L/S frequencies.

In Chapter 4, we used non-equilibrium molecular dynamics (NEMD) simulations to study thermal transport in a simple monatomic liquid confined between two crystalline walls whose exterior layers are maintained at different temperatures. By varying the energy parameter (wettability) and length parameter (repulsive distance) characterizing the L/S interaction and the temperature difference imposed on the system, we observed correlations between the thermal jump or thermal slip length and structural properties of the contact layer and analyzed their dependence on the local temperature at the interface. We argue that common descriptions of the contact layer including the contact density and depletion layer thickness cannot serve as a single unifying descriptor reflecting the effect of simultaneously changing the length and energy parameters on TBR. As an alternative, the 2D static structure factor was used to quantify a degree of spatial commensurability between the contact layer and surface potential of the adjacent solid. In the context of the fluid velocity slip at solid surfaces, the static structure factor has proven useful to understanding the momentum transfer across L/S interfaces [57, 74], but its significance in thermal transport has been much underestimated. To the extent of our knowledge, no previous work has provided a quantitative description of how in-plane liquid ordering affects thermal energy exchange between liquid and solid particles. We report that a simultaneous variation of the length and energy parameters result in a strong correlation between the thermal slip length and structure factor, suggesting that in-plane liquid ordering in directions normal to the heat flux plays more fundamental role in heat transfer than simple density enhancement.

We also explored the role of harmonic vibrational coupling on the interfacial thermal transport by computing the DOS of the contact layer and first solid layer. Instead of the DOS overlap commonly employed in MD studies, we measured the ratio of peak frequencies of the first solid layer and contact layer to quantify a degree of proximity between the DOS distributions of these layers. From the result of simulations, we constructed two types of master curve relations for the thermal slip length, the first expressing the thermal slip length in terms of the peak value of the structure factor and contact layer temperature and the second describing the correlation between the thermal slip length and peak frequency ratio. Both master curves were confirmed to be in excellent agreement with the measurements simulations within the parametric range explored.

1.3 Computational details

In this section, we provide computational descriptions of NEMD simulations applying to all projects discussed below. All physical quantities reported in this work are scaled by the reduced units in Table 1.1. The geometry of the multilayer rectangular cell used in the simulations is illustrated in Fig. 1.2(a) and its dimensions listed in Table 1.2.

As shown, the liquid layer was confined between two unthermostatted solid walls of thickness $L^{\mathrm{hs}} = L^{\mathrm{cs}}$. The centerline of the liquid layer was positioned at the coordinate origin $z = 0$. Each solid layer acting as the thermal source or sink was placed in contact with

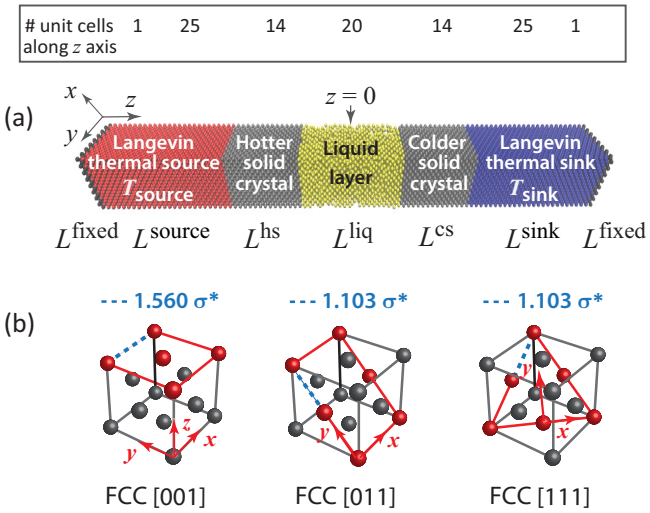

Figure 1.2: Schematics of the computational cell employed in NEMD simulations. (a) Liquid layer (yellow region) confined between two parallel solid walls (grey region) composed of FCC unit cells. External solid layers in red and blue were maintained at thermostat source and sink temperatures T_{source} and T_{sink}, respectively. Listed above the cell geometry are the approximate number of FCC unit cell lengths spanning each layer. (b) Three FCC facet orientations used in this study. Identical facet orientations were imposed on all solid layers.

a thermostatted solid of thickness $L^{\text{source}} = L^{\text{sink}}$. All simulations were carried out with thermostat temperatures $T_{\text{source}} = 1.3 + \Delta T_{Lang}/2$ and $T_{\text{sink}} = 1.3 - \Delta T_{Lang}/2$ where ΔT_{Lang} is the temperature difference applied between the heat source and heat sink. The values of ΔT_{Lang} and other simulation parameters chosen for individual projects are provided in Sections 2.2, 3.2, and 4.2. Migration or sublimation from the outermost boundaries of thickness L^{fixed} was preventing by affixing those particle in place.

All pairwise interactions between particle pairs $(ij) = LL$, LS or SS were modeled by a truncated and shifted 12-6 LJ potential given by

$$U_{ij}(r) = \begin{cases} U(r) - U(r_{\text{c}}) & \text{if } r \le r_{\text{c}}\,, \\ 0 & \text{if } r > r_{\text{c}} \end{cases} \tag{1.4}$$

where

$$U(r) = 4\,\varepsilon_{ij}\left[\left(\frac{\sigma_{ij}}{r}\right)^{12} - \left(\frac{\sigma_{ij}}{r}\right)^{6}\right], \tag{1.5}$$

and $r = |\vec{r}_i - \vec{r}_j|$ denotes the particle separation distance, ε_{ij} is the pairwise interaction energy (also called the bonding strength) and σ_{ij} is the separation distance corresponding to $U(r = \sigma) = 0$. The potential cutoff radius was set to $r_{\text{c}} = 2.5$. The truncated and shifted potential guarantees there are no discontinuities in the force field and therefore no impulsive

Physical quantity	Numerical value
mass	$m^* = 6.690 \times 10^{-26}$ kg
length	$\sigma^* = 0.3405 \times 10^{-9}$ m
energy	$\epsilon^* = 165.3 \times 10^{-23}$ J
temperature	$T^* = \epsilon^*/k_B = 119.8$ °K
time	$t^* = (m^*\sigma^{*2}/\epsilon^*)^{1/2} = 2.14$ ps
mass density	$\rho^* = m^*/(\sigma^*)^3$
pressure	$p^* = \epsilon^*/(\sigma^*)^3 = 41.7$ N/m^2
FCC edge length	$a^* = 1.560\,\sigma^* = 5.382 \times 10^{-10}$ m

Table 1.1: Symbols, numerical values and scalings for non-dimensionalization of physical quantities based on fluid argon [27, 45, 81]. Asterisk superscripts signify dimensional quantities. The Boltzmann constant $k_B = 1.380649 \times 10^{-23}$ J/K.

effects which could otherwise influence particle trajectories. Additional key parameters are listed in Table 1.1. For the range of temperature and density in this study, it was confirmed that the interior of the fluid layer remained a well defined dense liquid far from the critical and triple point [27, 72].

Cell dimensions	[001]	[011]	[111]
L_x	12.48	12.48	13.24
L_y	12.48	13.24	13.37
L^{fixed} (1 unit cell per end)	1.56	1.10	1.80
L^{source}	39.00	39.71	40.53
L^{hs}	21.84	22.06	21.17
L^{liq}	31.20	30.89	29.72
L^{cs}	21.84	22.06	21.17
L^{sink}	39.00	39.71	40.53
Total length along z axis	156.00	156.64	156.72

Table 1.2: Dimensions of the computational cell in Fig. 1.2(a) in reduced units.

To allow propagation of anharmonic modes, all solid layers were constructed using the LJ potential in contrast to studies which utilize harmonic wall-spring models. Since the melting temperature of an LJ solid is estimated to be $T_m \simeq \varepsilon_{SS}/2$ [68], the S/S interaction energy was set to $\varepsilon_{SS} = 10$ to ensure those layers remained in the solid state throughout the temperature range explored. At the start of each run, particles comprising all solid layers were situated identically and arranged on the lattice sites of an FCC crystal with unit cell edge length $a = 1.56$ [6]. Each solid layer comprised an integer number of unit cells to prevent overlap of particles along cell edges. The unit cells were oriented with their surface normal representing the [001], [011] or [111] facet oriented along the $\hat{z}$ axis. Dimensions for each orientation are shown in Fig. 1.2(b). The coordinates of the smallest reciprocal

FCC facet	$k_{o,x}$	$k_{o,y}$
[001]	±4.03	±4.03
[011] (shortest)	±4.03	0.00
[011] (2nd shortest)	0.00	±5.70
[111] (quadrants)	±5.70	±3.29
[111] (vertical axis)	0.00	±6.58

Table 1.3: Set of shortest reciprocal lattice vectors (RLVs) $\vec{k}_o = (k_x^o, k_y^o)$ (in reduced units) for three FCC facets of a real crystal lattice with unit cell edge length $1.56\sigma^*$. The RLVs for [001] are $(2\pi/a^*)(\widehat{e}_x, \widehat{e}_y)$, for [011] are $(2\pi/a^*)(\widehat{e}_x, 0)$ and for [111] are $(2\pi/a^*)(\sqrt{2}\widehat{e}_x, \sqrt{2/3}\widehat{e}_y)$ and $(2\pi/a^*)(0, \sqrt{8/3}\widehat{e}_y)$. The shortest and 2nd shortest RLVs for the [011] facet are relevant to this study, as discussed in the text.

lattice vectors for the real space facet orientations are listed in Table 1.4. Periodic boundary conditions were enforced along the $\hat{x}$ and $\hat{y}$ axes.

The L/S interaction strength was varied in increments of 0.1 over the range $0.1 \leq \varepsilon_{LS} \leq 1.0$ spanning behavior from non-wetting to strongly wetting, respectively. Different values of the thermal flux J_z were generated naturally by different choices of L/S interaction parameters (ε_{LS} and σ_{LS}), temperature difference ΔT_{Lang}, and crystal facet orientation. Simultaneous measurements extracted from the colder and hotter side of the liquid layer also allowed examination of the influence of local temperature on various static and dynamic quantities.

FCC facet	$k_{o,x}$	$k_{o,y}$
[001]	±4.03	±4.03
[011] (shortest)	±4.03	0.00
[011] (2nd shortest)	0.00	±5.70
[111] (quadrants)	±5.70	±3.29
[111] (vertical axis)	0.00	±6.58

Table 1.4: Set of shortest reciprocal lattice vectors (RLVs) $\vec{k}_o = (k_x^o, k_y^o)$ (in reduced units) for three FCC facets of a real crystal lattice with unit cell edge length $1.56\sigma^*$. The RLVs for [001] are $(2\pi/a^*)(\widehat{e}_x, \widehat{e}_y)$, for [011] are $(2\pi/a^*)(\widehat{e}_x, 0)$ and for [111] are $(2\pi/a^*)(\sqrt{2}\widehat{e}_x, \sqrt{2/3}\widehat{e}_y)$ and $(2\pi/a^*)(0, \sqrt{8/3}\widehat{e}_y)$. The shortest and 2nd shortest RLVs for the [011] facet are relevant to this study, as discussed in the text.

1.3.1 Temperature control

The NEMD simulations were carried out using the open source package LAMMPS [54, 73]. The equations of motion were integrated by the Verlet method [81] based on an time integration step $\Delta t_{int} = 0.002$. Liquid particles, initially situated on the lattice sites of an FCC crystal, were sequentially removed from the fluid layer until the bulk liquid density achieved a value $\rho_{bulk} \approx 0.84$. Particles in the liquid and unthermostatted solid layers were

initially equilibrated using a Nosé-Hoover thermostat [28] to a temperature $T_{\text{equil}} = 1.3$ for a period $10^5 \Delta t_{int} = 200$. This thermostat was then switched off and instead two Langevin thermostats [64] were activated in the heat source (red solid layers in Fig. 1.2) and heat sink (blue solid layers in Fig. 1.2) to maintain their temperatures at T_{source} and T_{sink}, respectively. Numerically, this is accomplished by replacing the Newton's equation of motion by the following Langevin equation:

$$\frac{d^2\vec{r}_i}{dt^2} = -\sum_{i \neq j} \frac{dU_{ij}(r)}{dr}\hat{r}_i - \frac{1}{\tau_{\text{damp}}}\frac{d\vec{r}_i}{dt} + \vec{F}_{\text{stoch}} \,, \tag{1.6}$$

where $\vec{r}_i$ is the 3D spatial coordinate of particle i and $\vec{F}_{\text{stoch}}$ denotes a random force vector modeled by a normal distribution of magnitude $[T_{\text{set}}/(\tau_{\text{damp}}\ \Delta t_{int})]^{1/2}$ with set point temperature T_{set}. The damping constant was chosen to be $\tau_{\text{damp}} = 500\ \Delta t_{int} = 1.0$. After activation of the Langevin thermostats, particles were subject to an additional stabilization period of $2 \times 10^5 \Delta t_{int} = 400$ to ensure steady state conditions. Particle trajectories in the unthermostatted liquid and solid layers evolved according to Newton's equation of motion, i.e., Eq. (1.6) without the damping or stochastic term. The motion of unthermostatted particles therefore derived exclusively from LJ interactions with neighboring particles situated within the potential cutoff radius $r \leq r_c = 2.5$. To ensure proper thermal calibration, it was confirmed that for $T_{\text{source}} = T_{\text{sink}}$, the simulations generated a uniformly flat temperature profile throughout the unthermostatted liquid and solid layers.

The thickness of the thermostatted layers L^{source} and L^{sink}, which ranged from about 39 to 40 (in reduced units), was chosen to exceed the length of a typical phonon mean free path α so as to avoid spurious reduction in thermal boundary resistance [37]. It has been shown that for $\alpha = c_\ell \times \tau_{\text{damp}} \leq 2L_s$, where c_ℓ is the longitudinal speed of sound [21], phonons generated within the thermostatted layers are dissipated before undergoing reflection and propagation from the outer boundary to the L/S interface. Stevens et al. [68] have reported that the value c_L for an FCC crystal is well approximated by the relation $c_l = 9.53\sqrt{\varepsilon_{SS}}$. For the parameter values used in this study, namely $\varepsilon_{SS} = 10$, $\tau_{\text{damp}} = 1$ and $L_s = 39$, the inequality $\alpha = c_\ell \times \tau_{\text{damp}} = 9.53\sqrt{10} \simeq 30 \leq 2L_s = 78.0$ was well satisfied.

Previous studies in the literature [21, 50] have examined the influence of liquid pressure on the reduction in thermal boundary resistance. We confirmed that the pressure within the bulk liquid was very weakly dependent on FCC facet orientation and not a significant contributor to any reductions in thermal slip length measured. Specifically, the pressures within the bulk liquid for $\varepsilon_{LS} = 0.1$ were measured to be $2.72 \pm 0.03[001]$, $2.78 \pm 0.02[011]$ and $2.86 \pm 0.02[111]$ and for $\varepsilon_{LS} = 1.0$ were measured to be $2.54 \pm 0.02[001]$, $2.60 \pm 0.03[011]$ and $2.66 \pm 0.03[111]$. All things equal, non-wetting fluids gave rise to a slightly higher bulk liquid pressure, as expected. For the density and temperature range explored in this study,

it was confirmed that roughly 90% of the bulk liquid pressure stemmed from the virial (not kinetic) contribution.

1.3.2 Averaging procedure for time-independent quantities

After thermal stabilization was complete and a steady thermal flux established, averages of various time-independent quantities were carried out as follows. The motion of particles was monitored for a total time $t_{\text{total}} = 5 \times 10^6 \Delta t_{int} = 10^4$, which was divided into ten equal and non-overlapping subdivisions. Within each subdivision, the motion was sampled at intervals of $500\Delta t_{int} = 1.0$ and so the mean values extracted from each subdivision were based on 1000 samplings. This sampling interval was chosen based on inspection of the velocity autocorrelation function, which decayed to zero by $t = 1.0$ (see Fig. 2.13). In what follows, the reported average values and standard deviations of all time-independent quantities, which are denoted by angular brackets $\langle \cdot \rangle$, were computed by averaging the mean values from each of the ten subdivisions.

Variation of quantities along the $\hat{z}$ axis was obtained by partitioning the unthermostatted liquid and solid layers into non-overlapping bins of volume $L_x \times L_y \times \Delta z_{\text{bin}}$, where Δz_{bin} is the bin width. A very slender bin width $\Delta z_{\text{bin}} = 0.016$ was used in computing density profiles $\langle \rho(z) \rangle$ to ensure resolution of spatial oscillations near the L/S interface indicative of liquid layering. The average density $\langle \rho(z) \rangle$ within each bin was computed from the ratio $\rho_{\text{bin}} = \langle N_{\text{bin}} \rangle / V_{\text{bin}}$, where $\langle N_{\text{bin}} \rangle$ is the average number of particles within a bin. For the values given in Table 1.2, the bin volume corresponding to each facet orientation was 2.49 for [001], 2.64 for [011] and 2.83 for [111]. In this study, the mass density and number density are equivalent since the masses of solid and liquid particles were all set to unity.

A coarser resolution $\Delta z_{\text{bin}} = 0.785$ was used for extracting the temperature distribution $\langle T(z) \rangle$. Too small a bin width causes excessively noisy velocity and thermal profiles from too small values of N_{bin}. It was confirmed that even for the narrowest bin width $\Delta z_{\text{bin}} = 0.016$, $\langle T(z) \rangle$ did not exhibit oscillations near the L/S interface. The average temperature T_{bin} within a bin was extracted from the equipartition relation

$$T_{\text{bin}} = \left\langle \frac{1}{3N_{\text{bin}}} \sum_{i}^{N_{\text{bin}}} \vec{v}_i^2 \right\rangle, \tag{1.7}$$

where i denotes a particle within the bin with a (3D) velocity vector $\vec{v} = (v_x, v_y, v_z)$. In computing the thermal gradient within the interior liquid and solid layers and corresponding thermal slip length, only the linear portion of the distribution $T(z)$ away from the L/S interface was fitted.

Temperature jumps at the L/S boundary were extracted from the difference between the temperature profiles linearly extrapolated from the interior solid and liquid layers evaluated at the midpoint of the depletion layer thickness, defined as the distance along the $\hat{z}$ axis

separating the peak values in density of the first adjacent solid and liquid layer. As expected, depletion layer thickness was found to vary with ε_{LS}, facet orientation and contact layer temperature. The thermal slip length, measured at both the hotter and colder sides of the liquid layer, was computed from Eq. (1.2).

In what follows, the *contact layer* refers exclusively to the first layer of *liquid* particles immediately adjacent to the solid surface. The thickness of this layer was measured to be the distance between neighboring minima in $\rho(z)$ bracketing the first oscillation in the liquid density. This distance was evaluated unambiguously because of the distinct stratification in liquid density near the L/S interface for all parameter values explored.

As discussed in later chapters, different choices of ε_{LS} and crystal facet orientation naturally yielded different values of the thermal flux J_z, which was evaluated from estimates of

$$J_z = \frac{1}{L_x \times L_y} \frac{E_{\text{net}}(t)}{t} , \tag{1.8}$$

where $E_{\text{net}}(t)$ is the net thermal input over a time interval t that was required to maintain the Langevin reservoirs at the set point temperatures T_{source} and T_{sink}. It was confirmed that E_{net} increased linearly in time, as required for steady state conditions. The thermal conductivity values representing the interior liquid and interior solid layers was extracted from the ratio $k = J_z/|dT/dz|$, where the thermal gradient was obtained by a least squares fit over the linear portion of the thermal profile.

Steady state particle distribution patterns within the interior liquid, contact layer and first crystalline layer were evaluated using the static 2D radial distribution function given by

$$g^{\parallel}(r) = \left\langle \frac{L_x \times L_y}{N_{\parallel}} \frac{n_{\text{pairs}}(r)}{2\pi r \Delta r} \right\rangle , \tag{1.9}$$

where $N_{\parallel}$ is the number of particles within the selected layer and n_{pairs} is the number of particle pairs within an annulus of radius $r - \Delta r/2 \leq r \leq r + \Delta r/2$ with $\Delta r = 0.01$.

Additional information about long range order within the contact layers was obtained from the static 2D structure factor given by

$$S_c^{\parallel}(\vec{k}) = \left\langle \frac{1}{N_c^2} \sum_{p=1}^{N_c} \exp\left(i\vec{k} \cdot \vec{r}_p\right) \sum_{q=1}^{N_c} \exp\left(-i\vec{k} \cdot \vec{r}_q\right) \right\rangle , \tag{1.10}$$

where N_c is the number of particles in the contact layer and $\vec{k} = (k_x, k_y)$ is a planar wave vector. Eq. (1.10) is normalized such that $0 \leq S_c^{\parallel}(\vec{k}) \leq 1$. It was confirmed that within statistical error, contributions from the imaginary part of Eq. (1.10) were vanishingly small. All reported measurements in this work represent the real contribution to Eq. (1.10).

The Voronoi diagrams were generated using MATLAB based on a randomly-selected snapshot of liquid particles in the contact layer. Since particles in the contact liquid layer do not have the same z-coordinate in most cases, we considered two-dimensional Voronoi diagrams of the projections of particle positions onto the xy-plane. For each particle in the contact layer, the coordination number m is represented by the number of edges in the two-dimensional Voronoi cell. To compare Voronoi diagrams across three facets and analyze their temperature and wettability dependencies, we evaluated the coordination number distributions, i.e., the number of Voronoi cells with m-edges normalized by the total number of Voronoi cells found in the contact layer. In current study, we obtained the coordination number distributions for $m = 4, 5, 6$ which correspond to rectangular, pentagonal, and hexagonal cells, respectively. It will be later shown that Voronoi cells with other shapes are rarely seen in the contact layer.

Rotational symmetry corresponding to $m = 4, 5, 6$ is quantified by the local bond-orientational order parameter which is defined as

$$\psi_m = \left| \frac{1}{N_c} \sum_{j}^{N_c} \frac{1}{N_j} \sum_{k}^{N_j} \exp(im\theta_{jk}) \right|. \tag{1.11}$$

Here, m is an integer representing the rotational degree of freedom, N_j is the number of first neighbors of particle j, and θ_{jk} is the angle made by the line joining particle j and one of its neighbors k with the x-axis. Here, the first neighbors refer to all particles located in the first shell of the 2D radial distribution function Eq. 1.9.

1.3.3 Averaging procedure for time-dependent quantities

Time-dependent and correlated behavior of particles in the contact layer was based exclusively on collections of liquid particles which remained within the layer throughout the entire measurement interval. Particles which exited the contact layer but then returned were excluded from the current analysis. For a given solid facet orientation, it was generally the case that an increase in ε_{LS} or decrease in contact layer temperature led to longer particle residence times.

Once steady state thermal conditions had been established, averages of time-dependent quantities were carried out using the following block averaging scheme. For the first block, tracking of particle trajectories was initiated at data collection times $t_o = (0, 10, 20, \ldots, 475,000) \times \Delta t_{int}$ then subsequently sampled at short intervals $10\Delta t_{int} = 0.02$. Data collection spanned a period $t_o \leq t \leq t_o + t_f$, where t_f was selected to be the longest interval of time during which at least ten particles remained exclusively within the contact layer throughout the period of measurement. For comparison, listed in Table 1.5 are measurements of the average total number of particles within the hotter and colder contact layer for two values of ε_{LS} and the

three facets. Therefore, by the time only ten particles from the original occupancy number remained, roughly 90% had exited the layer at least once.

Facet	ε_{LS}	$\langle N_c \rangle_{\text{hotter}}$	$\langle N_c \rangle_{\text{colder}}$
[001]	0.1	104.3 ± 0.4	109.9 ± 0.4
[011]	0.1	116.6 ± 0.4	125.3 ± 0.4
[111]	0.1	122.0 ± 0.4	128.6 ± 0.4
[001]	1.0	114.9 ± 0.4	125.0 ± 0.5
[011]	1.0	80.7 ± 0.3	92.9 ± 0.4
[111]	1.0	134.1 ± 0.4	161.4 ± 0.5

Table 1.5: Average total number of particles $\langle N_c \rangle$ in the contact layer at the hotter and colder side for $\varepsilon_{LS} = 0.1$ and 1.0 and three facets.

Each initial time for data collection t_o therefore led to slightly different values of t_f. For meaningful averages with a single block, the smallest value t_f was used to compute the time average relevant to the block. A similar procedure was applied to two subsequent non-overlapping blocks, with the first data collection time in the sequence set to the value t_f of the previous block. The smallest overall value t_f recorded for three such blocks was then used to extract the final average reported pertaining to the overall block (B) average. Relations for quantities indicated by the symbol $\langle \cdot \rangle^B_{t_o,}$ therefore denote the final average value based averages over t_o followed by block averaging. In all cases, the time t_f far exceeded the decay time of the velocity autocorrelation function by an order of magnitude.

Dynamic regimes describing different types of particle motion within the contact layer were quantified by the 2D mean-squared displacements, self-intermediate scattering function, and non-Gaussian parameter. The 2D mean-squared displacement was computed as

$$MSD_c^{\parallel}(t) = \left\langle \frac{1}{N_c} \sum_j^{N_c} \left| \vec{r}_j(t_o + t) - \vec{r}_j(t_o) \right|^2 \right\rangle_{t_o}^{B}, \tag{1.12}$$

where $\vec{r}_j(t) = [x_j(t), y_j(t)]$ is the 2D position vector of particle j within the contact layer and $N_c = N_c(t_o, t_f)$ is the number of particles permanently occupying the contact layer throughout the measurement interval $t_o \leq t \leq t_o + t_f$ subject to the constraint $N_c \geq 10$. The 2D self-intermediate scattering function was evaluated according to

$$F_c^{\parallel}(\vec{k}_o, t) = \left\langle \frac{1}{N_c} \sum_{j=1}^{N_c} \exp\left\{ i\, \vec{k}_o \cdot \left[\vec{r}_j(t_o + t) - \vec{r}_j(t_o) \right] \right\} \right\rangle_{t_o}^{B}, \tag{1.13}$$

where $\vec{k}_o$ represents the wave vector corresponding to the first peak in the structure factor. As discussed earlier, $\vec{k}_o$ was found to equal the smallest reciprocal lattice vector except

for the [011] case below the structural transition which coincided instead with the second smallest reciprocal lattice vector. The results in Section 2.3 represent the real contribution to $F_c^{\parallel}(\vec{k}_o, t)$ - the imaginary contributions were found to be negligibly small by comparison.

Dynamic heterogeneity governing structural relaxation of the contact layer is quantified by the non-Gaussian parameter (NGP) which is defined as [58]

$$\alpha_2(t) = \frac{\langle \Delta r(t)^4 \rangle}{(1 + \frac{2}{d})\langle \Delta r(t)^2 \rangle^2} - 1 \,, \tag{1.14}$$

where $d = 2$ represents the spatial dimension. Non-Gaussian behavior or underlying dynamic heterogeneity leading to caged motion within the contact layer is represented by non-zero value of the NGP.

The velocity autocorrelation function for particles in the contact layer was determined in similar fashion according to

$$VACF_c^{\parallel}(t) = \left\langle \frac{1}{N_c} \sum_{j=1}^{N_c} \vec{v}_j(t_o + t) \cdot \vec{v}_j(t_o) \right\rangle_{t_o}^{B} . \tag{1.15}$$

We then computed the density of states which is obtained by taking the temporal Fourier transform of the VACF [7]:

$$\mathrm{DOS}(\nu) = \left\langle \frac{4}{N_c T} \int_0^{t_f} \sum_{j=1}^{N_c} \vec{v}_j(t_o + t) \cdot \vec{v}_j(t_o) \cos(2\pi i \nu t) dt \right\rangle_{t_o}^{B} . \tag{1.16}$$

Here T is the local temperature in the first solid or liquid layer and ν is the frequency. The normalization factor in Eq. (1.16) was chosen to satisfy the equipartition theorem upon integrating over all frequencies: $\int_0^{\infty} \mathrm{DOS}(\nu) d\nu \sim 3$. It is crucial that local thermal equilibrium is established in the solid or liquid layer since Eq. 1.16 is based on the equipartition theorem, i.e., that the solid or liquid layer has a well-defined temperature even when the system as a whole is in thermal non-equilibrium. In Section 2.3.1, we demonstrate that local thermal equilibrium is indeed established by showing that particles in the contact layer follow the Maxwell-Boltzmann distribution function even when thermal gradient is non-zero.

1.3.4 Averaging procedure for spectral heat flux

The mode-level contribution to the interfacial heat transfer was quantified using the spectral heat flux, [60–62]:

$$q_{L\to S}(\nu) = \frac{2}{L_x \times L_y} \left\langle \left| \mathrm{Re} \sum_{i,j} \int_{-\infty}^{\infty} \vec{F}_{ij}(t + t_o) \cdot \vec{v}_i(t_o) e^{2\pi i \nu t} dt \right| \right\rangle^{B} . \tag{1.17}$$

Here, t is the correlation interval between the velocity $\vec{v}_i$ of the i-th solid atom and the force $\vec{F}_{ij}$ exerted by the j-th liquid atom, and the symbol $\langle \cdot \rangle^B$ represents an average over five non-overlapping time blocks which will be detailed shortly. On average, the correlation function $\vec{F}_{ij}(t+t_0)\cdot\vec{v}_i(t_0)$ depends only on t (and not on a time origin t_o) due to the assumed steady state. The double summation is over all L/S pairs within the cutoff distance from the L/S interface. Following the derivation in Ref. [60], we could express Eq. 1.17 in terms of discrete Fourier transforms of force and velocity trajectories obtained from the solid atoms:

$$q_{L\to S}(\nu) = \frac{1}{L_x \times L_y} \frac{2}{N_{\text{samp}}\Delta t_{\text{samp}}} \left\langle \left| \text{Re} \sum_{i,j} \hat{F_{ij}}(\nu)\cdot\hat{v_i}(\nu) \right| \right\rangle^B. \tag{1.18}$$

Here, the discrete Fourier transforms of force ($\hat{F_{ij}}(\nu)$) and velocity ($\hat{v_i}(\nu)$) are evaluated as

$$\hat{F_{ij}}(\nu_l) = \Delta t_{\text{samp}} \sum_{k=1}^{N_{\text{samp}}} e^{2\pi i \nu_l k \Delta t_{\text{samp}}} \vec{F}_{ij}(k\Delta t_{\text{samp}}), \tag{1.19}$$

$$\hat{v_i}(\nu_l) = \Delta t_{\text{samp}} \sum_{k=1}^{N_{\text{samp}}} e^{2\pi i \nu_l k \Delta t_{\text{samp}}} \vec{v}_i(k\Delta t_{\text{samp}}). \tag{1.20}$$

Here, $\Delta t_{\text{samp}} = 10\Delta t_{int}$ is the time interval between successive data collection, $N_{\text{samp}} = 5\times10^4$ is the total number of samples used to compute discrete Fourier transforms, and $\nu_l = l/N_{\text{samp}}\Delta t_{\text{samp}}$ ($l = 0, 1, 2\ldots$) is the sampling frequency.

We collected force and velocity over five non-overlapping, evenly-spaced time blocks starting at $t_o = (5n\times10^5)\Delta t_{int}$ where $n = 0, 1, 2, 3, 4$. For instance, force and velocity of particles in the first time block starting at $t_o = 0$ was collected at $t = (0, 10, 20, 30, \cdots, 5\times10^5 - 10)\Delta_{int}$. Then, the discrete Fourier transforms for force [Eq. (1.19)] and velocity [Eq. (1.20)] were computed to obtain the spectral heat flux within each block. A Gaussian window of width $\Delta\nu = 1.0$ was required to smooth out the sharply fluctuating spectrum within each block. Finally, five samples thus obtained were averaged to compute the final average.

It is also possible to decompose Eq. (1.18) into contributions along different directions as follows:

$$q^{\alpha}_{L\to S}(\nu) = \frac{1}{L_x \times L_y} \frac{2}{N_{\text{samp}}\Delta t_{\text{samp}}} \left\langle \left| \text{Re} \sum_{i,j} \hat{F^{\alpha}_{ij}}(\nu)\hat{v^{\alpha}_i}(\nu) \right| \right\rangle^B, \tag{1.21}$$

where $\alpha \in x, y, z$ denotes the contribution along one of the three Cartesian coordinates, and $\hat{F^{\alpha}_{ij}}(\nu)$ and $\hat{v^{\alpha}_i}(\nu)$ are the respective components of the discrete Fourier transforms in Eq. (1.19) and Eq. (1.20).

Chapter 2

EFFECT OF CAGING DYNAMICS IN THE CONTACT LAYER ON THERMAL TRANSPORT

2.1 Overview of this chapter

The simulation parameters used in this project are discussed in Section 2.2. In Section 2.3, we first benchmark the system by showing how crystal facet orientation, L/S interaction energy and contact layer temperature influence stationary properties such as the liquid density profile, liquid contact density, temperature profiles, thermal flux and thermal slip length. We then examine features of the 2D (i.e., in-plane) radial distribution function and 2D static structure factor describing particle organization throughout the contact layer. This is followed by examination of the 2D and 3D velocity autocorrelation function, 2D mean square displacement and 2D self-intermediate scattering function. The discussion in Section 2.4 focuses on the main finding that a smaller thermal slip length correlates positively with a larger non-ergodicity parameter but shorter – not longer – caging time.

Variable	Value in scaled units
mass of each particle	1
LJ particle diameter	$\sigma_{LL} = \sigma_{SS} = \sigma_{LS} = 1.0$
LJ interaction energy	$\varepsilon_{LL} = 1.0$
	$\varepsilon_{SS} = 10$
	$\varepsilon_{LS} = 0.1 - 1.0$
FCC edge length	$a = 1.560$
integration time step	$\Delta t_{int} = 0.002$
source temperature	$T_{\text{source}} = 1.6$
sink temperature	$T_{\text{sink}} = 1.0$
bulk liquid density	$\rho_L \approx 0.84$
FCC unit cell density	$\rho_S = 1.0536$
FCC crystal facet	[001], [011], [111]

Table 2.1: List of simulation parameters employed in Chapters 2-3. All numerical values are reported in dimensionless units detailed in Table1.1.

2.2 Simulation parameters

In this project, the FCC crystal lattice comprising each solid substrate was orientated so that the [001], [011], and [111] crystal directions are pointing along the $\hat{z}$ axis. Three solid facets constituting the first solid layers are depicted in Fig. 1.2(b). For each choice of FCC facet, we systematically increased the L/S interaction energy ε_{LS} from 0.1 (non-wetting interaction) to 1.0 (strongly-wetting interaction) in increments of 0.1. The L/S repulsive distance σ_{LS}

was fixed to 1.0 in all simulation runs.The heat source and heat sink temperatures were set to $T_{source} = 1.6$ and $T_{sink} = 1.0$, respectively, for all simulation runs in this project. The temperature dependence of TBR and other interfacial properties was analyzed by comparing the measurements taken at the hotter and colder interfaces. The numerical values of other simulation parameters are summarized in Table 2.1.

2.3 Results

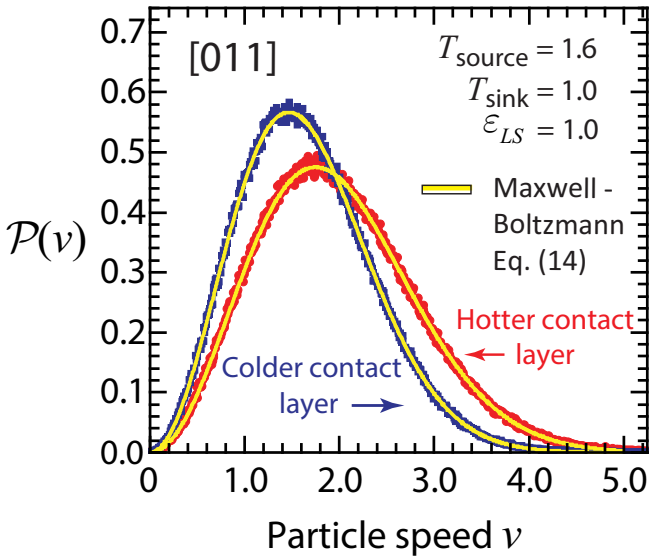

Figure 2.1: Sample distribution $\mathcal{P}(v)$ showing liquid particle speed inside the hotter and colder contact layer facing an [011] facet for $\varepsilon_{LS} = 1.0$. Superimposed on the data is the Maxwell-Boltzmann distribution function in Eq. (2.1) for fit constants $T_h^{\text{fit}} = 1.526 \pm 0.001$ and $T_c^{\text{fit}} = 1.0740 \pm 0.0009$.

2.3.1 Thermal equilibrium of the contact layer

Shown in Fig. 2.1 is a sample plot of the particle speed distribution in a hotter and colder contact layer against a [011] facet for $\varepsilon_{LS} = 1.0$. Superimposed on the data are least square fits to the Maxwell-Boltzmann distribution (in reduced units)

$$\mathcal{P}(v_i) = 4\pi\left(\frac{1}{2\pi T}\right)^{3/2} v_i^2 \exp\left(-\frac{v_i^2}{2T}\right) \quad \text{for } i \in N_c, \tag{2.1}$$

where $v_i^2 = (v_{i,x})^2 + (v_{i,y})^2 + (v_{i,z})^2$. Least squares fits to Eq. (2.1) yielded the fit constants $T_h^{\text{fit}} = 1.526 \pm 0.001$ and $T_c^{\text{fit}} = 1.074 \pm 0.001$. The average kinetic energy in the contact layer, as derived from the Maxwell-Boltzmann distribution, yields the equipartition relation. Least squares fits to Eq. (1.7) yielded very similar estimates $T_h = 1.529 \pm 0.006$ and $T_c = 1.074 \pm 0.004$, as should be the case.

As expected, the distribution of particle speeds in Fig. 2.1 is broader and the average speed

and therefore kinetic energy higher for the particles in the hotter layer. While the overall layered S/L/S system describes a state of thermal non-equilibrium due to the application of a steady temperature gradient, this distribution of velocities confirms that the contact layer is in a state of local thermal equilibrium. It was also confirmed that for the parameter values used in this study, the liquid film remained quiescent and never underwent any convective flow.

2.3.2 Characterization of contact layer by time-independent quantities

2.3.2.1 Contact layer density

It is known from prior molecular dynamics studies of systems in thermal equilibrium [16, 25, 67, 78, 80] and non-equilibrium [4, 21, 41, 43, 57, 74, 76] that a fluid in contact with a featureless or structured solid will exhibit an oscillatory density profile $\rho(z)$. The characteristic peak to peak separation is normally set by the repulsive part of the inter particle potential. For a sufficiently thick liquid layer, the amplitude and number of oscillations increases at colder temperature or higher values of ε_{LS}, with rapid decay to the value of the interior liquid. These general features are evident too in Fig. 2.2(a)–(f) showing the influence of ε_{LS}, facet and local temperature on the liquid density profile. The horizontal line is the reference value $\rho = 0.84$ of the interior liquid chosen for this study.

The results in Fig. 2.2(a)–(f) confirm that the spacing of crystal planes is smallest for the [011] and largest for the [111] facet and that the solid layer peak density is largest for [111] and smallest for [011], in line with the facet dimensions in Fig. 1.2(b). The degree of liquid layering, indicated by the amplitude and number of oscillations, is smallest for the [011] facet and largest for the [111] facet. This suggests that particles in the contact layer against a [011] facet can move more easily between layers in comparison to comparable particles against the other two facets. We shall return to this point when discussing results extracted from actual particle trajectories. At both the hotter and colder interfaces, it is apparent that the liquid facing the [011] facet also undergoes a structural transition at some value ε_{LS} which depends on temperature. This abrupt jump, particularly noticeable on the hotter side, is evident from the shift in the location of the first liquid oscillation. For values ε_{LS} above the transition, the depletion layer thickness for the [011] case decreases while that for the [001] and [111] undergo a slight increase. That said, the depletion layer thickness for the liquid facing a [011] facet is always the smallest of all facets no matter the value ε_{LS}.

Shown in Fig. 2.2(g) is the contact density ρ_c for the contact layer facing different facets on the hotter and colder side with increasing ε_{LS}. In all cases, ρ_c rises monotonically with increasing ε_{LS}, although the slope of the rise is highest for colder temperature. In comparing the influence of facet orientation either on the hotter or colder side, for a given value of ε_{LS}, ρ_c is smallest against the [011] facet by a significant amount and largest against the [111] facet. The structural transition noted earlier for the [011] case seems evident here too for

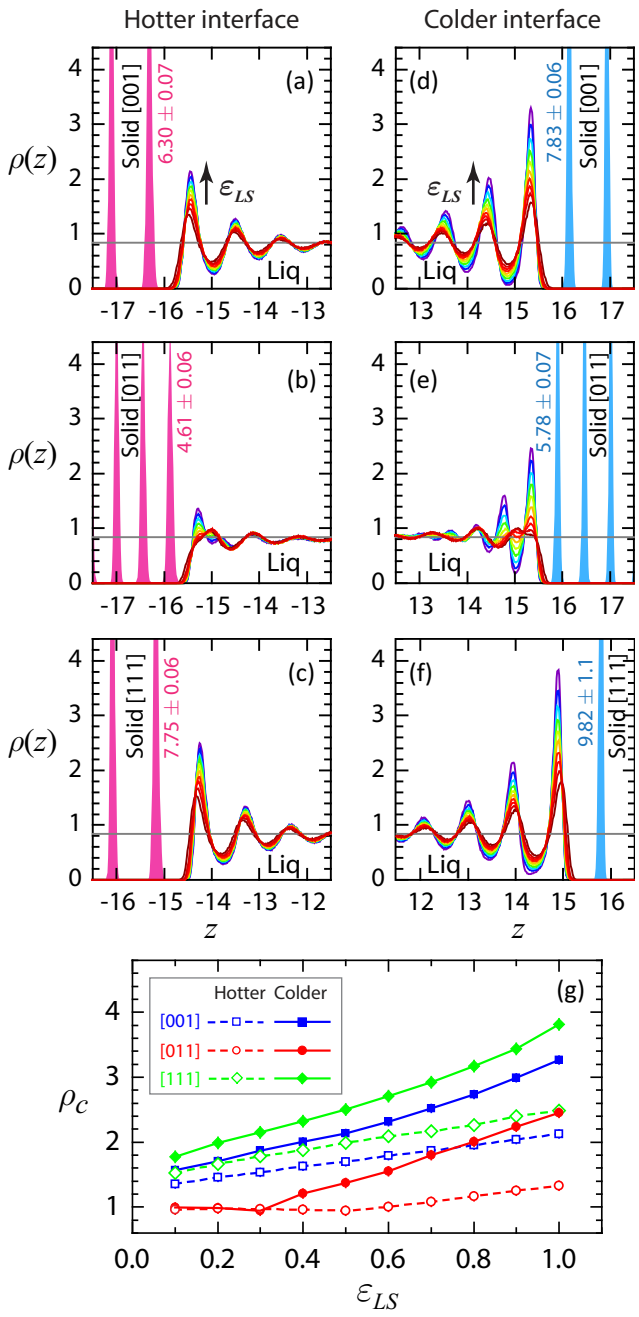

Figure 2.2: Liquid density $\rho(z)$ at (a)–(c) hotter and (d)–(f) colder L/S interfaces for three facets and $0.1 \leq \varepsilon_{LS} \leq 1.0$ in increments of 0.1. Also shown are the first few peaks of the solid density for $\varepsilon_{LS} = 1.0$ (amplitude exceeds plot boundary) and the interior liquid density $\rho_{\text{bulk}} = 0.84$ (grey horizontal line). Numerical values listed next to the first solid layer denote the peak solid density (evaluated with bin width $\Delta z = 0.016$). (g) Contact density ρ_c across three facets for $0.1 \leq \varepsilon_{LS} \leq 1.0$. Connecting segments are only a guide to the eye. Error bars are smaller than the line thickness and not visible.

$0.3 \lesssim \varepsilon_{LS} \lesssim 0.4$; below this range, ρ_c is rather insensitive to ε_{LS} and temperature.

It is well known that the interfacial energy density (i.e., energy per unit area of the interface) of liquid particles against a structured or unstructured solid wall is comprised of three distinct contributions – namely, the Gibbs surface excess energy, the excess entropy and the excess number of absorbed liquid particles [78]. Although beyond the scope of this current work, quantification of the relative contributions to the interfacial energy density for increasing value ε_{LS}, different facet orientation and different local temperature will provide more insight into the mechanism driving the structural transition of the contact layer for the [011] case.

2.3.2.2 Thermal profiles and thermal flux

Shown in Fig. 2.3(a)–(c) are the temperature profiles $T(z)$ throughout the liquid and unthermostatted solid layers. The sizeable jumps at the hotter and colder side reflect the influence of thermal boundary resistance at a L/S interface. Away from the interface, the profiles are linear and the thermal gradient therefore constant, confirming the layers are Fourier conductors. Since the interior liquid density depends on temperature and pressure, there is no symmetry about the $z = 0$ axis, as evident. At steady state and in the absence of convective flow, energy conservation requires that the thermal flux J_z be a constant throughout the unthermostatted layers. Therefore, the layer containing liquid must maintain a much larger magnitude of the thermal gradient, since the thermal conductivity of a simple liquid is always much smaller than that of a solid. The results show that the slope of $T(z)$ in the liquid layer increases monotonically with increasing value ε_{LS}, corresponding to smaller values of the thermal jump. Measured values of the thermal flux, thermal gradient and thermal conductivity can be found in Table 2.5 and values of the thermal jump and contact layer temperature in Table 2.6. The data confirm that an increase in L/S interaction energy ε_{LS} reduces thermal boundary resistance such that the temperature of the contact layer T_c is closer to the surface temperature of the solid facet. The data also reveal that for a given value ε_{LS}, the thermal jump ΔT is not always higher at the colder interface, as one might intuit naively. In fact, the data in Table 2.6 confirm that for the same value ε_{LS}, the ratio $\Delta T|_{hotter}/\Delta T|_{colder}$ can be smaller, equal to or larger than one. This is because even for the same value ε_{LS} and same facet, the thermal flux J_z is different due to the influence of local temperature. It is for this reason that proper comparison between systems of the thermal boundary resistance or thermal slip length requires normalization by the thermal flux, just as indicated by the definitions in Eq. (1.1) and Eq. (1.2).

Recall that in this study, the set point temperature of the thermal source and sink were set at $T_{\text{source}} = 1.6$ and $T_{\text{sink}} = 0.6$ for all simulations conducted. The steady thermal flux J_z propagating through the system was therefore not imposed but arose naturally by choice of ε_{LS} and facet orientation. These two input parameters also determined the contact layer

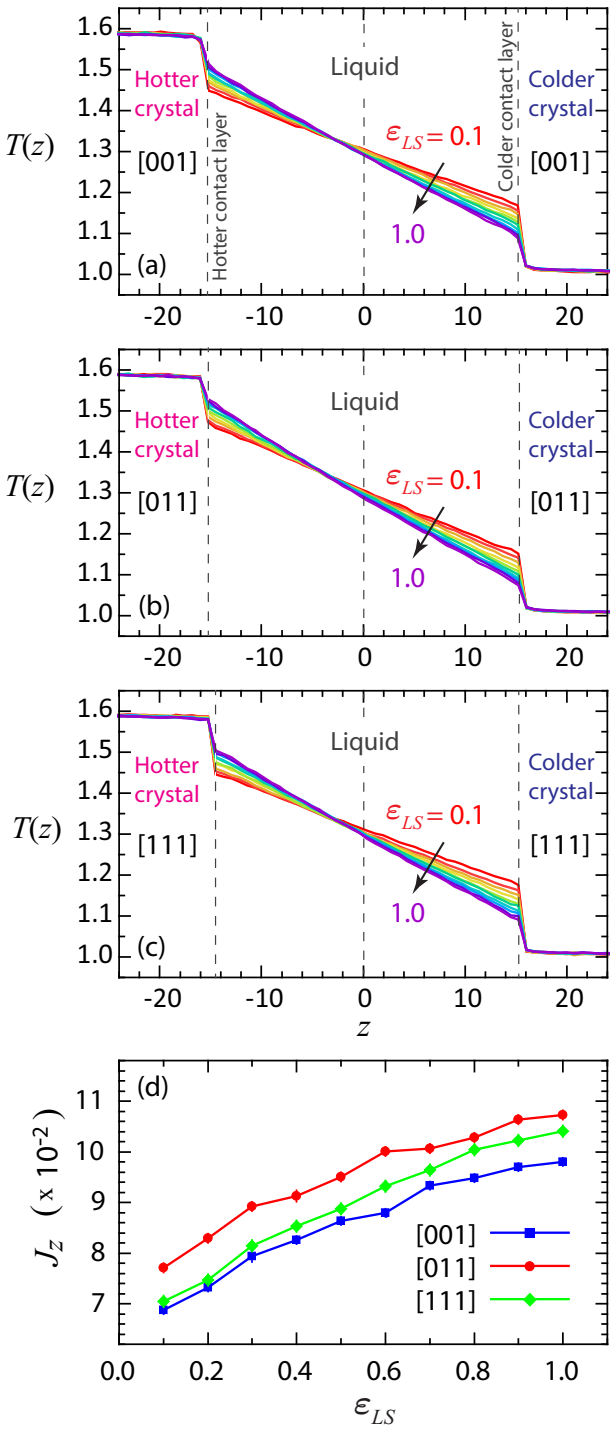

Figure 2.3: Steady state temperature distribution $T(z)$ throughout the solid and liquid layers for (a) [001], (b) [011], and (c) [111] facets and $0.1 \leq \varepsilon_{LS} \leq 1.0$ in increments of 0.1. (d) Corresponding values of the steady thermal flux J_z. Connecting segments are only a guide to the eye.

temperature. For the geometry used in this study, the L/S interaction energy ε_{LS} and facet choice therefore essentially established "interface filters" which regulated the magnitude of the thermal flux crossing the L/S interface as well as the contact layer temperature. The results in Fig. 2.3(d) show that for the same value ε_{LS}, the highest thermal flux is achieved with the [011] facet by a significant amount.

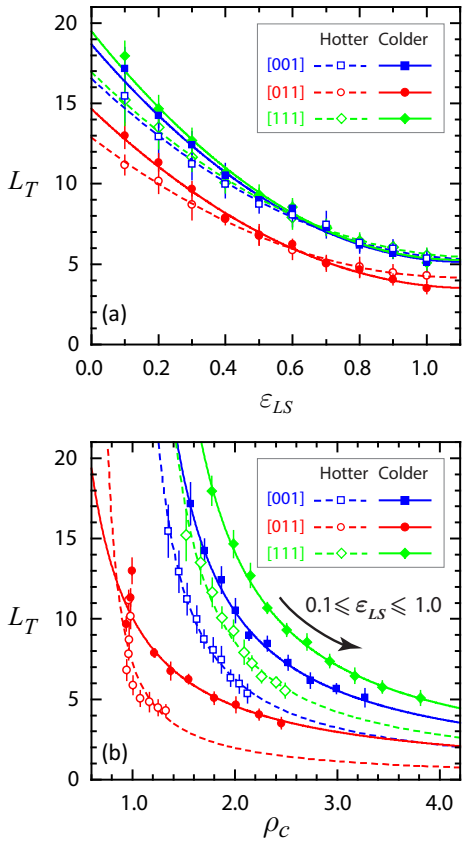

Figure 2.4: Reduction in the thermal slip length L_T with (a) increasing L/S interaction energy ε_{LS} and (b) increasing contact density ρ_c at the hotter and colder interfaces for three facet orientations. Superposed solid and dashed curves represent least squares fit to Eq. (2.2) and Eq. (2.3), with fit constants listed in Table 2.2 and Table 2.3, respectively.

2.3.2.3 Dependence of the thermal slip length on L/S interaction energy and contact density

Shown in Fig. 2.4(a) is the reduction in the thermal slip length, computed from Eq. (1.2), at the hotter and colder L/S interface, for increasing value ε_{LS} and increasing contact density for the three solid facets. In all cases, the thermal slip length decreases monotonically with increasing ε_{LS}. The reduction in L_T is higher for $\varepsilon_{LS} \lesssim 0.6$ and more gradual above that value showing less sensitivity to ε_{LS} for more wetting liquids. The key result is that for a given value ε_{LS}, the thermal slip length is always smallest for the [011] facet by a considerable amount and largest for the [111] facet. A reduction in thermal slip length as

ε_{LS} increases has previously been reported in NEMD studies [4, 5, 90] relying on different thermostatting methods, different L/S media and different parameter ranges, but no general relation proposed. Our data in Fig. 2.4(a) are well fit by the quadratic relation

$$L_T(\varepsilon_{LS}) = a - b\ \varepsilon_{LS} + c\ \varepsilon_{LS}^2\ , \tag{2.2}$$

Facet	H/C side	a	b	c
[001]	H	16.5 ± 0.5	19.0 ± 2.0	8.0 ± 1.0
[011]	H	12.9 ± 0.2	15.9 ± 0.8	7.3 ± 0.6
[111]	H	16.9 ± 0.3	20.0 ± 1.0	8.7 ± 0.8
[001]	C	18.7 ± 0.6	24.0 ± 2.0	11.0 ± 2.0
[011]	C	14.7 ± 0.5	20.0 ± 2.0	9.0 ± 1.0
[111]	C	19.5 ± 0.6	26.0 ± 2.0	12.0 ± 2.0

Table 2.2: Least squares fit coefficients and standard deviation values for parameters a, b and c in Eq. (2.2).

indicated by the superposed solid and dashed lines representing least square fits, where a, b and c are positive constants dependent on facet orientation and and T_c. Fit coefficients are listed in Table 2.2.

Shown in Fig. 2.4(b) is the reduction in L_T for increasing value ρ_c, where of course the value ρ_c cannot be specified but emerges naturally in response to the parameter values input into the simulation. Except for a few notable points, the thermal slip length generally decreases monotonically with increasing value ρ_c, reflecting the influence of the L/S coupling energy. The important result here is that either at the hotter or colder L/S interface, the thermal slip length is smallest for the [011] facet and largest for the [111] facet. The superposed solid and dashed lines indicate least square fits to the reciprocal function

$$L_T(\rho_c) = \frac{\alpha_1}{\rho_c - \alpha_2}\ , \tag{2.3}$$

Facet	H/C side	α_1	α_2
[001]	H	11.8 ± 0.4	0.88 ± 0.04
[011]	H	8.40 ± 1.0	0.17 ± 0.12
[111]	H	14.2 ± 0.3	1.00 ± 0.02
[001]	C	6.60 ± 0.2	0.94 ± 0.02
[011]	C	2.70 ± 0.9	0.63 ± 0.12
[111]	C	8.03 ± 0.4	1.03 ± 0.04

Table 2.3: Least squares fit coefficients and standard deviation values for parameters α_1 and α_2 in Eq. (2.3).

where α_1 and α_2 are positive constants that depend on facet orientation and T_c; fit constants are listed in Table 2.3. For the [011] facet, the data points for $\varepsilon_{LS} = 0.1, 0.2, 0.3$ on the colder side, and for $0.1 \leq \varepsilon_{LS} \leq 0.7$ on the hotter side deviate more significantly from the reciprocal relation, as indicated by the larger standard deviation values reported in Table 2.3. As mentioned earlier in this section and to be discussed in more detail in Section 2.3.2.6, the contact layer against the [011] facet undergoes a structural transition as a certain value of ε_{LS}, which varies with temperature. The data points in Fig. 2.4(b) which deviate most from the reciprocal relation in Eq. (2.3) represent those systems below the transition point. This transition induced by the [011] facet was also evident in Fig. 2.2(g) at the colder interface, but less noticeable at the hotter interface where ρ_c is not as sensitive to ε. No similar transition was observed for the [001] or [111] facet for the parameter range in this study.

Taken together, the results in Figs. 2.2(g), 2.3(d), and 2.4(b) are seemingly counterintuitive. For the same value ε_{LS}, a hotter or colder contact layer against the [011] facet generates the highest thermal flux J_z of all three facets despite having the smallest - not largest - contact density ρ_c . Therefore, a higher contact density does not uniquely predict a higher thermal flux (nor lower thermal resistance or higher thermal conductance), as sometimes suggested [17, 21, 29]. In the original AMM model proposed by Khalatnikov [31, 55], the relation governing the thermal boundary resistance for superfluid helium against a metal surface was shown to depend on several variables such as the local temperature, liquid pressure, elastic properties of the liquid and solid, and the excitation spectra of electrons and different phonon branches of the solid. An increase in one variable can therefore be offset by other factors or confounding variables such that no one variable is a unique predictor of TBR. The results shown in Figs. 2.2(a)–(f) do suggest that systems with the smallest depletion layer thickness, as for the [011] facet, do appear to maintain the highest thermal flux. Similar behavior [59] has been reported in NEMD simulations of L/S media described by more complex intermolecular potentials describing water on silicon and water on graphene coated silicon; however the depletion length in that study was defined somewhat differently.

2.3.2.4 Voronoi diagram, coordination number, and local bond-orientational order parameter

Some qualitative but crucial features of particle distribution within the contact layer are captured by the Voronoi diagrams presented in Fig. 2.5. Each Voronoi diagram is based on a snapshot of the contact layer randomly obtained over 5×10^5 time steps after thermal equilibration was complete. We compared the in-plane liquid distributions against the non-wetting interface ($\varepsilon_{LS} = 0.1$) and the strongly-wetting interface ($\varepsilon_{LS} = 1.0$) to analyze the wettability dependence of liquid structures against three facets at different temperatures. The coordination number of each particle is read from the number of edges comprising the Voronoi cell. To simplify current analysis, we focus exclusively on the populations

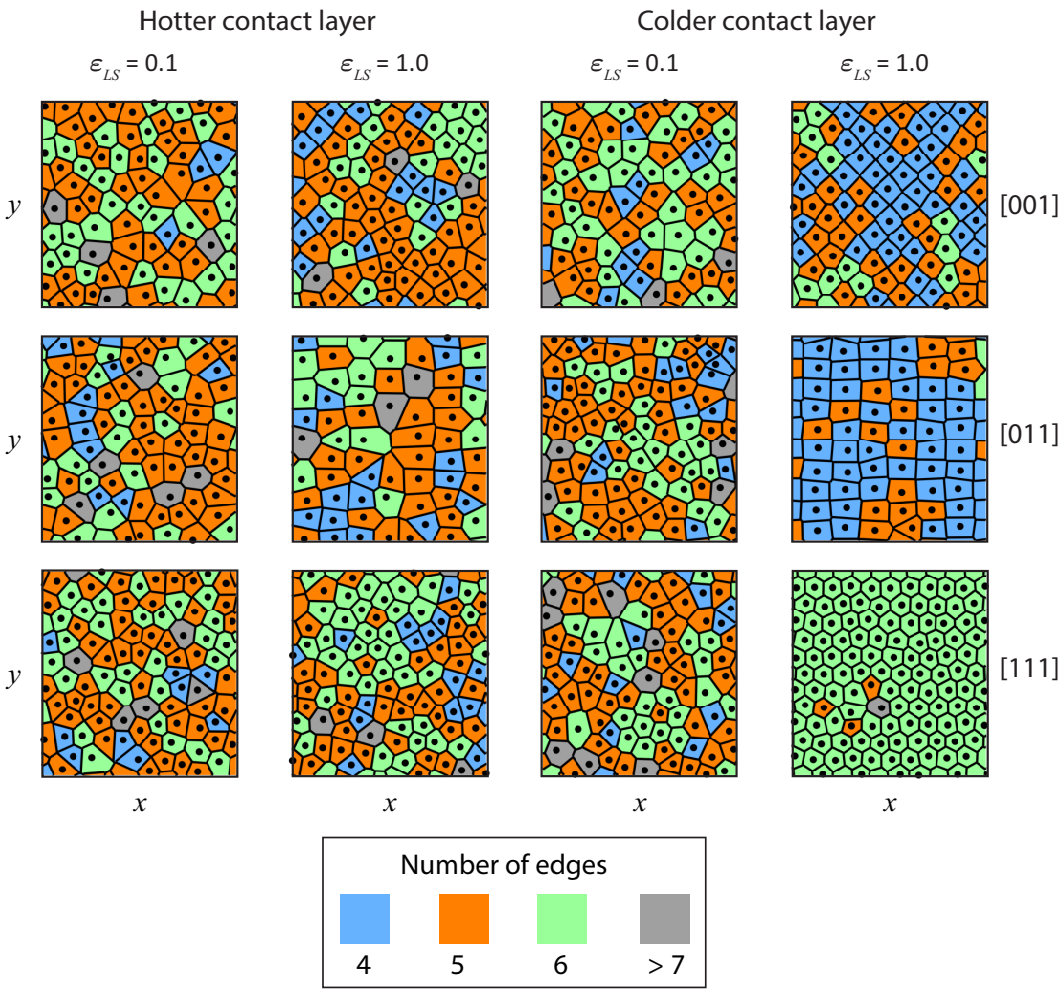

Figure 2.5: The Voronoi tessellations in the contact liquid layers across the colder (left two columns) and hotter (right two columns) FCC facets at $\varepsilon_{LS} = 0.1$ and 1.0. The number of edges comprising each cell is represented by the color scheme shown at the bottom.

of rectangular cells ($m = 4$), pentagonal cells ($m = 5$), and hexagonal cells ($m = 6$). It was confirmed in background that other shapes (triangular, heptagonal, and octagonal cells) comprise less than 5% of the Voronoi cells in all contact layers, so the restriction to $m = 4, 5, 6$ has no significant influence on discussions that follow.

We find that particle distributions within the hotter contacts layers are almost unaffected by the presence of the nearby solid even when the interface is strongly-wetting. For all three facets, the tessellations are predominantly occupied by pentagonal and hexagonal cells which seem to be distributed randomly (i.e., large clusters of pentagonal or hexagonal cells are not found). The apparent lack of the spatial ordering is due to thermally-induced particle diffusion which leads to frequent hopping from one equilibrium position to another. As indicated in Table 2.5, the numerically obtained temperatures inside the contact layers when $\varepsilon_{LS} = 1.0$ are 1.513 ± 0.004 for the [001] facet, 1.529 ± 0.006 for the [011] facet,

and 1.503 ± 0.007 for the [111] facet. Since T_c is equivalent to average kinetic energy of a single particle in two-dimensional system, thermal energy per particle is approximately 50% larger than $\varepsilon_{LS} = 1.0$ in these three cases. Thus, particle dynamics at the hotter interface is thermally-driven, and liquid particles continuously diffuse within the contact layer until they suddenly jump to the adjacent liquid layer. Because $0.1 \leq \varepsilon_{LS} \leq 1.0$ is smaller in magnitude compared to thermal energy, it naturally follows that liquid particle distributions are nearly independent of L/S wettability or facet structure.

On the other hand, particle distributions within the colder contact layers inherit periodic patterns of the crystalline surfaces when L/S binding energy is $\varepsilon_{LS} = 1.0$. From Table 2.5, the temperatures within the contact layers are 1.089 ± 0.004 for the [001] facet, 1.074 ± 0.004 for the [011] facet, and 1.095 ± 0.004 for the [111] facet. All temperature measurements are within 10% of L/S binding energy, so L/S binding exerts comparable effects on particle dynamics within the contact layer under strongly-wetting interaction. Consequently, the Voronoi diagrams corresponding to the [001], [011], and [111] facets are predominantly occupied by squares, rectangles, and hexagons, respectively. The long-range spatial ordering corresponding to the respective facet is observed in all three contact layers. Thus, phase transition from the liquid-like to solid-like structures is likely taking place in the contact layer as ε_{LS} approaches thermal energy from the equipartition theorem.

The coordination number distribution f_m was computed as $f_m = \langle N_m/N_c \rangle$ where N_m is the number of Voronoi cells with m edges, N_c is the total number of Voronoi cells in a snapshot, and the angle brackets denote time averaging whose procedure was detailed in Section 1.3. The distributions corresponding to $m = 4, 5, 6$ are plotted against $0.1 \leq \varepsilon_{LS} \leq 1.0$ in Fig. 2.6. In the non-wetting regime ($\varepsilon_{LS} \lesssim 0.3$), the average distributions of rectangular, pentagonal, and hexagonal cells are nearly identical in all three facets, and they are ($f_4 \approx 0.10$, $f_5 \approx 0.50$, $f_6 \approx 0.35$). At the hotter interface, f_m remains nearly unchanged as ε_{LS} is increased to 1.0 for any m (weak dependence on surface wettability). On the other hand, the stronger wettability dependence is observed at the colder interface. When ε_{LS} is increased, f_m corresponding to the symmetrical structure of the solid surface increases rapidly (i.e., $m = 4$ for [001] and [011], and $m = 6$ for [111]). As seen in Fig. 2.6(a), f_4 for the [011] facet is greater than that for [001] for any ε_{LS}. The relative population of pentagonal cells in Fig. 2.6(b) decays moderately when ε_{LS} is increased, but it is less sensitive to the L/S coupling compared to f_4 or f_6.

The symmetrical structures seen in the Voronoi diagrams are further quantified using the bond-orientational order parameter [Eq. (1.11)] for $m = 4, 5, 6$. As seen in Fig. 2.6(d), ψ_4 corresponding to the colder [001] facet and colder/hotter [011] facet increases abruptly as ε_{LS} is increased to 1.0 as if the phase transition is taking place. For the colder [001] facet, ψ_4 deviates significantly from zero near $\varepsilon_{LS} \approx 0.7$, but no analogous behavior is seen for the hotter [001] facet. The colder and hotter [011] facets undergo this phase transition at

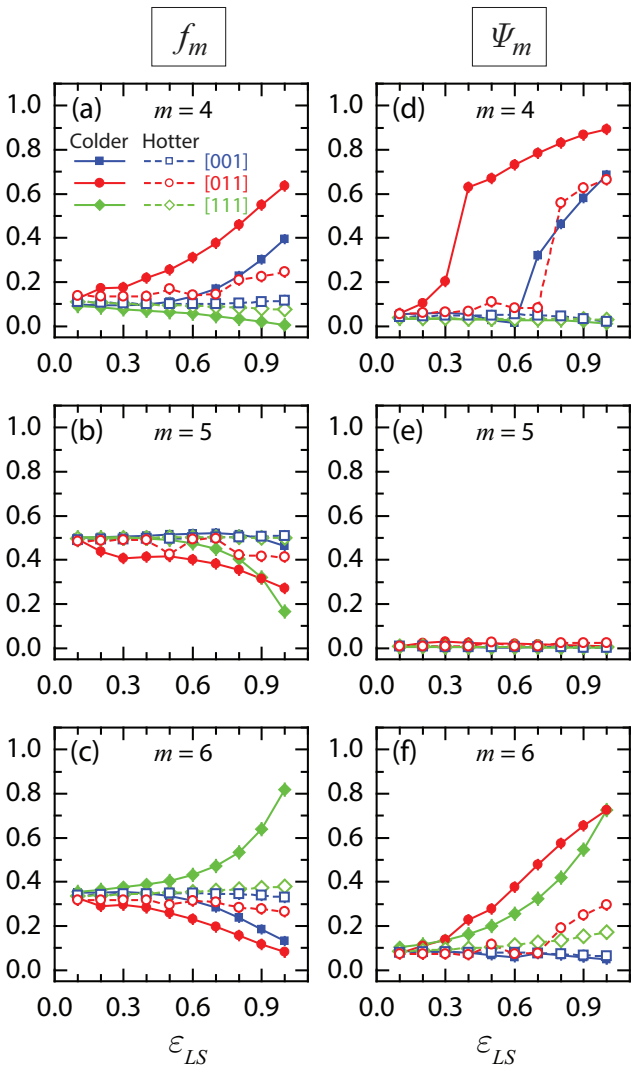

Figure 2.6: Time-averaged quantities characterizing the rotational symmetries observed in the contact liquid layers across three FCC facets. (a)–(c) The fraction f_m of Voronoi cells with m vertices ($m = 4, 5, 6$), and (d)–(f) the corresponding bond-orientational order parameter $|\psi_m|$ across three FCC facets, all plotted against ε_{LS}. The consecutive symbols are connected by line segments for visual clarity.

$\varepsilon_{LS} \approx 0.4$ and 0.8, respectively, both of which are well below the corresponding values for the colder and hotter [001] facets. Moreover, irrespective of the local temperature, ψ_4 for the [011] facet is consistently larger than that for the [001] facet once the phase transition takes place. This analysis suggests that the interfacial liquid structure against the [011] facet develops stronger 4-fold rotational symmetry compared to that against the [001] facet. Not surprisingly, ψ_4 for the [111] facet remains smaller than 0.1 over the range $0.1 \leq \varepsilon_{LS} \leq 1.0$.

As seen in Fig. 2.6(e), the extracted values of ψ_5 are vanishingly small for all interfaces examined in this work. While this is not particular unexpected given that three solid

facets lack the 5-fold rotational symmetry, it is noteworthy that the considerable fraction of pentagonal cells indicated in Fig. 2.6(b) makes no contribution to the structural symmetry in the contact layer, i.e., the pentagonal cells in the Voronoi diagrams represent purely disordered states. Finally, ψ_6 versus ε_{LS} in Fig. 2.6(f) indicates the strong presence of 6-fold symmetric structure against the [011] and [111] facets. An increase of ψ_6 with respect to ε_{LS} is gradual, and no abrupt behavior is seen as in the case of ψ_4 in Fig. 2.6(d). Despite the obvious hexagonal structure of the [111] facet, the extracted values of ψ_6 are larger against the [011] facet under the strongly-wetting L/S interaction for both the colder and hotter interfaces. This is rather surprising given the dominating presence of hexagonal Voronoi cells for the [111] facet in Fig. 2.5.

2.3.2.5 2D radial distribution function

Shown in Fig. 2.7 are the 2D radial distribution functions $g^{\parallel}(r)$ for particles in the contact layer at the hotter and colder interfaces for three facet orientations with increasing value ε_{LS}. Also superimposed are the results for the first crystal plane for $\varepsilon_{LS} = 1.0$ and the interior liquid. It was determined (not shown) that $g^{\parallel}(r)$ within the interior liquid and first crystal plane varied weakly with ε_{LS}. The lack of sensitivity to ε_{LS} of the interior liquid region is likely due to the fact that the layer thickness was fairly large and the interior region therefore well shielded from the L/S interface. We also recall that the crystal solid used in this study was constructed using large ratios $\varepsilon_{SS}/\varepsilon_{LS}$ of the order of 10 to 100, thereby reducing sensitivity of $g^{\parallel}(r)$ for the first crystal plane to changes in ε_{LS}.

As expected, the colder the interface temperature and the stronger the L/S coupling, the stronger the commensurability between the radial distribution of particles within the contact layer and those of the adjacent crystal facet. For the [011] facet, comparison of the distribution function $g^{\parallel}(r)$ between the contact layer and interior liquid reveals that at smaller values ε_{LS}, the location and shape of the first two liquid peaks almost superimpose, with a small but gradual increase in the mismatch as r increases. This indicates that the local spatial distribution of particles in the contact layer is more isotropic and more liquid-like than for the contact layers against the [001] and [111] facet. This is especially evident for the colder contact layer for $\varepsilon_{LS} \leq 0.3$ and the hotter contact layer for $\varepsilon_{LS} \leq 0.7$. Notably, this is the same parameter range which we noted earlier gave rise to the deviations in the reciprocal functions shown in Fig. 2.4(b). Also evident from Fig. 2.7 is that while the contact layer against the [001] and [111] facet undergoes a smooth and gradual increase in $g^{\parallel}(r)$ as ε_{LS} increases, the layer against the [011] facet manifests an abrupt jump in behavior, indicative of the structural transition noted earlier.

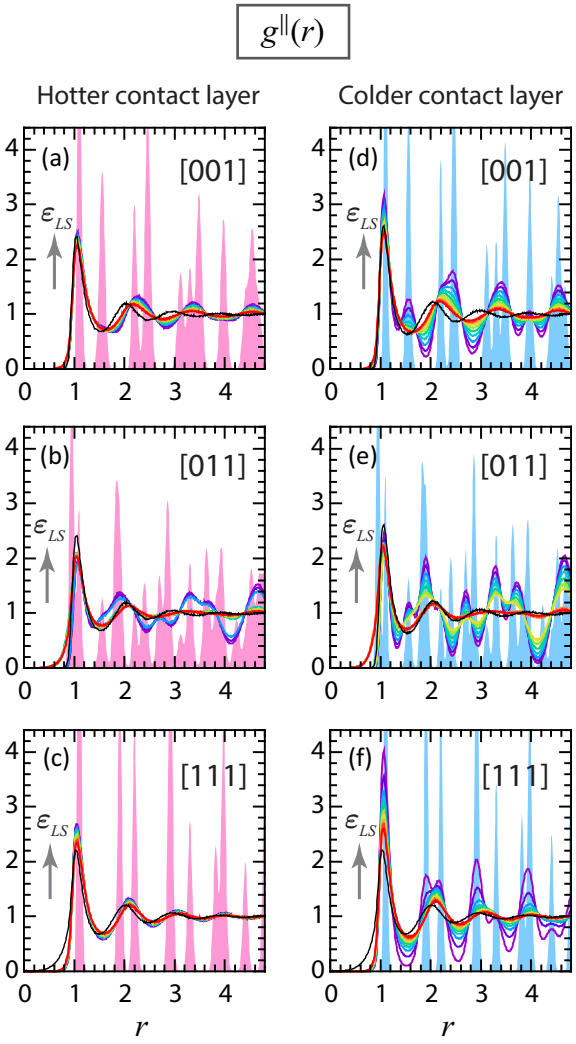

Figure 2.7: 2D radial distribution function $g^{\parallel}(r)$ given by Eq. (1.9) for (a)–(c) hotter and (d)–(f) colder contact layers (colored curves) for $0 \leq \varepsilon_{LS} \leq 1.0$ in increments of 0.1 and three facets. Shown for comparison is the distribution for the interior liquid (black curve) as well as the first crystal plane for $\varepsilon_{LS} = 1.0$ (red and blue shaded peaks).

2.3.2.6 2D static structure factor

The results in Fig. 2.8 for the static 2D structure factor given by Eq. (1.10) provide additional insight into the degree of commensurability between the organization of particles in the contact layer and first crystal plane. The logarithmic color scale in Fig. 2.8 spans three orders of magnitude. Generally, for the same value ε, the colder the contact layer, the closer the structure factor resembles that of the crystal facet, as indicated by the set of discrete points reflecting the maxima. The hotter the contact layer, the more fluid-like the particle packing, as indicated by the circular ring patterns. For all facets, the hotter contact layers for $\varepsilon_{LS} = 1.0$ show stronger commensurability with the underlying crystal facet than

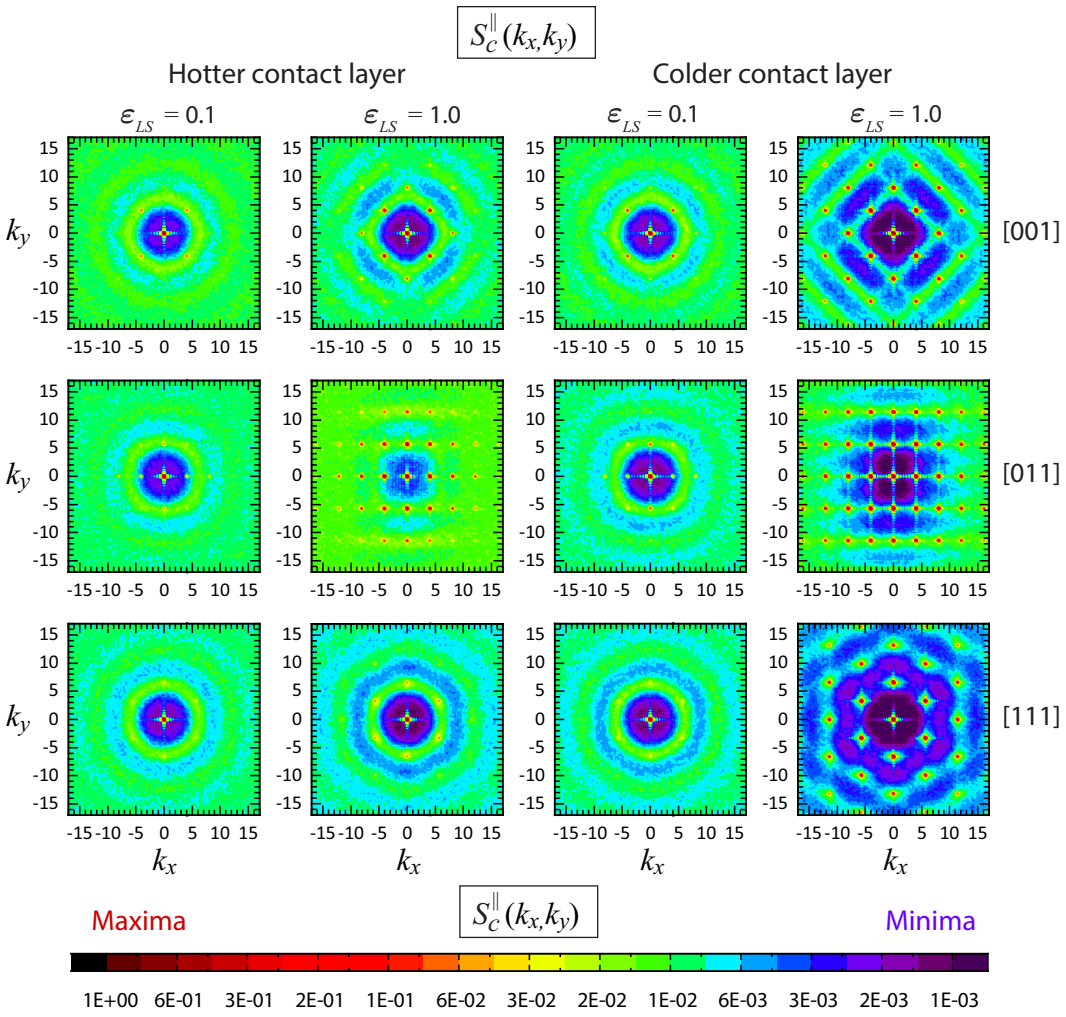

Figure 2.8: Static 2D structure factor $S_c^{\parallel}(k_x, k_y)$ [Eq. (1.10)] for the hotter and colder contact layer for two values of L/S interaction energy and three facet orientations. Maximal values appear as small solid red dots.

do the colder contact layers for $\varepsilon_{LS} = 0.1$. Most notably, for either $\varepsilon_{LS} = 0.1$ or 1.0, the [011] facet always induces much longer-range translational order within the contact layer than do the other two facets.

Closer inspection of the images in Fig. 2.8 and other images for different values of ε_{LS} (not shown) reveals that while the global maxima (small red solid dots) of $S_c^{\parallel}(k_x, k_y)$ for the [001] or [111] case always align with the wave vectors defining the shortest RLVs, the [011] case behaves differently due to the structural transition noted earlier. For $\varepsilon_{LS} = 0.1$, which is below the transition value, the maxima of $S_c^{\parallel}(k_x, k_y)$ coincide not with the smallest but the second smallest RLVs, specified in Table 1.4). For $\varepsilon_{LS} = 1.0$, which is above the transition, the maxima occur at the shortest RLVs of the crystal facet. Based on a review of the data for all choices ε_{LS}, the real space configuration of particles in the colder contact layer is

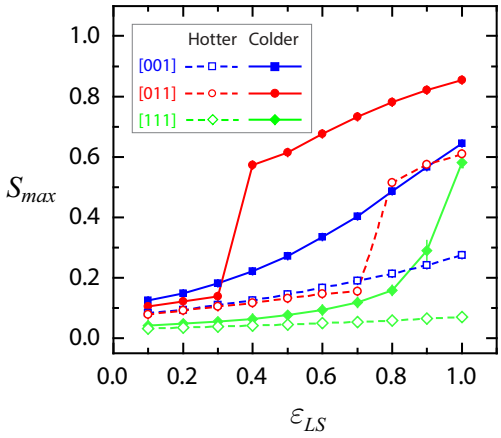

Figure 2.9: Maxima of the static 2D structure factor S_{max} extracted from Eq. (1.10) for particles in the hotter and colder contact layer for three facets and $0 \leq \varepsilon_{LS} \leq 1.0$ in increments of 0.1. Connecting segments are only a guide to the eye. Coordinates of the relevant reciprocal lattice vectors are listed in Table 1.4.

characterized by a preferential alignment of particles along the $\hat{x}$ axis for $\varepsilon_{LS} \leq 0.3$ and preferential alignment along the $\hat{y}$ axis for $\varepsilon_{LS} \geq 0.4$. This switch in alignment also occurs within the hotter layer in crossing the value $0.7 \leq \varepsilon_{LS} \leq 0.8$. This additional information further informs the trends noted earlier in Fig. 2.6(d)–(f) and Fig. 2.7.

The maxima of $S_c^{\parallel}(k_x, k_y)$, denoted by $S_{max} = S_c^{\parallel}(k_{o,x}, k_{o,y})$, are plotted in Fig. 2.9 for increasing value ε_{LS}. For the [111] case, the results show greater sensitivity to ε_{LS} for the colder layer, as expected. Also, while S_{max} for the [001] and [111] facets shows a smooth and gradual increase with increasing ε_{LS}, the [011] case manifests sizeable jumps at $0.7 \leq \varepsilon_{LS} \leq 0.8$ in the hotter layer and at $0.3 \leq \varepsilon_{LS} \leq 0.4$ for the colder layer. These jumps correspond exactly to the switch in particle alignment which occurs for liquid particles against the [011] facet. Above the transition, the values S_{max} for the [011] case always and significantly exceed the values for the other two facets. Therefore particle alignment along the $\hat{y}$ axis reflects much stronger commensurability with the periodic pattern set by the corrugation of the crystal surface potential. Below the transition value, S_{max} for the colder layer against the [001] facet slightly exceeds that for the [011] facet but this difference altogether disappears at higher temperatures.

2.3.3 Characterization of contact layer by time-dependent quantities

2.3.3.1 2D mean squared displacemen

Shown in Fig. 2.10 are sample snapshots from individual runs of the location of particles in the hotter and colder contact layer for two values of ε_{LS} and three facet orientations. The time t_{exit} denotes the instant after which one of four randomly tagged particles escaped the contact layer. Accurate inferences about particle motion and dynamics, of course, requires

extensive ensemble averaging, as discussed in Section 1.3. However, the instantaneous snapshots from a single run nonetheless reveal a few interesting trends, later supported by proper ensemble averaging as discussed later in this section.

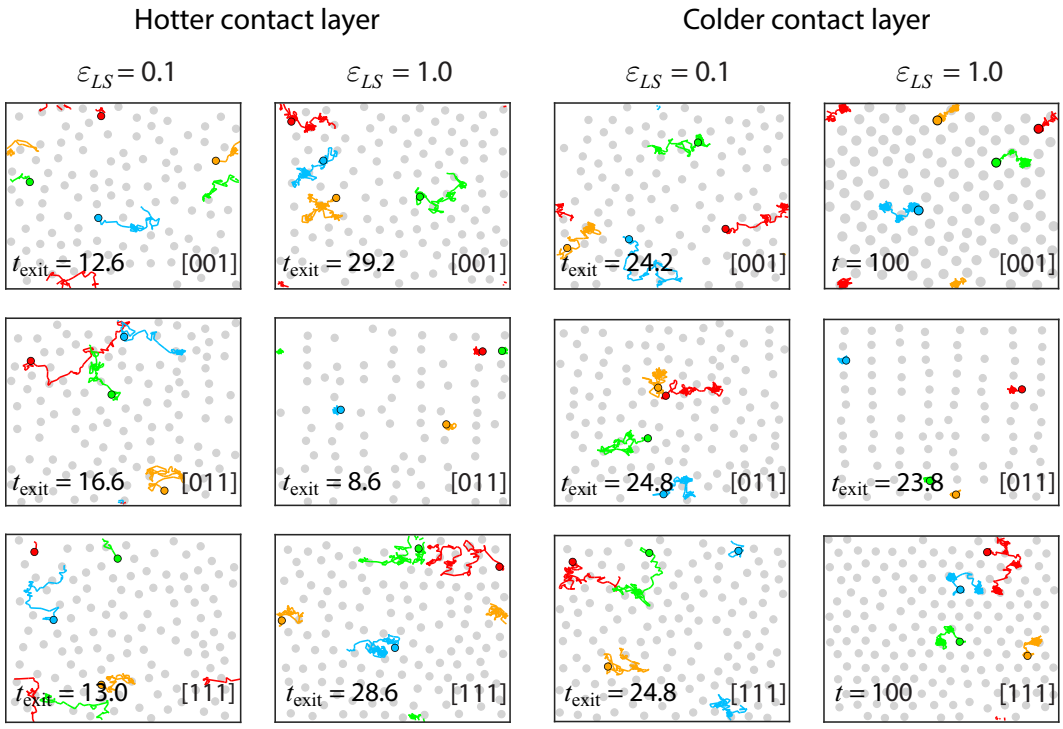

Figure 2.10: Sample snapshots from individual runs showing the position of particles in the contact layer at time t_{exit} (grey dots). Highlighted are the trajectories (red, green, yellow and blue segments) of four randomly tagged particles with their final location at $t = t_{\text{exit}}$ indicated by a black circle. For the two images marked $t = 100$, all four tagged particles remained within the contact layer at least through that time.

For a given facet with $\varepsilon_{LS} = 1.0$, a colder contact layer maintains a higher liquid surface density and longer particle residence times, as expected. Also, such layers more strongly adopt the dimensions and symmetry of the adjacent crystal surface potential, an effect which is not as evident to the eye for $\varepsilon_{LS} = 0.1$. For $\varepsilon_{LS} = 1.0$, perhaps the most interesting feature is that particles against either the hotter or colder [011] facet undergo the shortest displacement from their initial position, likely indicative of tighter binding with the solid surface, and yet experience the *smallest residence times* in comparison to the results for the other two facets. This tentative observation, based only on a few single snapshots, suggests that particles against the [011] facet more readily escape the layer perhaps in response to hindered diffusion in-plane. In what follows, we support this hypothesis with a more comprehensive set of data extracted from many more particle trajectories, which are properly ensemble averaged.

Some key features of the contact layer become evident when examining temporal correlations

obtained by extensive ensemble and block averaging of single particle trajectories. Shown in Fig. 2.11 is the 2D mean square displacement $MSD_c^{\parallel}(t)$ plotted on logarithmic axes for particles in the hotter and colder contact layer for three facet orientations and $0.1 \leq \varepsilon_{LS} \leq 1.0$. These results are exclusively based on particles which never left the contact layer throughout the measurement interval shown. As described in Section 1.3.3, the measurement interval was terminated once fewer than ten particles satisfied that minimum occupancy condition. Runs conducted with different input parameter values therefore yielded different terminal times.

The superposed lines in Fig. 2.11(a)–(f) signify the theoretical exponents for the early (E) and late (L) time motion of a particle in a bulk homogeneous isotropic fluid far from any boundary or interface. These exponent values describe ideal ballistic motion ($\gamma_E = 2$) and diffusive motion ($\gamma_L = 1$). In all cases for the system under study, the influence of the crystal surface potential diminishes the magnitude of these exponents, as evident in Fig. 2.12. In Table 2.7, the exponents for γ_E were extracted from least square fits over the interval $0.02 \leq t \leq 0.10$ and for γ_L over the interval spanning the last decade in time. For motion showing plateau-like response following the (sub) ballistic regime, as observed for the colder [011] facet for $\varepsilon \geq 0.4$ or hotter [011] facet for $\varepsilon \geq 0.8$, the least squares fits were extracted using only the last half-decade. This is because for some parameter values, the plateau-like regime extended only a short period and it was preferable in extracting exponent values to use the same interval in time. Nevertheless, it is clear that the 2D mean square displacement of particles against the [011] facet exhibits the largest departure from the ideal value $\gamma_L = 1$, reflecting a significant retarding influence from the crystal surface potential.

The results in Fig. 2.11 confirm some interesting features. The behavior of particles against the [001] and [111] facets show a smooth transition from sub-ballistic to sub-diffusive motion, with a gradual reduction in the magnitudes of γ_E and γ_L with increasing value ε_{LS}. By contrast, particles against the [011] facet experience a significant slowdown following the sub-ballistic regime, with a notable drop in the value γ_E exactly at the values of ε_{LS} where there occurs a structural transition discussed earlier. The motion both prior and subsequent to this transition is indicative of 2D caged motion whereby longer excursions from diffusive-like motion are severely repressed. Below the transition in ε_{LS}, caged motion is weaker. Above the transition, particle localization is enhanced and caging quite strong. Against the colder [001] and [111] facets, one also observes a small transient slowdown in mean square displacement quickly followed by a longer sub-diffusive regime. The caged motion induced by the colder [001] and [111] facets is very weak, even for the largest values of ε_{LS}.

The fitted power law exponents plotted in Fig. 2.12 and tabulated in Table 2.7 reveal some interesting features. For all parameter ranges tested, the exponents γ_E, which span the limited range $1.83 \lesssim \gamma_E \lesssim 1.90$, are always smaller than the ideal value 2.0. The motion

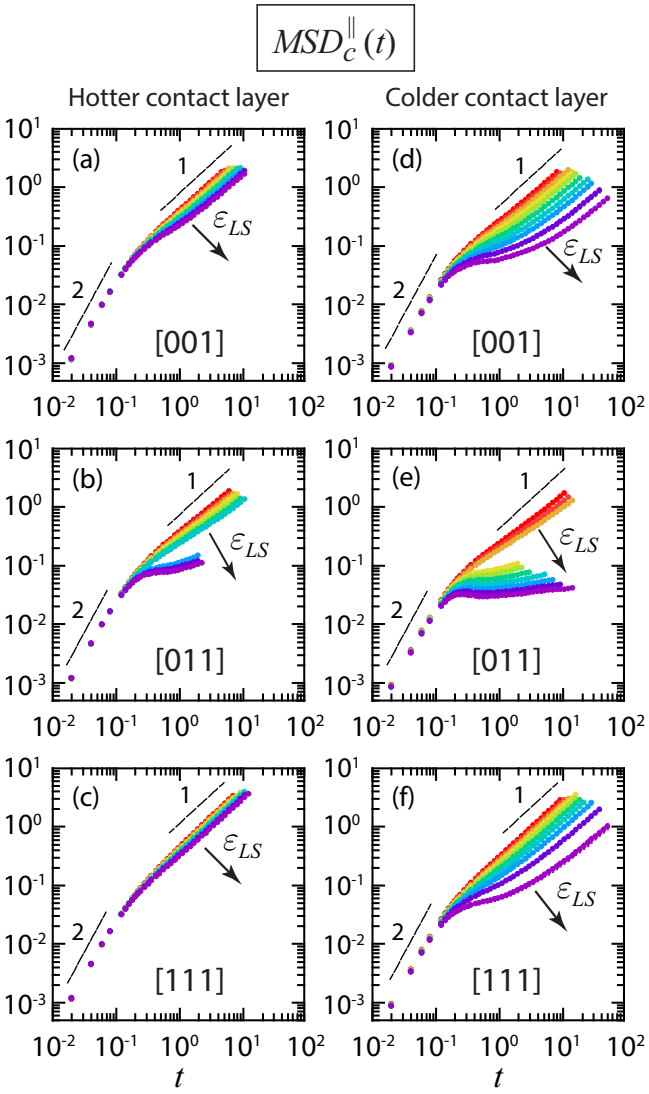

Figure 2.11: 2D Mean square displacement $MSD_c^{\parallel}(t)$ given by Eq. (1.12) at (a)–(c) hotter and (d)–(f) colder L/S interfaces for three facets and $0.1 \leq \varepsilon_{LS} \leq 1.0$ in increments of 0.1. The data shown is restricted to trajectories of particles ten or more of which remain within contact layer throughout entire measurement interval. Superposed lines denote exponent values for ideal ballistic (γ_E) and ideal diffusive (γ_L) motion. Vertical lines through icons signify standard deviation.

of particles in the contact layer is therefore slowed in comparison to ideal ballistic motion in a simple homogenous fluid but not by much. Furthermore, the values γ_E are relatively insensitive to facet orientation and temperature and exhibit only a slight decrease as ε_{LS} increases. This minor reduction in exponent is expected since ballistic-like motion is by its very nature inertia-dominated [36] and therefore should not be as sensitive to the influence of the crystal surface potential. For a simple bulk homogenous and isotropic fluid, the mean square displacement in the ballistic regime scales according to $T \times t^2$ (i.e., $(k_B T/m)t^2$

in dimensional units). (Incorporation of hydrodynamic memory effects [26, 82] is known to alter this relation slightly such that the particle mass m is replaced by a slightly larger effective mass to account for the fraction of surrounding fluid displaced by the motion of the particle.) The entries in Table 2.7 and corresponding values of the contact layer temperature T_c in Table 2.6 confirm that hotter particles undergo larger mean square displacement even in the presence of a corrugated surface potential for the values ε_{LS} tested.

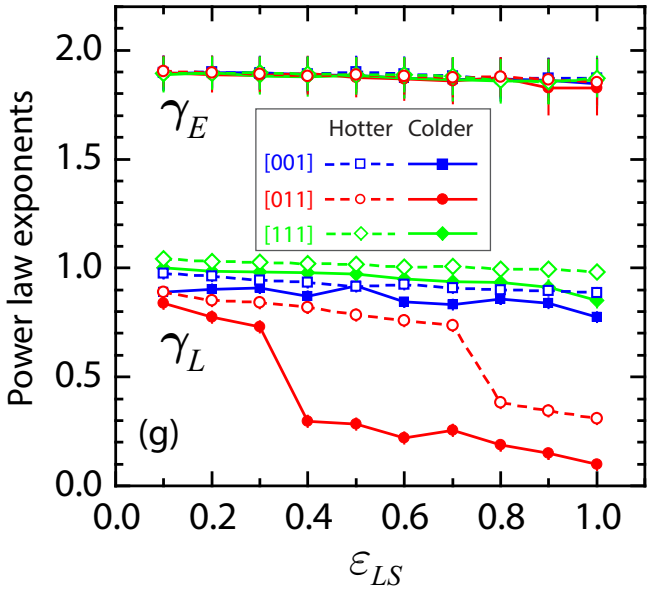

Figure 2.12: Exponents extracted from least squares fit to data in Fig. 2.11. Connecting segments are a guide to the eye.

As shown in Fig. 2.12, the exponents γ_L span a much wider range and they too fall below the ideal value 1.0. At late times then, particle motion in the contact layer experiences significant slowdown due to the influence of the periodically corrugated crystal surface potential. For similar parameter values, liquid particles against the [011] facet undergo the smallest 2D mean square displacement, while particles against the [111] facet undergo the largest. Below the structural transition in ε_{LS} for particles against the [011] facet discussed earlier, the values γ_L manifest sizeable jumps. Together with the results in Fig. 2.9, this implies that the longer range the 2D structural order, induced by colder temperature and/or larger values of ε, the smaller the 2D mean square displacement. Clearly, the hindrance or suppression of 2D diffusive-like motion in the contact layer is caused by significant energy barriers established by the corrugated crystal surface potential.

The caged motion inferred from γ_L for the [011] case, especially notable above the structural transition, can also be seen in Figs. 2.11(b) and (e), where there occurs a distinct plateau-like region with a small or vanishing slope. For the colder layer at higher values of ε_{LS}, the 2D mean square displacement practically stalls due to significant particle localization. This behavior spans about one decade in time for the hotter layers and almost two decades in time

for the colder layers. Near $t \gtrsim 10^{-1}$ for larger values of ε_{LS}, the motion briefly reverses as particles undergo recoil within dynamic cages just prior to onset of the 2D caged regime. At higher temperatures and smaller values of ε_{LS}, this recoil is far less pronounced.

Generally, the terminal time increases as ε_{LS} increases. This is expected since larger L/S bonding energy should cause more particles to remain situated within the contact layer for longer periods of time before escaping to a subsequent liquid layer. In comparing behavior against different facets for similar parameter values, we note that the [011] case for values ε_{LS} below the structural transition yields terminal times only slightly longer than those for the other two facets. However above the transition, the results in Figs. 2.11(b) and (e) show a steep drop in $MSD_c^{\parallel}(t)$ and very short terminal times, which are almost an order of magnitude *smaller* - not larger - than for the other two facets. Therefore, while the planar motion of particles in the contact layer is severely repressed by 2D caged motion, the caged particles escape more rapidly into the third dimension, so to speak, funneling thermal energy toward the colder solid more rapidly.

We recall that under steady state conditions, as in this study, the average density of particles in each liquid layer remains fairly constant, dependent on the local temperature and pressure. On average then, for every particle that leaves the contact layer, another replaces it. At the hotter L/S interface, the caged motion helps funnel hotter more energetic particles to the next liquid layer along the $+\hat{z}$ axis, which is cooler. At the colder L/S interface, the caged motion helps funnel colder less energetic particles to the next liquid layer along the $-\hat{z}$ axis, which is warmer. These particles are rapidly replaced by hotter particles from the warmer layer, which then transfer energy to the first crystalline layer. In either case, the 2D caging motion against the [011] facet enhances thermal transfer near the interface when compared to the other two facets.

The 2D caged motion against the [011] facet we have described is unlike the 3D caged motion observed in equilibrium simulations of glass-forming liquids. Glassy dynamics has been studied in simple hard sphere models as the concentration approaches approaches the critical packing fraction [15] and in binary mixtures of LJ particles upon approach to the vitrification temperature [35]. Three dimensional caged motion is known to occur in complex fluids such as water, molten silicon, polymers and long chain biological molecules, in part due to more complex intermolecular potentials which are orientation dependent. The formation of a plateau-like region in the 3D mean square displacement signaling 3D caging is normally attributed to two effects. Not only are individual particles trapped in cages formed by neighboring particles, but those neighbors are also situated within other cages, thereby causing a significant slowing in the overall motion [34]. In such systems, the colder the temperature and the stronger the particle interaction energy, the stronger the 3D dynamic cage and the longer the confinement time before re-escape and re-trapping by another cage. By contrast in our system, the colder the temperature and the stronger the L/S interaction

energy, the stronger the 2D dynamic cage but the shorter the confinement time and the more rapid the escape to the adjacent liquid layer.

2.3.3.2 2D and 3D velocity autocorrelation function

Caged motion can also be inferred from the velocity autocorrelation function. Early simulations of fluids in equilibrium modeled as LJ particles interacting via a soft repulsive potential like $U(r) = \varepsilon_{LL}(\sigma/r)^{15}$ showed that upon approach to vitrification, there develops a period of negative velocity autocorrelation immediately following the early ballistic regime [12, 13]. This behavior has been attributed to the reversed motion of a particle undergoing collisions with neighboring particles which encircle it by a temporary mobile cage; the inclusion of attractive forces enhances the cohesiveness or strength of the cage thereby prolonging the period of transient confinement.

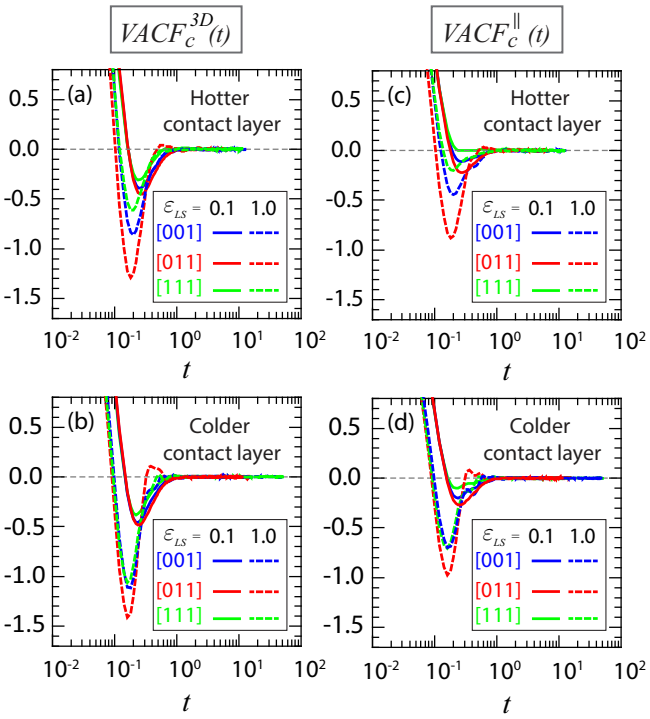

Figure 2.13: Velocity autocorrelation function $VACF_c(t)$ given by Eq. (1.15) for three facets and $\varepsilon_{LS} = 0.1$ and 1.0 for trajectories of particles ten or more of which remain within the contact layer throughout the measurement interval. Superscripts $3D$ and $\parallel$ denote evaluation of Eq. (1.15) based either on $3D$ or in-plane $2D$ velocity vectors, respectively.

Transient negative autocorrelation is also seen in Fig. 2.13 showing the results for $VACF_c^{3D}(t)$ and $VACF_c^{\parallel}(t)$. Comparing the time intervals here with the 2D mean square displacement in Fig. 2.11, it appears that the start of the negative autocorrelation coincides with the end of the sub-ballistic regime and onset of 2D caged regime. As expected, the amplitude of the negative autocorrelation is larger for particles inside a colder contact layer due to the

reduction in particle kinetic energy. Contrasting the behavior for $\varepsilon_{LS} = 0.1$ *and* 1.0 shows a more pronounced oscillatory behavior about zero upon escape from a transient 2D cage; these oscillations are related to stronger memory effects associated with stronger influence from the periodic crystal surface potential. The results also indicate a there is a stronger dependence on facet orientation and layer temperature for $\varepsilon_{LS} = 1.0$ than $\varepsilon_{LS} = 0.1$, again highlighting the influence of the periodic surface potential on nearby liquid motion. The special character of motion within a contact layer against the [011] facet is again evident. For the same value ε_{LS} and similar layer temperature, the [011] facet induces the *strongest* yet *shortest* period of localization due to 2D caging quantified by the larger amplitude but shorter period of negative velocity autocorrelation. For all parameter values tested, the velocity autocorrelation function was found to decay to zero beyond $t \gtrsim 1.0$. The results indicate that the caging effect is strongest for the [011] case and weakest for the [111] case.

The liquid behavior against the [011] facet exhibits another key feature most easily seen in Fig. 2.13 for $\varepsilon_{LS} = 1.0$. Following the negative autocorrelation period in $VACF_c^{3D}(t)$ or $VACF_c^{\parallel}(t)$, only the [011] case gives rise to subsequent positive values. Furthermore, the average time spent confined within a dynamic cage, as measured from the time interval between zero crossing points for transient trapping and escape, is shortest for particles in the colder – not hotter – layer, a seemingly counter-intuitive result. As discussed previously in evaluating the results of Figs. 2.11(b) and (e), for values of ε_{LS} above the structural transition in the contact layer, particles adjacent to the [011] facet escape more rapidly. As confirmed too by the results in Fig. 2.13 for the [011] case as well, despite that such particles experience stronger 2D caged motion and therefore smaller 2D mean square displacements, caged particles escape more rapidly into the third dimension, i.e., subsequent liquid layers.

Finally, while the curves for $VACF_c^{3D}(t)$ and $VACF_c^{\parallel}(t)$ appear generally similar, there is an important distinction worth noting. Comparison of the amplitude for the negative autocorrelation between the three facets and different layer temperatures for $\varepsilon_{LS} = 1.0$ reveals that the dominant contribution to the results shown stems from 2D motion within the contact layer. This is also true for $\varepsilon_{LS} = 0.1$ although the effect is less pronounced due to less of an influence from the periodic solid surface potential. This suggests that irrespective of layer temperature and facet orientation, most of the time spent in caged motion is caused by repeated transient trapping and escape while confined to the contact layer and less so from confinement effects in the out-of-plane direction ($\hat{z}$ axis) caused by the liquid layering in Fig. 2.2.

2.3.3.3 2D self-intermediate scattering function

The strength of caged motion is typically quantified by the 2D self-intermediate scattering function (SISF) $F_c^{\parallel}(\vec{k}_o, t)$ defined in Eq. (1.13), where $\vec{k}_o$ is the wave vector corresponding to the first peak in the structure factor. The results in Fig. 2.14 show that only for a small

parameter set and only for the [111] case does the motion undergo a direct transition from ballistic-like to diffusive-like dynamics. The trajectories of particles in those contact layers are therefore the most liquid-like. All other curves in Fig. 2.14 exhibit some degree of caged motion terminating at a non-zero value, without subsequent diffusive-like decay. For large ε_{LS}, the colder [111] facet induces an unusual signature as well marked by a lengthy interval of negative constant slope, behavior not seen in 3D glassy systems either. Re-inspection of the 2D radial distribution in Fig. 2.7, 2D structure factor in Fig. 2.8 and snapshots in Fig. 2.10 indicate that the negative slope is likely due to the formation of an epitaxial contact layer.

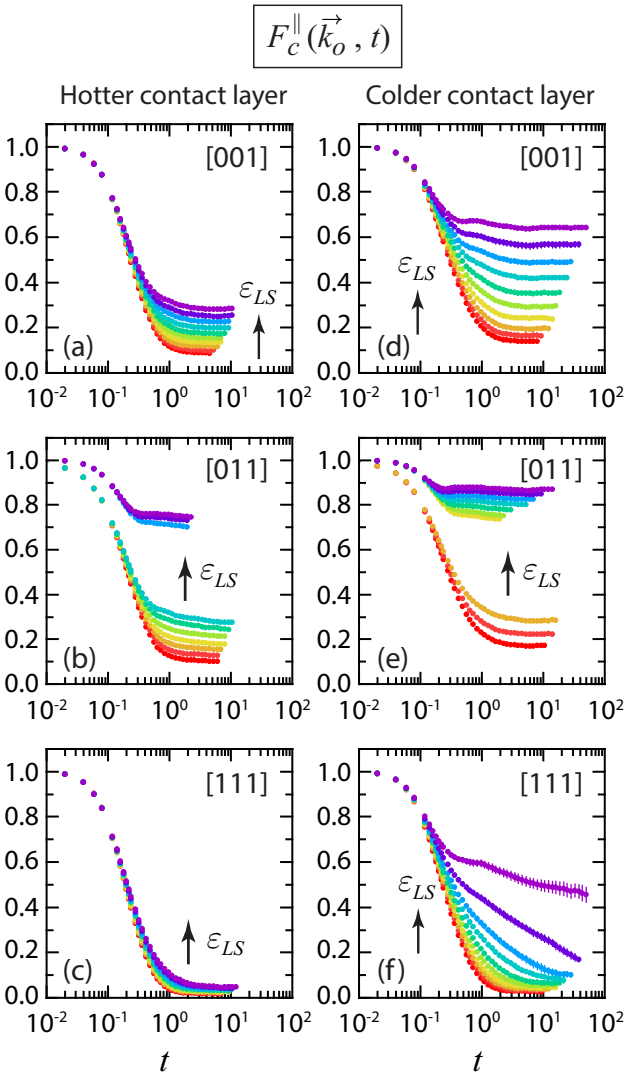

Figure 2.14: Self-intermediate scattering function $F_c^{\parallel}(\vec{k}_o, t)$ given by Eq. (1.13) at (a)–(c) hotter and (d)–(f) colder L/S interfaces for three facets and $0.1 \leq \varepsilon_{LS} \leq 1.0$ in increments of 0.1. Wave number coordinates of the reciprocal lattice vectors corresponding to the maxima of the 2D static in-plane structure factor are listed in Table 1.4. Vertical lines through icons signify standard deviation (not visible when smaller than icon size).

In conventional glassy systems undergoing caged motion, the 3D counterpart of Eq. (1.13) exhibits three distinct regimes: early ballistic, intermediate caging (plateau) and late time diffusion. Numerous studies have shown that in many 3D glassy systems, the SISF from early to late times can be fit by a double stretched exponential, each term represented by the Kohlrausch-Williams-Watt function. The onset of the plateau signals the transition from ergodic to non-ergodic behavior; for this reason, the amplitude of the plateau region is called the non-ergodicity parameter [35, 48, 85]. This fitting function remains ever popular since the extracted time constants provide estimates of the average relaxation times associated with early ballistic and late time diffusive motion.

In the system under study, however, with the exception of the [111] facet for small ε_{LS}, the majority of curves in Fig. 2.14 cannot be fit by the usual double exponential function since they do not asymptote to zero despite that the measurement interval extends three to four decades in time. Instead, the curves terminate at a non-zero value, whose magnitude depends on ε_{LS}, facet and temperature. Generally, it appears that the colder the layer temperature or the larger the value ε_{LS}, the more prolonged the plateau-like region and the larger the value F^*).

The influence of facet orientation highlights some special features of the [011] case. The curves in Fig. 2.14(b) and (e) are well separated by a large gap due to the structural transition described earlier in Fig. 2.9 and Fig. 2.12. The two sets of curves exhibit different character. For smaller values ε_{LS}, the curves look like typical 3D SISF curves describing unhindered motion in a homogeneous isotropic fluid except that the diffusive tail never decays to zero. The non-zero asymptotic value of the SISF below the structural transition implies persistent autocorrelation while undergoing diffusion caused by influence of the periodic corrugation of the crystal surface potential. Above the transition, the SISF curves in Fig. 2.14(b) and (e) instead reveal a rather flat distinctive plateau, indicative of strong caged motion. In comparing motion against the three facets, we see that for the same value of ε_{LS}, the [011] facet induces the strongest degree of caging but surprisingly, the shortest period of confinement. The latter confirms faster escape of particles from the contact layer to the subsequent liquid layer.

2.3.3.4 Non-ergodicity parameter

The dependence of the terminal time t^* and non-ergodicity parameter value F^* as ε_{LS} increases is shown in Fig. 2.15. When combined with the findings in Fig. 2.11, the results in Fig. 2.15(a) highlight that above the value ε_{LS} relating to the structural transition for the [011] case, particles spend the least amount of time undergoing 2D caged motion than similarly parameterized motion for contact layers against the [001] or [111] facet. The caging residence time is much therefore shorter despite that the caging is stronger as quantified by the value F^* in Fig. 2.15(b). Below the structural transition, for the same value ε_{LS},

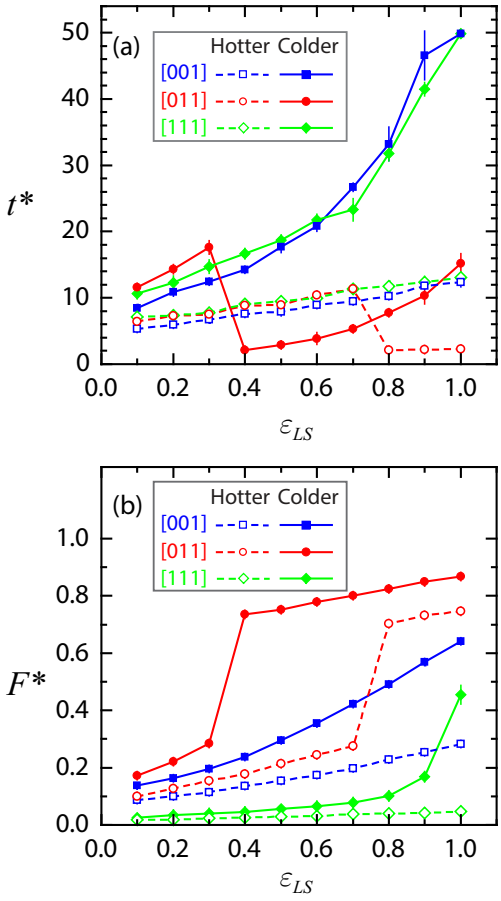

Figure 2.15: SISF analysis. (a) Terminal time t^* and (b) non-ergodicity parameter F^* extracted from SISF curves in Fig. 2.14. Vertical lines through icons represent standard deviation; connecting segments are a guide to the eye.

liquid particles against the [011] facet spend similar or slightly longer times undergoing sub-diffusive or weakly caged motion as particles against the other two facets. However, for similar contact layer temperature and identical value ε_{LS}, the [011] case always incurs the largest value of F^*. As described in Section 1.3.3, data collection was terminated at time t^* once there were fewer than 10 particles that had never left the contact layer. A different criterion for minimum residency will of course yield different values of t^* and F^* but the trends described should still distinguish the [011] facet from the other two.

2.3.4 Crystal surface potential

The discussion so far has centered on the special nature of the contact layer against the [011] facet. Next we try and relate 2D caged motion to the symmetry and structure of the underlying crystal lattice. For instance, the 2D Bravais lattice for the [011] facet has only two-fold symmetry while the [001] facet has four-fold and the [111] facet six-fold symmetry. This reduced symmetry should influence how the kinetic and potential energy of particles

Facet	H/C side	ε_{LS}	Min	Max
[001]	H	0.1	-0.455 (0.001)	3.32 (0.20)
[001]	C	0.1	-0.472 (0.001)	4.36 (0.19)
[001]	H	1.0	-4.435 (0.010)	17.2 (0.63)
[001]	C	1.0	-4.727 (0.004)	41.4 (1.54)
[011]	H	0.1	-0.373 (0.002)	2.88 (0.68)
[011]	C	0.1	-0.382 (0.001)	2.55 (0.06)
[011]	H	1.0	-5.425 (0.021)	3550 (497)
[011]	C	1.0	-5.688 (0.016)	5860 (172)
[111]	H	0.1	-0.367 (0.003)	1.68 (0.09)
[111]	C	0.1	-0.380 (0.002)	1.61 (0.04)
[111]	H	1.0	-4.011 (0.010)	2.56 (0.24)
[111]	C	1.0	-4.127 (0.004)	4.17 (0.16)

Table 2.4: Minimum and maximum values of the crystal surface potential computed from Eq. (2.4). For each parameter set, measurements spanning a total time $t_{\text{total}} = 5\times10^6\Delta t_{int} = 10^4$ were separated into ten equal non-overlapping time blocks. Mean and standard deviation values are based on the average of the ten min/max values.

moving across these terrains partition differently along different Cartesian directions. Here, we examine some details of the L/S potential landscape for the smallest and largest value of ε_{LS}, which when evaluated together with the results in Fig. 2.11 and Fig. 2.14, highlight an additional feature of the [011] facet.

Shown in Fig. 2.16 are images of the crystal surface potential given by

$$U_{\text{surf}}(x, y, z_c) = \left\langle \sum_{i=1}^{N_s} U_{LS}(|\vec{r}_c - \vec{r}_{s,i}|) \right\rangle \tag{2.4}$$

computed at the distance $z = z_c$ corresponding to the position of the peak in the liquid density ρ_c (see Fig. 2.2). Here, $\vec{r}_c = (x, y, z = z_c)$ denotes a coordinate in the contact layer, $\vec{r}_{i,s}$ is the coordinate of particle i in the solid layer and N_s is the number of solid particles within the potential cutoff distance. The images represent a square plaquette with edge length of about three lattice constants centered in the $(\hat{x}, \hat{y}$ plane of the rectangular cell in Fig. 1.2(a). The plaquette was partitioned into a 200×200 array of smaller squares and measurements extracted from the grid center points.

The numerical values indicated in each panel represent the minimum and maximum values of $U_{\text{surf}}(x, y, z_c)$ within the plaquette. (Higher precision values with standard deviations are listed in Table 2.4.) The mean and standard deviation, based on 10^3 snapshots in time, were computed from the averaging scheme outlined in Section 1.3.2). Below we refer to the ratio of the maximum to minimum value as the max/min ratio.

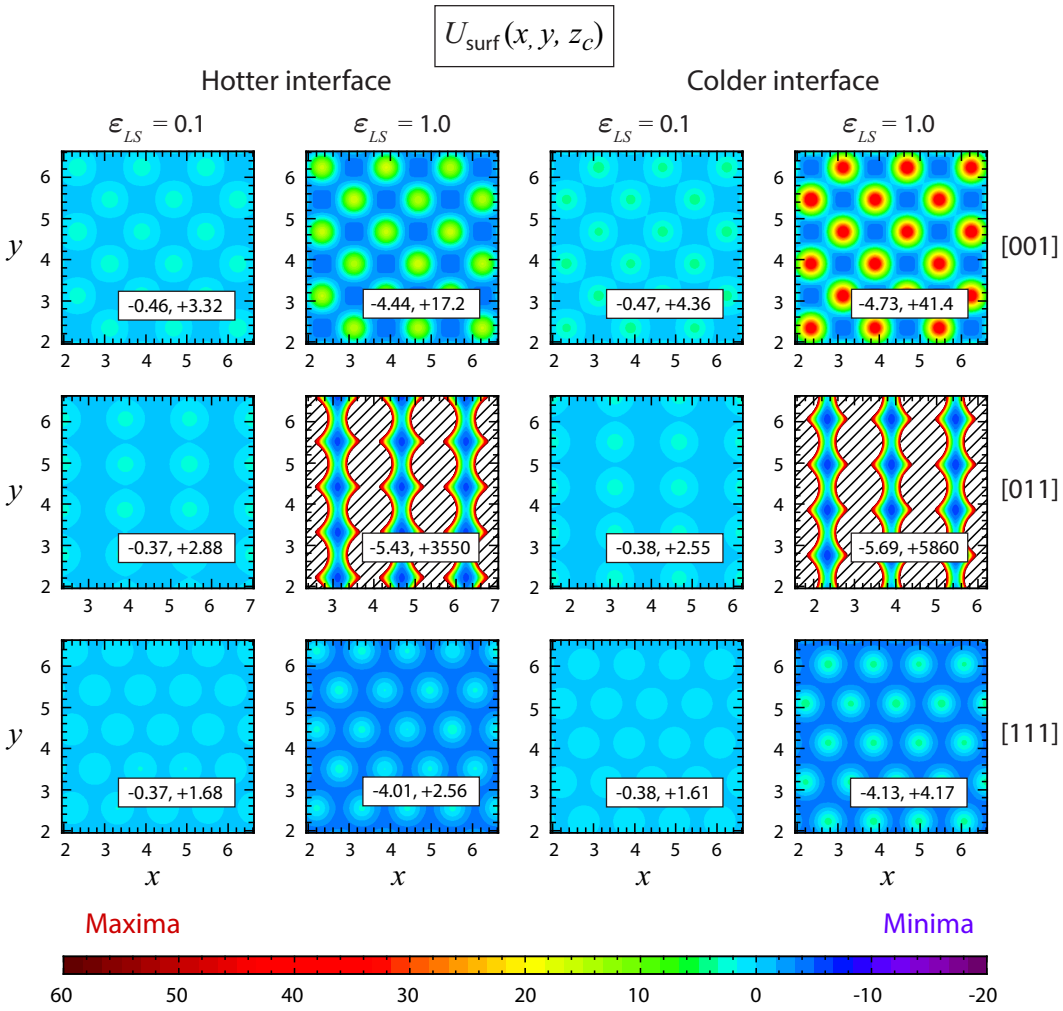

Figure 2.16: Images of the crystal surface potential $U_{\text{surf}}(x, y, z_c)$ given by Eq. (2.4) acting on particles in the hotter and colder contact layer for three facet orientations and $\varepsilon_{LS} = 0.1$ and 1.0. Numerical pairs are the minimum and maximum values of $U_{\text{surf}}(x, y, z_c)$ within the plaquette. Diagonal black lines lines indicate regions where $U_{\text{surf}} > 60$.

For the examples shown in Fig. 2.4, at fixed value ε_{LS}, the minima of $U_{\text{surf}}(x, y, z_c)$ are all relatively insensitive to temperature; the maxima experience small to very large increase at colder temperature depending on ε_{LS} and facet. This behavior may accord with studies [52] indicating that a decrease in temperature for the LJ potential tends to decrease the particle separation distance σ and to increase the potential minimum ε_{LS} such that the repulsive contribution is more strongly influenced.

For $\varepsilon_{LS} = 0.1$, aside from the different symmetry, all the images appear remarkably similar and display only a gentle undulation in the potential landscape, which suggests relatively smaller hindrance to particle motion within the contact layer. This behavior is nonetheless not truly diffusive but sub-diffusive (i.e., $\gamma_E < 1.0$ as shown in Fig. 2.11(g). For $\varepsilon_{LS} = 1.0$, the undulations in $U_{\text{surf}}(x, y, z_c)$ are larger and steepen further at colder temperatures. Here,

the [011] case truly stands out in that its max/min ratio is about two and half orders of magnitude at the hotter L/S interface and more than three orders of magnitude at the colder L/S interface. The [111] case has the smallest max/min ratio, which is why those liquid particles exhibit the highest in-plane mobility in Fig. 2.11. The images of U_{surf} for the [011] facet also reveal that the large repulsive barriers occupy a larger area of the plaquette, which explains why the contact density ρ_c for the [011] case in Fig. 2.2(g) is the smallest of all three facets.

The strong anisotropy evident in the [011] potential surface for $\varepsilon_{LS} = 1.0$ leads to especially strong confinement of particles associated with 2D caged motion. In comparison to the other two cases, the [011] facet induces extremely large and rather wide repulsive barriers along the $\hat{x}$ axis and slightly deeper attractive basins along the $\hat{y}$ axis. Consequently, motion along the $\hat{x}$ axis is almost completely suppressed. Motion of particles along the $\hat{y}$ axis is also hindered since those routes are crowded with other liquid particles centered about the more attractive basins. Thermal fluctuations therefore tend to cause escape of particles from the contact layer more readily along the $\hat{z}$ axis. We suspect that thermal transport along the $\hat{z}$ axis is also more efficient due to the more correlated motion among particles during escape from their 1D alignment in the contact layer.

2.4 Discussion

The early NEMD studies cited in the Introduction as well as more recent continuum [20, 46, 56] and particle-based simulations [2, 10, 17, 21, 22, 49, 50, 53, 59, 65, 66, 92] all confirm that an enhancement in L/S wettability or increase in liquid pressure generally leads to a reduction in the thermal boundary resistance and thermal slip length at a L/S interface. This correspondence has been attributed to the higher resulting contact density from enhanced liquid on solid adsorption/absorption and/or a smaller depletion layer. Intuitively, it seems reasonable that a higher contact density will promote more frequent collisions between liquid and solid particles thereby enhancing the rate at which thermal energy is transferred across the interface. While the results in Fig. 2.4(a) confirm that all things equal, larger values of ε_{LS} lead to smaller thermal slip lengths, the data in Fig. 2.4(b) highlight a contradiction of sorts with this prevailing view. Specifically, for the same value ε_{LS}, the [011] facet supports the highest thermal flux yet maintains the smallest contact density of all three facets tested. From this demonstration alone, it is clear that a single variable like ρ_c cannot reliably nor uniquely predict the relative magnitude in thermal slip length. This counterexample motivated the current study in which various metrics relating to the structural and dynamic properties of particle motion in the contact layer are used to piece together a more accurate picture of how thermal energy is best transferred across the interfacial region. By confining the liquid layer between two solids, each oriented identically along one of three facets of an FCC crystal, it becomes clearer how the different facet symmetry, width and depth of the periodic crystal surface potential and local temperature influences the configuration and

motion of particles in the contact layer. The two L/S interfaces, one at the hotter and colder side of the liquid layer, act essentially as phonon filters which regulate the maximum rate of heat transfer across the entire system. Quantification of particle trajectories by mean square displacement and the self-intermediate scattering function reveals that a smaller thermal slip length is strongly correlated with more rapid particle escape from 2D caged motion in the contact layer. And the stronger the caging effect, the smaller the thermal slip length. As has been noted for supercooled liquids and so-called structural glasses [40], it is highly likely that in our system too, as a particle escapes one cage and gets trapped by a next, it does not do so alone since its displacement causes coherent motion of neighboring particles as well. The type of 2D caged motion described in this work likely pertains more broadly to the coherent motion of clusters of neighboring particles and therefore sub-diffusive behavior characterized by a much larger effective mass. Besides the retarding influence of the periodic crystal surface potential, this effect too may help explain the reduction in the exponent values γ_L in Table 2.7.

We end this discussion with an explanation for why our findings stand in sharp contrast to the main conclusion of a previous study which remains highly cited to this day [89]. The authors of that work reported no discernible effect on thermal transfer across the L/S interface which could be traced to the degree of in-plane liquid ordering for a net thermal gradient in the direction parallel or perpendicular to the contact layer. This conclusion was based on the observation that the thermal distribution, thermal gradient and thermal conductivity of the liquid layer remained unchanged despite varying the liquid layer thickness and increasing ε_{LS} from 0.2 to 3.3. Closer inspection of the data in that study suggests three important factors that were overlooked. First, the value $\varepsilon_{LS} = 3.3$ selected to represent a strongly wetting liquid was so large as to induce epitaxial locking of the contact layer to the solid surface for all cases tested. This problem is evident in Fig. 3 of Ref. [89] showing perfect registry between the particles in the contact layer and the pattern set by the periodic surface potential describing the [100] facet of an FCC crystal. This behavior would not only significantly repress 2D diffusive motion within the contact layer by would also create a solid-like interstitial layer. Secondly, the density and temperature of the liquid layer were chosen to be too close to the triple point [27] thereby also incurring formation of solid-like domains within the contact layer. Thirdly, the thickness of the solid layers abutting the liquid layer were reported to be 10× the edge length of the FCC unit cell. The thickness of the solid layers was therefore less than the phonon mean free path [21, 37, 68], which would restrict the set of vibrational frequencies able to couple to the liquid layer.

Table 2.5: Results of NEMD simulations described in the text for $T_{\text{source}} = 1.6$ and $T_{\text{sink}} = 1.0$ showing the influence of FCC facet orientation and L/S interaction energy ε_{LS} on the thermal flux J_z [Eq. (1.8)] and magnitude of the thermal gradient $|dT/dz|$ and thermal conductivity k [Eq. (1.3)] within the bulk solid and liquid layers away from the L/S interface. The numerical values in each column are to be multiplied by the multiplicative factor appearing in the column heading. Thermal gradient values were extracted from least squares fits across the linear portion of the thermal profile within each layer. Numbers in parentheses are standard deviation values. All values are reported in reduced units.

			Liquid layer		Hotter solid layer		Colder solid layer	
Facet	ε_{LS}	$J_z \times 10^{-2}$	$\lvert dT/dz\rvert \times 10^{-2}$	k	$\lvert dT/dz\rvert \times 10^{-2}$	$k \times 10^{3}$	$\lvert dT/dz\rvert \times 10^{-2}$	$k \times 10^{3}$
[001]	0.1	6.88(0.05)	0.90(0.03)	7.63(0.26)	0.03(0.02)	0.24(0.09)	0.03(0.01)	0.32(0.20)
[001]	0.2	7.32(0.05)	0.98(0.03)	7.46(0.23)	0.04(0.02)	0.42(0.60)	0.03(0.01)	0.21(0.05)
[001]	0.3	7.93(0.11)	1.04(0.03)	7.63(0.31)	0.04(0.02)	0.24(0.24)	0.03(0.02)	0.35(0.19)
[001]	0.4	8.25(0.02)	1.10(0.03)	7.49(0.20)	0.05(0.02)	0.19(0.09)	0.04(0.01)	0.26(0.16)
[001]	0.5	8.63(0.03)	1.16(0.02)	7.45(0.11)	0.05(0.02)	0.30(0.30)	0.04(0.01)	0.24(0.11)
[001]	0.6	8.79(0.07)	1.19(0.03)	7.37(0.18)	0.05(0.01)	0.19(0.05)	0.04(0.01)	0.25(0.07)
[001]	0.7	9.33(0.03)	1.23(0.02)	7.57(0.09)	0.07(0.02)	0.14(0.04)	0.04(0.01)	0.24(0.06)
[001]	0.8	9.48(0.04)	1.29(0.02)	7.32(0.12)	0.05(0.02)	0.22(0.12)	0.03(0.01)	0.45(0.55)
[001]	0.9	9.70(0.04)	1.32(0.03)	7.38(0.15)	0.06(0.02)	0.18(0.06)	0.04(0.01)	0.28(0.10)
[001]	1.0	9.81(0.02)	1.35(0.03)	7.26(0.14)	0.05(0.02)	0.21(0.08)	0.04(0.01)	0.26(0.07)
[011]	0.1	7.71(0.03)	1.04(0.02)	7.39(0.13)	0.04(0.02)	0.53(1.03)	0.03(0.01)	0.25(0.06)
[011]	0.2	8.29(0.04)	1.10(0.02)	7.54(0.11)	0.05(0.02)	0.19(0.07)	0.03(0.01)	0.33(0.15)
[011]	0.3	8.92(0.06)	1.17(0.03)	7.64(0.14)	0.05(0.01)	0.18(0.04)	0.03(0.01)	0.40(0.24)
[011]	0.4	9.13(0.11)	1.22(0.01)	7.47(0.13)	0.06(0.02)	0.19(0.06)	0.04(0.01)	0.24(0.06)
[011]	0.5	9.51(0.04)	1.28(0.02)	7.43(0.17)	0.06(0.02)	0.17(0.05)	0.03(0.01)	0.35(0.16)
[011]	0.6	10.01(0.08)	1.32(0.02)	7.62(0.08)	0.06(0.01)	0.19(0.06)	0.04(0.01)	0.27(0.08)
[011]	0.7	10.07(0.08)	1.38(0.02)	7.26(0.14)	0.05(0.01)	0.22(0.06)	0.03(0.01)	0.39(0.25)
[011]	0.8	10.28(0.04)	1.41(0.04)	7.32(0.18)	0.05(0.02)	0.27(0.19)	0.03(0.01)	0.39(0.21)
[011]	0.9	10.63(0.03)	1.43(0.03)	7.40(0.13)	0.06(0.01)	0.20(0.04)	0.04(0.01)	0.30(0.11)
[011]	1.0	10.73(0.05)	1.46(0.02)	7.36(0.11)	0.05(0.02)	0.21(0.08)	0.04(0.01)	0.32(0.09)
[111]	0.1	7.05(0.04)	0.91(0.03)	7.72(0.28)	0.04(0.01)	0.20(0.09)	0.03(0.01)	0.23(0.09)
[111]	0.2	7.47(0.06)	0.99(0.03)	7.47(0.13)	0.04(0.02)	0.27(0.26)	0.03(0.01)	0.27(0.15)
[111]	0.3	8.14(0.02)	1.06(0.03)	7.68(0.20)	0.04(0.02)	0.24(0.12)	0.03(0.01)	0.34(0.16)
[111]	0.4	8.53(0.05)	1.13(0.01)	7.53(0.07)	0.04(0.01)	0.23(0.11)	0.03(0.01)	0.27(0.11)
[111]	0.5	8.88(0.03)	1.18(0.02)	7.56(0.13)	0.05(0.02)	0.19(0.10)	0.03(0.01)	0.26(0.07)
[111]	0.6	9.32(0.06)	1.23(0.03)	7.57(0.20)	0.06(0.01)	0.16(0.02)	0.03(0.02)	0.91(1.40)
[111]	0.7	9.64(0.07)	1.28(0.02)	7.55(0.13)	0.05(0.01)	0.19(0.05)	0.03(0.01)	0.28(0.08)
[111]	0.8	10.04(0.06)	1.33(0.02)	7.53(0.10)	0.05(0.02)	0.21(0.06)	0.04(0.01)	0.37(0.25)
[111]	0.9	10.22(0.03)	1.36(0.02)	7.49(0.10)	0.06(0.01)	0.20(0.05)	0.04(0.02)	0.29(0.12)
[111]	1.0	10.41(0.04)	1.40(0.02)	7.43(0.10)	0.05(0.03)	0.23(0.15)	0.04(0.01)	0.35(0.20)

Table 2.6: Results of NEMD simulations described in the text for $T_{\text{source}} = 1.6$ and $T_{\text{sink}} = 1.0$ showing the influence of FCC facet orientation and L/S interaction energy ε_{LS} on contact layer density ρ_c, maximum value of the static in-plane structure factor S_{max} [Eq. (1.10)], contact layer temperature T_c [Eq. (1.7)], thermal jump ΔT and thermal slip length L_T [Eq. (1.2)]. Numbers in parentheses are standard deviation values. All values are reported in reduced units.

		Hotter contact layer					Colder contact layer				
Facet	ε_{LS}	ρ_c	S_{max}	T_c	ΔT	L_T	ρ_c	S_{max}	T_c	ΔT	L_T
[001]	0.1	1.351(0.013)	0.083(0.001)	1.451(0.008)	0.139(0.011)	15.457(1.616)	1.567(0.017)	0.124(0.003)	1.168(0.007)	0.155(0.009)	17.172(1.316)
[001]	0.2	1.455(0.029)	0.094(0.001)	1.461(0.007)	0.127(0.010)	12.942(1.279)	1.705(0.037)	0.148(0.002)	1.156(0.004)	0.140(0.006)	14.230(0.730)
[001]	0.3	1.535(0.036)	0.110(0.003)	1.471(0.009)	0.117(0.007)	11.231(0.967)	1.870(0.036)	0.181(0.002)	1.147(0.005)	0.129(0.006)	12.421(0.826)
[001]	0.4	1.629(0.010)	0.125(0.002)	1.475(0.005)	0.110(0.007)	9.975(0.833)	2.007(0.043)	0.222(0.003)	1.137(0.006)	0.116(0.007)	10.519(0.755)
[001]	0.5	1.699(0.024)	0.146(0.002)	1.486(0.006)	0.101(0.005)	8.748(0.568)	2.137(0.019)	0.272(0.004)	1.128(0.005)	0.104(0.003)	8.985(0.311)
[001]	0.6	1.790(0.021)	0.166(0.003)	1.491(0.004)	0.096(0.007)	8.077(0.740)	2.315(0.025)	0.335(0.004)	1.122(0.003)	0.101(0.004)	8.465(0.458)
[001]	0.7	1.869(0.029)	0.189(0.002)	1.492(0.005)	0.091(0.009)	7.461(0.829)	2.521(0.036)	0.403(0.004)	1.110(0.004)	0.089(0.005)	7.281(0.461)
[001]	0.8	1.957(0.030)	0.213(0.001)	1.501(0.004)	0.082(0.005)	6.316(0.488)	2.737(0.033)	0.486(0.004)	1.101(0.003)	0.080(0.005)	6.164(0.473)
[001]	0.9	2.042(0.021)	0.242(0.003)	1.506(0.009)	0.078(0.006)	5.955(0.560)	2.993(0.027)	0.567(0.005)	1.096(0.004)	0.074(0.003)	5.659(0.302)
[001]	1.0	2.126(0.034)	0.274(0.003)	1.513(0.004)	0.073(0.007)	5.362(0.580)	3.269(0.030)	0.645(0.006)	1.089(0.004)	0.069(0.006)	5.101(0.559)
[011]	0.1	0.963(0.021)	0.038(0.001)	1.470(0.006)	0.116(0.006)	11.175(0.607)	0.995(0.023)	0.036(0.001)	1.154(0.004)	0.135(0.007)	12.986(0.790)
[011]	0.2	0.980(0.016)	0.040(0.001)	1.475(0.008)	0.111(0.007)	10.157(0.757)	0.983(0.016)	0.037(0.000)	1.142(0.005)	0.124(0.005)	11.326(0.533)
[011]	0.3	0.970(0.018)	0.043(0.001)	1.484(0.007)	0.101(0.009)	8.697(0.950)	0.941(0.016)	0.040(0.001)	1.131(0.003)	0.113(0.004)	9.685(0.436)
[011]	0.4	0.961(0.017)	0.045(0.001)	1.493(0.003)	0.095(0.004)	7.810(0.354)	1.212(0.031)	0.552(0.002)	1.116(0.004)	0.096(0.003)	7.890(0.249)
[011]	0.5	0.945(0.022)	0.051(0.000)	1.498(0.006)	0.087(0.007)	6.817(0.627)	1.375(0.027)	0.588(0.004)	1.107(0.004)	0.086(0.006)	6.767(0.549)
[011]	0.6	1.006(0.013)	0.055(0.001)	1.506(0.005)	0.077(0.007)	5.860(0.579)	1.549(0.036)	0.651(0.003)	1.099(0.003)	0.082(0.004)	6.251(0.282)
[011]	0.7	1.077(0.027)	0.056(0.001)	1.514(0.004)	0.070(0.006)	5.057(0.493)	1.797(0.023)	0.713(0.003)	1.091(0.003)	0.070(0.004)	5.074(0.376)
[011]	0.8	1.164(0.025)	0.487(0.004)	1.521(0.008)	0.068(0.007)	4.824(0.594)	2.009(0.034)	0.768(0.003)	1.086(0.004)	0.065(0.006)	4.658(0.485)
[011]	0.9	1.253(0.015)	0.554(0.003)	1.526(0.005)	0.064(0.006)	4.485(0.489)	2.237(0.020)	0.814(0.003)	1.079(0.004)	0.058(0.004)	4.047(0.338)
[011]	1.0	1.329(0.013)	0.588(0.004)	1.529(0.006)	0.063(0.005)	4.285(0.378)	2.455(0.038)	0.851(0.003)	1.074(0.004)	0.051(0.005)	3.510(0.359)
[111]	0.1	1.525(0.017)	0.032(0.001)	1.445(0.007)	0.139(0.010)	15.208(1.579)	1.776(0.014)	0.042(0.001)	1.181(0.005)	0.164(0.005)	17.958(0.898)
[111]	0.2	1.664(0.022)	0.035(0.001)	1.452(0.009)	0.134(0.009)	13.498(1.314)	1.988(0.033)	0.048(0.001)	1.165(0.004)	0.145(0.006)	14.661(0.840)
[111]	0.3	1.781(0.026)	0.039(0.001)	1.459(0.008)	0.123(0.007)	11.660(0.878)	2.154(0.024)	0.055(0.002)	1.154(0.004)	0.134(0.006)	12.696(0.742)
[111]	0.4	1.876(0.026)	0.041(0.001)	1.470(0.008)	0.114(0.006)	10.089(0.661)	2.319(0.028)	0.065(0.002)	1.145(0.002)	0.121(0.004)	10.674(0.341)
[111]	0.5	1.989(0.022)	0.045(0.001)	1.475(0.006)	0.109(0.006)	9.260(0.657)	2.505(0.033)	0.076(0.002)	1.132(0.004)	0.110(0.004)	9.317(0.396)
[111]	0.6	2.091(0.027)	0.050(0.001)	1.486(0.006)	0.097(0.008)	7.921(0.745)	2.705(0.028)	0.093(0.002)	1.126(0.007)	0.105(0.005)	8.562(0.505)
[111]	0.7	2.165(0.020)	0.054(0.002)	1.488(0.005)	0.093(0.005)	7.255(0.455)	2.927(0.028)	0.117(0.005)	1.116(0.004)	0.094(0.004)	7.380(0.415)
[111]	0.8	2.260(0.029)	0.059(0.001)	1.498(0.006)	0.086(0.005)	6.418(0.404)	3.171(0.040)	0.159(0.005)	1.110(0.004)	0.086(0.005)	6.455(0.469)
[111]	0.9	2.403(0.018)	0.063(0.001)	1.496(0.005)	0.082(0.003)	6.051(0.315)	3.439(0.035)	0.290(0.033)	1.100(0.004)	0.078(0.004)	5.763(0.374)
[111]	1.0	2.490(0.028)	0.070(0.001)	1.503(0.007)	0.078(0.006)	5.534(0.447)	3.812(0.039)	0.582(0.018)	1.095(0.004)	0.071(0.006)	5.093(0.461)

Table 2.7: Results of NEMD simulations described in the text for $T_{\text{source}} = 1.6$ and $T_{\text{sink}} = 1.0$ showing the influence of FCC facet orientation and L/S interaction energy ε_{LS} on the early (E) time and late (L) time exponent values, γ_E and γ_L, respectively, obtained from least square fits to the 2D mean square displacement curves in Fig. 2.11(numbers in parentheses are 95% confidence interval values). Also listed are the extracted values of the non-ergodicity parameter $F_c^*(\vec{k}_o)$ [Eq. (1.13)] at the terminal time τ^* (numbers in parentheses are standard deviation values). All values are reported in reduced units.

		Hotter contact layer				Colder contact layer			
Facet	ε_{LS}	γ_E	γ_L	F^*	t^*	γ_E	γ_L	F^*	t^*
[001]	0.1	1.8969(0.0733)	0.9745(0.0010)	0.0861(0.0047)	5.3100(0.3100)	1.8932(0.0758)	0.8897(0.0022)	0.1375(0.0004)	8.4500(0.5400)
[001]	0.2	1.9017(0.0689)	0.9626(0.0012)	0.0991(0.0029)	5.9400(0.2946)	1.8984(0.0694)	0.9022(0.0018)	0.1631(0.0033)	10.8467(0.5900)
[001]	0.3	1.8952(0.0722)	0.9434(0.0020)	0.1146(0.0006)	6.7100(0.5220)	1.8958(0.0744)	0.9082(0.0018)	0.1953(0.0043)	12.4067(0.3921)
[001]	0.4	1.8899(0.0772)	0.9340(0.0014)	0.1364(0.0004)	7.5800(0.1970)	1.8867(0.0777)	0.8700(0.0024)	0.2379(0.0064)	14.2200(0.1058)
[001]	0.5	1.8990(0.0722)	0.9150(0.0022)	0.1549(0.0010)	7.8700(0.5910)	1.8846(0.0816)	0.9173(0.0020)	0.2959(0.0072)	17.7067(0.8429)
[001]	0.6	1.8912(0.0747)	0.9260(0.0020)	0.1732(0.0025)	8.9600(0.2553)	1.8731(0.0875)	0.8442(0.0020)	0.3542(0.0016)	20.8067(0.7814)
[001]	0.7	1.8801(0.0813)	0.9095(0.0022)	0.1969(0.0044)	9.4800(0.1970)	1.8646(0.0958)	0.8322(0.0024)	0.4213(0.0059)	26.6933(0.6395)
[001]	0.8	1.8700(0.0872)	0.8977(0.0020)	0.2277(0.0026)	10.2800(0.4854)	1.8674(0.0972)	0.8568(0.0020)	0.4901(0.0059)	33.2133(2.5694)
[001]	0.9	1.8727(0.0886)	0.8966(0.0020)	0.2540(0.0018)	11.8200(0.4652)	1.8607(0.1000)	0.8386(0.0020)	0.5681(0.0117)	46.5600(3.6550)
[001]	1.0	1.8715(0.0888)	0.8865(0.0022)	0.2832(0.0063)	12.3267(0.6906)	1.8458(0.1077)	0.7743(0.0025)	0.6410(0.0038)	49.8400(0.0000)
[011]	0.1	1.9025(0.0672)	0.8894(0.0006)	0.0994(0.0036)	6.4300(0.4050)	1.8962(0.0739)	0.8394(0.0016)	0.1713(0.0031)	11.5933(0.5201)
[011]	0.2	1.8963(0.0727)	0.8509(0.0006)	0.1274(0.0016)	7.3133(0.5637)	1.8889(0.0783)	0.7756(0.0016)	0.2216(0.0046)	14.3000(0.7158)
[011]	0.3	1.8894(0.0764)	0.8413(0.0010)	0.1537(0.0019)	7.5133(0.3743)	1.8854(0.0772)	0.7304(0.0014)	0.2846(0.0022)	17.5800(1.0153)
[011]	0.4	1.8826(0.0805)	0.8192(0.0016)	0.1780(0.0034)	8.8333(0.5201)	1.8935(0.0758)	0.2980(0.0062)	0.7358(0.0029)	2.0867(0.1332)
[011]	0.5	1.8870(0.0775)	0.7858(0.0020)	0.2139(0.0060)	8.9067(0.6438)	1.8760(0.0888)	0.2826(0.0030)	0.7520(0.0016)	2.9000(0.5724)
[011]	0.6	1.8810(0.0811)	0.7585(0.0022)	0.2439(0.0051)	10.3733(0.4086)	1.8682(0.0947)	0.2203(0.0032)	0.7783(0.0025)	3.8400(0.9007)
[011]	0.7	1.8760(0.0872)	0.7375(0.0028)	0.2751(0.0043)	11.3133(0.4801)	1.8592(0.1011)	0.2544(0.0028)	0.8010(0.0016)	5.3000(0.1217)
[011]	0.8	1.8769(0.0866)	0.3829(0.0080)	0.7021(0.0022)	2.1067(0.1137)	1.8748(0.0869)	0.1889(0.0006)	0.8242(0.0018)	7.7867(0.3252)
[011]	0.9	1.8654(0.0925)	0.3438(0.0062)	0.7318(0.0023)	2.1933(0.1943)	1.8275(0.1202)	0.1494(0.0014)	0.8488(0.0014)	10.2933(1.1856)
[011]	1.0	1.8536(0.1038)	0.3101(0.0048)	0.7459(0.0030)	2.2500(0.1700)	1.8276(0.1233)	0.0978(0.0016)	0.8679(0.0009)	15.2000(1.4500)
[111]	0.1	1.8930(0.0750)	1.0431(0.0008)	0.0184(0.0039)	7.1500(0.2420)	1.8881(0.0777)	1.0005(0.0004)	0.0249(0.0008)	10.6000(0.4550)
[111]	0.2	1.8953(0.0722)	1.0307(0.0008)	0.0186(0.0024)	7.3667(0.3139)	1.8980(0.0730)	0.9841(0.0004)	0.0347(0.0061)	12.2533(1.0191)
[111]	0.3	1.8960(0.0727)	1.0266(0.0008)	0.0233(0.0006)	7.7900(0.6510)	1.8821(0.0819)	0.9836(0.0006)	0.0391(0.0017)	14.7333(1.0108)
[111]	0.4	1.8923(0.0736)	1.0206(0.0008)	0.0248(0.0006)	9.0500(0.0611)	1.8784(0.0861)	0.9783(0.0008)	0.0449(0.0033)	16.6333(0.1677)
[111]	0.5	1.8870(0.0761)	1.0182(0.0010)	0.0288(0.0010)	9.5100(0.4130)	1.8834(0.0819)	0.9726(0.0006)	0.0555(0.0012)	18.7067(0.5601)
[111]	0.6	1.8876(0.0755)	1.0048(0.0010)	0.0310(0.0012)	9.9667(0.5132)	1.8711(0.0883)	0.9492(0.0008)	0.0648(0.0023)	21.7600(0.8681)
[111]	0.7	1.8806(0.0833)	1.0064(0.0004)	0.0384(0.0018)	11.3667(0.4272)	1.8641(0.0941)	0.9370(0.0010)	0.0783(0.0119)	23.3200(1.6837)
[111]	0.8	1.8619(0.0938)	0.9932(0.0006)	0.0399(0.0040)	11.7467(0.7829)	1.8603(0.1000)	0.9343(0.0010)	0.1011(0.0082)	31.7733(1.0801)
[111]	0.9	1.8551(0.0988)	0.9949(0.0006)	0.0411(0.0044)	12.4000(0.8492)	1.8587(0.1025)	0.9128(0.0008)	0.1689(0.0098)	41.4600(1.0054)
[111]	1.0	1.8712(0.0838)	0.9824(0.0006)	0.0473(0.0035)	13.0600(0.6879)	1.8609(0.1102)	0.8528(0.0014)	0.4551(0.0323)	49.8600(0.0000)

Chapter 3

VIBRATIONAL ANALYSIS OF THERMAL TRANSPORT ACROSS L/S INTERFACE

3.1 Overview of this chapter

In this chapter, we first examine the vibrational modes that contribute to energy exchange between the liquid and solid particles by computing the spectral heat flux [Eq. (1.17)] decomposed into the in-plane (i.e., along the x- and y-axes) and out-of-plane (i.e., along the z-axis) components. We then analyze heterogeneous dynamics in the contact layer using NGP [Eq. (1.14)] to extract characteristic times for the short-time ballistic motion and subsequent caging motion. The frequencies corresponding to these characteristic times are used to analyze the frequency range where the normal modes in the contact layer are most abundant. Then, we analyze the DOS of the first liquid and contact layers to quantify a degree of overlap between the distributions and study its impact on TBR. Finally, we propose a master curve relation for TBR in terms of contact layer temperature and L/S frequencies.

3.2 Simulation parameters

The simulation parameters employed in Chapter 3 are identical to those employed in Chapter 2. Refer to Section 2.2 and Table 2.1 for details.

3.3 Results

3.3.1 Spectral heat flux across L/S interface

As proposed in the original model by Frenkel [14], the relaxation dynamics in the in-plane directions has significant impacts on the transverse (in-plane) vibrational modes supported by the liquid. In the past, Caplan et al. [10] proposed an analytical model based on the diffuse mismatch model [69] in the attempt to quantify the wettability dependence of thermal transport across the L/S interface, and reported a substantial contribution arising from the transverse vibrational modes. Later, Sääskilahti et al. [62] conducted a mode-level decomposition of heat flux across the L/S interface using NEMD simulations, and found that stronger surface wettability (i.e., larger ε_{LS}) leads to enhanced vibrational coupling in the transverse directions.

To generalize these findings in the context of the in-plane liquid ordering, we compute the total and in-plane components of the frequency-dependent heat flux [Eq. (1.18) and Eq. (1.21)] across different FCC facets at $\varepsilon_{LS} = 0.1$ and 1.0, and summarize them in Fig. 3.1. In all cases examined, the dominant contribution to the interfacial thermal transport is arising from the frequency range $0 < \nu < 14$ which qualitatively agrees with the frequency analysis conducted by Sääskilahti et al. [62]. At greater values of ε_{LS}, $q_{L\to S}(\nu)$ not only increases at

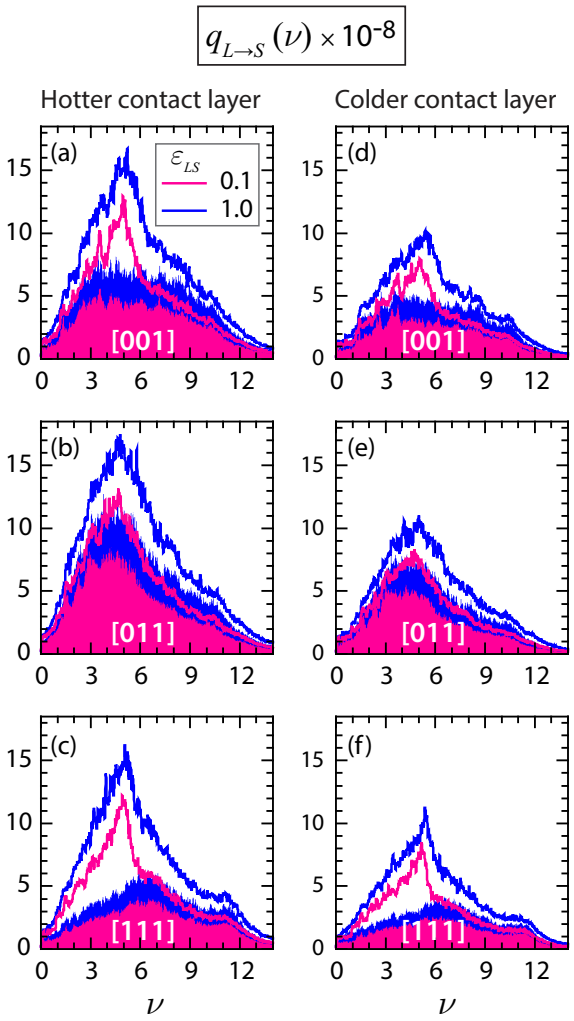

Figure 3.1: spectral heat flux [Eq. (1.18) and Eq. (1.21)] across L/S interface for three FCC facets at $\varepsilon_{LS} = 0.1$ and 1.0. Shaded regions in pink and light blue designate in-plane contribution for $\varepsilon_{LS} = 0.1$ and 1.0, respectively.

all frequencies, but also the major peaks found around $4 \leq \nu \leq 6$ shift rightward. Similarly, higher temperature also leads to enhanced heat flux over the entire frequency range, but the peak positions remain nearly unchanged. As suggested by earlier works, the in-plane contributions ($q^x_{L\to S}(\nu) + q^y_{L\to S}(\nu)$) occupy a non-negligible fraction of the total heat flux in all cases considered, especially over high frequencies ($\nu \gtrapprox 9$) where the total $q_{L\to S}(\nu)$ is entirely dominated by the in-plane components. For the [001] and [111] interfaces, large gaps between the total and in-plane contributions near $4 \leq \nu \leq 6$ imply considerable thermal contributions along the out-of-plane direction. In contrast, the in-plane heat flux across the [011] interface occupies a significant fraction of the total $q_{L\to S}(\nu)$ at all frequencies. To further quantify thermal contributions across different solid facets, we integrate Eq. (1.21) over frequency to evaluate the cumulative flux $Q_{L\to S}(\nu)$ and its directional decomposition

$Q^{\alpha}_{L\to S}(\nu)$ along different Cartesian coordinates ($\alpha \in x, y, z$):

$$Q_{L\to S}(\nu) = \int_0^{\nu} q_{L\to S}(\nu')d\nu', \tag{3.1}$$

$$Q^{\alpha}_{L\to S}(\nu) = \int_0^{\nu} q^{\alpha}_{L\to S}(\nu')d\nu'. \tag{3.2}$$

The in-plane and out-of-plane contributions are simply given by $Q^{x}_{L\to S}(\nu) + Q^{y}_{L\to S}(\nu)$ and $Q^{z}_{L\to S}(\nu)$, respectively. In Fig. 3.2, we plot $Q_{L\to S}(\nu)$ for three FCC facets at both sides of the computational cell (Here, we only consider $\varepsilon_{LS} = 1.0$). In all cases shown, $Q_{L\to S}(\nu)$ rises sharply over the intermediate frequencies ($4 \leq \nu \leq 9$), then eventually asymptotes to $Q_{L\to S}(\infty)$ which includes thermal contributions at all frequencies. For both colder and hotter interfaces, the total $Q_{L\to S}(\nu)$, as well as its in-plane components, are greatest across the [011] facet. The out-of-plane components are slightly larger across the [111] facet compared to the other two, likely because of enhanced contact density at the [111] interface. However, the differences among the out-of-plane components are insubstantial compared to their in-plane counterparts.

3.3.2 Non-Gaussian parameter and characteristic times

Heterogeneous dynamics that governs structural relaxation of the contact layer was quantified using the 2D NGP defined in Eq. (1.14). The results are shown in Fig. 3.3 at the hotter and colder interfaces for three facet orientations and $0.1 \leq \varepsilon_{LS} \leq 1.0$. In all cases presented in Fig. 3.3, non-zero values were obtained over the time interval spanning roughly three decades ($10^{-1} < t < 10^{2}$). The deviation of Eq. (1.14) from zero is attributed to the caging effect induced by the periodically corrugated crystal surface potential which restricts the planar diffusion within the contact layer. For each curve in Fig. 3.3, we extracted the characteristic times t_{BL} and t_{cage} which represent the average time duration of the ballistic and caging motions, respectively. The former (t_{BL}) was estimated by the time at which $\alpha_2(t)$ first deviates from zero, and the latter (t_{cage}) was taken to be the time at which the deviation from zero was greatest. Two types of characteristic times obtained at the hotter and colder L/S interfaces for $\varepsilon_{LS} = 0.1, 1.0$ are listed in Table 3.3.2. For the ballistic motion, we found that $t_{BL} \sim 0.1$ for all interfaces examined. It is readily seen that t_{BL} is insensitive to the variations in temperature, L/S interaction energy, and crystal facet orientation. Hence, t_{BL} should be interpreted as the smallest time scale below which no crucial dynamics takes place rather than a key time scale that directly impacts thermal transport across the L/S interface. In contrary, t_{cage} exhibits strong dependence on the properties of the L/S interface, increasing substantially upon lowering the temperature or enhancing the L/S interaction energy (ε_{LS}). Comparing t_{cage} across three crystal facets, we note that liquid particles in the contact layer against the [011] facet experience the longest caging motion out of the three. This finding is

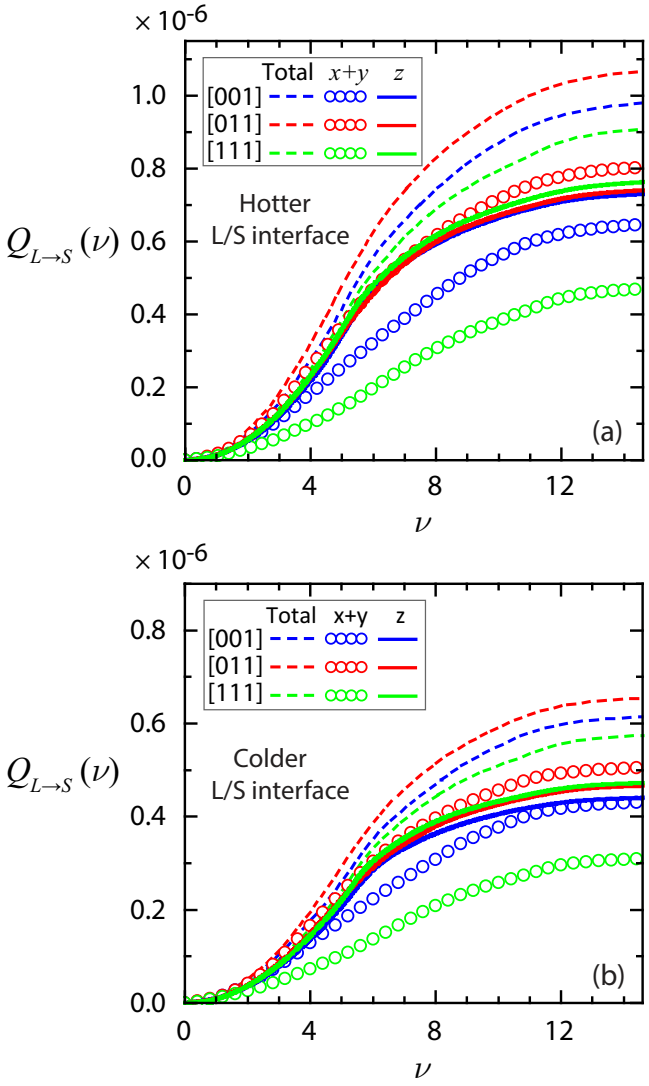

Figure 3.2: Cumulative heat flux [Eq. (3.1) and Eq. (3.2)] across three FCC facets at (a) hotter T_H interface and (b) colder T_C interface ($\varepsilon_{LS} = 1.0$).

consistent with the results from the earlier analysis of MSD and SISF (2.3.3) which indicated that caging behaviors are most pronounced across the [011] facet.

The corresponding frequencies, $\nu_{BL} = 1/t_{BL}$ and $\nu_{cage} = 1/t_{cage}$, were used to estimate the frequency range where the vibrational modes in the contact layer are mostly found. The results in Fig. 3.4(a) indicate that $\nu_{BL} \gtrsim 10$ for the [001] and [111] facets irrespective of the L/S interaction energy or temperature. For the [011] facet, the structural transition that was noted earlier (Section 2.3.2) at $0.3 \lesssim \varepsilon_{LS} \lesssim 0.4$ across the colder interface leads to a notable reduction in ν_{BL}, and likewise across the hotter interface at $0.7 \lesssim \varepsilon_{LS} \lesssim 0.8$. The structural transition, therefore, lowers the upper bound of the frequency range occupied by vibrational modes in the contact layer.

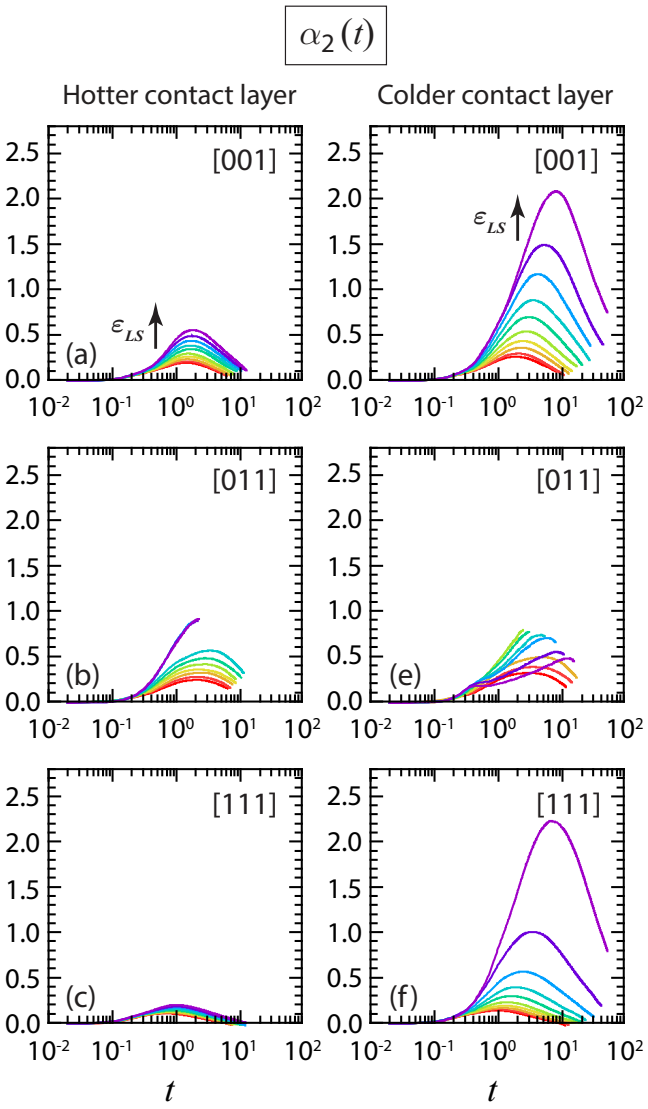

Figure 3.3: NGP [Eq. (1.14)] for the contact liquid layers across three FCC facets at (a-c) the hotter and (d-f) colder interfaces. A linear color scale is used to designate $0.1 \leq \varepsilon_{LS} \leq 1.0$ in increments of 0.1 as indicated by the short arrow pointing in the direction of increasing ε_{LS}.

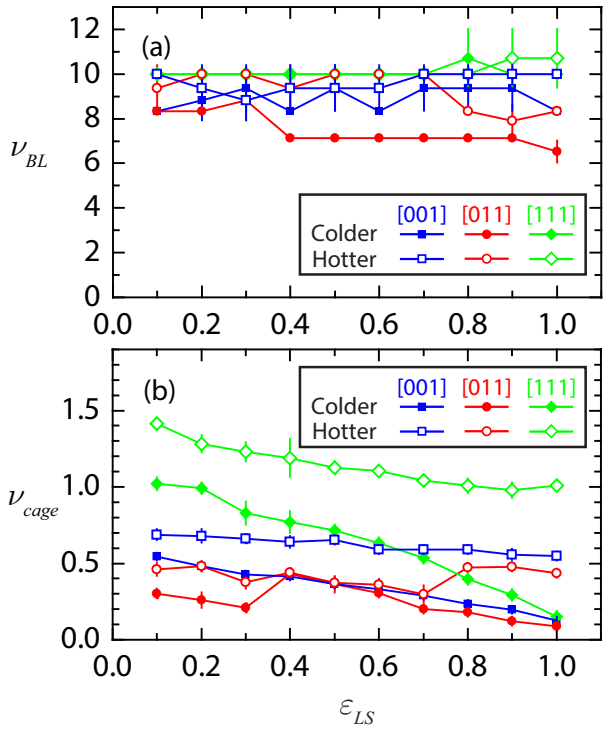

Figure 3.4: Characteristic frequencies (a) $\nu_{BL} = 1/t_{BL}$ for ballistic motion and (b) $\nu_{cage} = 1/t_{cage}$ for caging motion estimated using NGP [Eq. (1.14)] across different crystal facets. Connecting segments are only a guide to the eye.

Fig. 3.4(b) shows ν_{cage} at the hotter and colder interfaces for three facet orientations. The dependence on ε_{LS} is weak at the hotter interface, but becomes more notable at the colder interface. For both the hotter and colder interfaces, ν_{cage} tends to be lowest across the [011] facet irrespective of the L/S interaction energy, especially when ε_{LS} is small. A smaller value of ν_{cage} implies that caging motion makes greater contribution to vibrational modes in the contact layer.

		Hotter interface		Colder interface	
Facet	ε_{LS}	t_{BL}	t_{cage}	t_{BL}	t_{cage}
[001]	0.1	0.10(0.00)	1.45(0.08)	0.12(0.00)	1.84(0.05)
[001]	1.0	0.10(0.00)	1.83(0.04)	0.12(0.00)	7.86(0.26)
[011]	0.1	0.11(0.01)	2.17(0.20)	0.12(0.00)	3.31(0.35)
[011]	1.0	0.12(0.00)	2.29(0.09)	0.15(0.01)	11.24(1.45)
[111]	0.1	0.10(0.00)	0.71(0.01)	0.10(0.00)	0.98(0.04)
[111]	1.0	0.09(0.01)	0.99(0.01)	0.10(0.00)	6.55(0.23)

Table 3.1: Characteristic times t_{BL} for ballistic motion and t_{cage} for caging motion the hotter and colder L/S interfaces for $\varepsilon_{LS} = 0.1, 1.0$. Numbers in parentheses are standard deviation values. All values are reported in reduced units.

3.3.3 Density of states

The DOS [Eq. (1.16)] was used to quantify the population of vibrational modes occupying different frequencies in the contact layer and the first solid layer. As shown in Fig. 3.5, the DOS distribution for the contact layer is a relatively narrow, single-peaked spectrum, whereas the corresponding the DOS for the first solid layer exhibits multiple peaks over a wider frequency range ($0 < \nu < 14$) . These observations are consistent with the reported features of the DOS obtained in the past MD studies [18, 38]). A significant fraction of the spectrum for the contact layer lies below the ballistic frequency ν_{BL} which is $\nu_{BL} \sim 10$ for the [001] and [111] facet and $\nu_{BL} \gtrsim 6$ for the [011] facet irrespective of ε_{LS} (Section 3.3.2). This implies that vibrational motions during the ballistic regime play negligible roles in the overall dynamical behaviors of the contact layer. When ε_{LS} is increased, the DOS distributions for both the contact layer and the first solid layer shift rightward and become broader, both effects leading to the enhanced contributions from high frequency modes. The Frenkel frequency ν_F, which sets a lower bound on the oscillation frequency of liquid particles, is given by the reciprocal of the average time a liquid particle undergoes caging motion. Therefore, we may estimate the Frenkel frequency as $\nu_F \sim \nu_{cage}$. From Fig. 3.4(b), it is readily seen that ν_F shifts leftward as ε_{LS} is incremented, thus augmenting the frequency range supported by the cage motion.

3.3.4 Frequency description of TBR

In the context of elastic phonon transport across the S/S interface, the acoustic mismatch model [32, 69] assumes that vibrational modes with some frequency ν interact only with other modes with the same frequency, implying that the thermal boundary resistance becomes smaller when more vibrational modes of a given frequency become available on both sides of the interface. The concept of frequency overlap, which is often evaluated by computing the area under which two the DOS distributions overlap [11], has been employed in past MD studies in order to vibrationally analyze heat transfer across the L/S interface. The acoustic mismatch model, however, assumes cryogenic temperatures where inelastic phonon scattering is very close to nonexistent [69], and whether the concept of frequency overlap is applicable to the L/S interface remains open to question. A number of past MD works reported that frequency overlap changes very little compared to thermal boundary resistance, concluding that, unlike the heat transfer across the S/S interface, the concept of frequency overlap is not useful in the context of L/S interface [1, 29, 83]. Several other MD works reported otherwise, i.e., that greater frequency overlap is intimately related to enhanced heat transfer across the L/S system [18, 23].

Here, we propose to characterize the frequency overlap between interfacial liquid and solid atoms by evaluating the frequency ratio ν_S^*/ν_L^*, where ν_S^* is the peak frequency at which the DOS of the solid layer reaches global maximum, and ν_L^* is the peak frequency of the total the DOS of the contact layer. From our earlier inspection of the DOS, we know that ν_S^*/ν_L^*

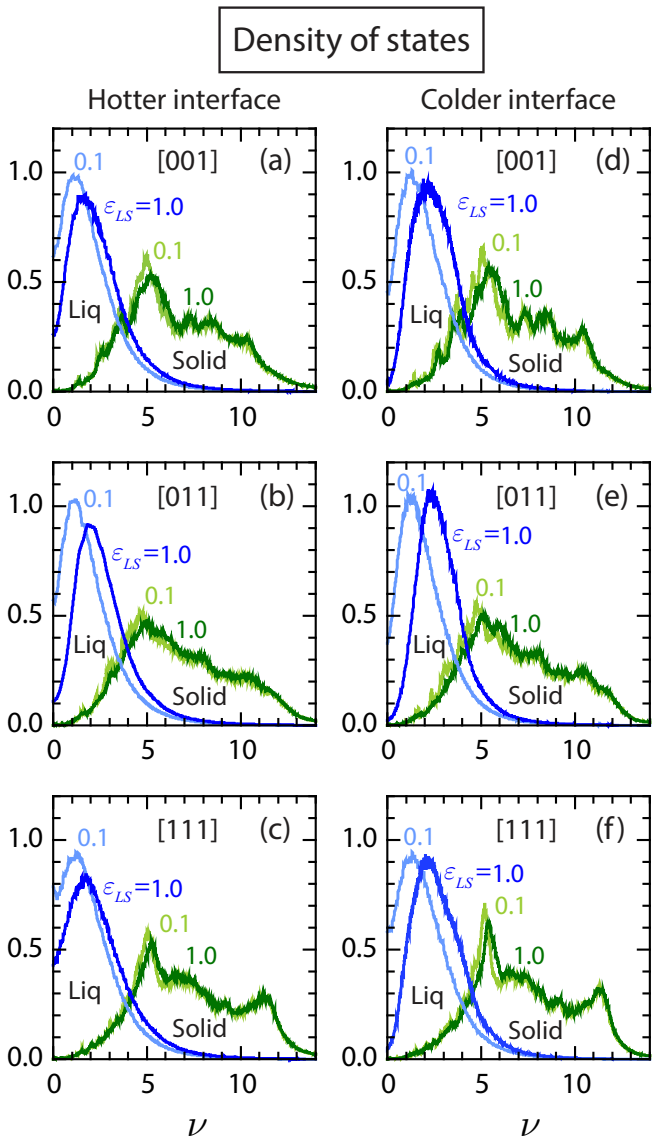

Figure 3.5: Density of states [Eq. (1.16)] of the first liquid solid layers at (a)–(c) the hotter and (d)–(f) colder interfaces where ε_{LS} = 0.1 and 1.0.

is always greater than 1, and gradually approaches 1 when the two the DOS distributions approach each other.

As shown in Fig. 3.6(a), the peak frequency ratio tends to decrease when ε_{LS} is increased, reflecting that the DOS distributions for the interfacial solid and liquid approach each other in the presence of strongly-wetting L/S interactions. Higher temperature yields larger frequency ratio (greater mismatch), because the DOS of the contact layer shifts leftward, i.e., becomes more diffusive, at higher temperatures. As a general feature, the [011] interface yields smaller frequency ratios compared to the [001] or [111] interface. Also, the frequency ratios obtained from [001] and [111] interfaces are roughly comparable to each other. For

the [011] interface, we observe an abrupt drop in the frequency ratio over $0.4 \leq \varepsilon_{LS} \leq 0.8$ for the colder interface, and at $\varepsilon_{LS} = 0.8$ for the hotter interface. This abrupt behavior presumably arises from the structural transition resulting in an epitaxial locking of the liquid particles within the contact layer (Section 2.3).

In Fig. 3.6(b), the results from all simulation runs are summarized to analyze the overall effects of the peak frequency ratio on the thermal slip length across three FCC facets. Here, the explicit temperature dependence is taken into account by evaluating $L_T T_c^{\gamma}$ where T_c is the temperature of the contact layer and $\gamma = 1.5$ is suitably chosen so that data from the hotter and colder interfaces merge onto each other. Remarkably, the data obtained across three FCC facets at different temperature and surface wettability converge onto a master curve given by

$$L_T T^{1.5} = a_T \left(\frac{\nu_S}{\nu_L} \right)_T^b, \tag{3.3}$$

where $a_T = 0.506 \pm 0.104$ and $b_T = 2.660 \pm 0.172$ were obtained through data fitting. A rapid increase of $L_T T^{1.5}$ with respect to ν_S/ν_L is consistent with a classical description, e.g., the acoustic mismatch model, which ascribes the physical origin of thermal boundary resistance to the mismatch in the acoustic impedance $Z_i \propto \nu_i$ $(i = L, S)$ between solids and liquids. The positive correlation between the thermal boundary resistance and the frequency ratio was previously implied by Kim et al. [33] in their MD simulations of liquid argon sandwiched between FCC crystal walls. They evaluated the temperature jumps across the L/S interfaces by systematically varying the thickness of the liquid region, and reported that TBR could be described as a function of the surface wettability, wall temperature, and frequency ratio. Likewise, Hasan et al. [23] performed a series of non-equilibrium MD simulations to explore thermal transport between liquid argon and monolayer-coated FCC crystal walls, and changed the mass of the interfacial monolayer and the interaction energy among monolayer particles to find that thermal slip length obeys a forth-order polynomial of ν_M/ν_L where ν_M denotes the oscillation frequency of the monolayer. The implication behind Eq. (3.3) is more robust than these earlier findings, since cumulative effects due to variations in surface wettability, wall temperature, and solid surface geometry are neatly summarized in a simple functional form.

3.4 Discussion

To gain fundamental insights into the vibrational dynamics that governs in-plane heat transfer across the L/S interface, we examined the DOS distributions of the interfacial liquid and solid layers (Fig. 3.5) and quantified the vibrational mismatch by computing the peak frequency ratio ν_S^*/ν_L^*. When ε_{LS} is increased, the DOS distribution for the contact layer shifts rightward, and consequently the vibrational overlap between the interfacial liquid and solid layers is improved (ν_S^*/ν_L^* approaches unity). Comparing $\nu_S^*/\nu_L^* L$ for three FCC facets at given ε_{LS}, we have found that the [011] facet leads to the best vibrational coupling with the contact layer. Based on these observations, it is sensible to expect that the well-known

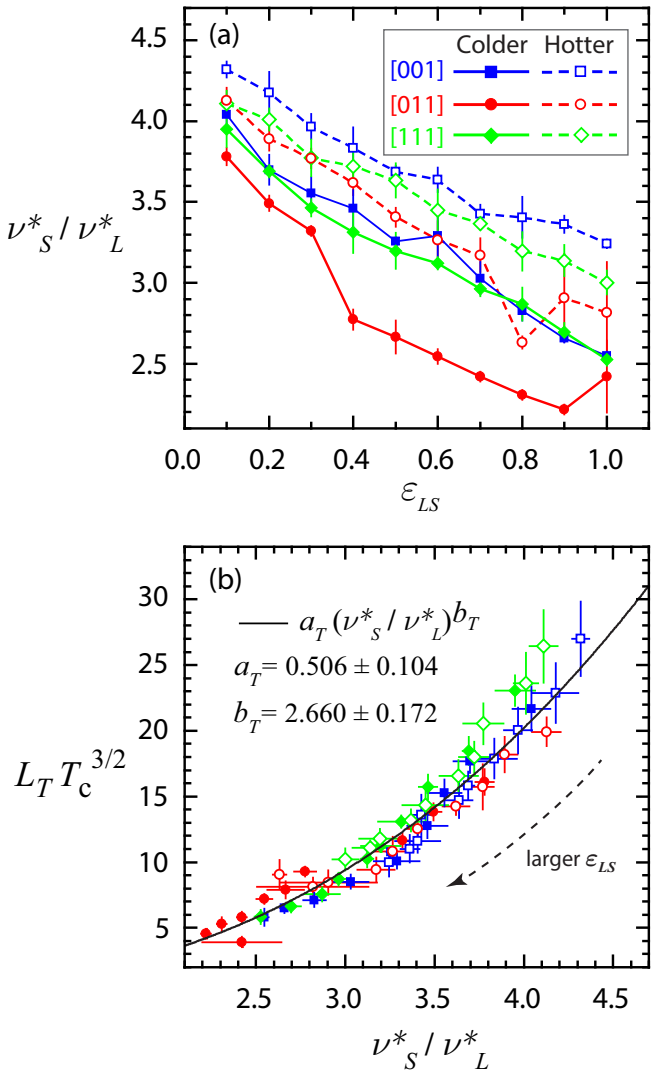

Figure 3.6: Peak frequency ratio and thermal slip length. (a) ν_S/ν_L vs. ε_{LS} across three FCC facets at colder interface and hotter interfaces. Symbols (data) are connected by colored line segments for visual clarity. (b) $L_T T_c^{3.5}$ vs. ν^*_S/ν^*_L obtained from all interfaces examined in this study. Black solid curve represents the master curve relation in Eq. (3.3) fitted against measurements from NEMD simulations. Obtained values of fitting parameters are obtained to be $a_T = 0.506 \pm 0.104$ and $b_T = 2.660 \pm 0.172$.

wettability dependence of the thermal slip length [Fig. 2.4(a)] and low TBR across the [011] facet are both due to an enhanced liquid ordering which in turn increases high frequency modes within the contact layer.

To support this, we have constructed the master relation among the thermal slip length, peak frequency ratio, and interfacial temperature [Eq. (3.3)] which successfully unifies the wettability and temperature dependencies of the thermal slip length as well as the configurational effects arising from the choice of solid surface geometry. Our model suggests

that the thermal boundary resistance across the L/S interface is primarily governed by the vibrational matching as conjectured by the acoustic mismatch model and also by the local temperature of the contact layer. As seen in Fig. 3.6(a), higher interfacial temperature undermines the L/S vibrational coupling (larger ν_S^*/ν_L^*), but at the same time enhances the overall thermal transport (smaller thermal slip length). This behavior which deviates from the simplified description based on the vibrational matching could be explained in terms of anharmonic phonon scattering across the hotter interface [69]. That is, higher interfacial temperature permits high-frequency modes populating the interfacial solids to interact with low-frequency modes within the contact layer, thus promoting additional vibrational modes to participate in heat transfer. Indeed, past simulation-based investigations reported that diffusive phonon scattering arising from the anharmonic interaction improves thermal transport in the S/S systems [19, 61, 63].

Table 3.2: Characteristic frequencies obtained from NGP ($\nu_{cage} = 1/t_{cage}$ for caging motion and $\nu_{BL} = 1/t_{BL}$ for ballistic motion), peak frequencies from the DOS (ν_L^* for contact layer and ν_S^* for first solid layer), and the ratio ν_S^*/ν_L^* obtained for different choices of crystal facet orientation. Numbers in parentheses are standard deviation values. All values are reported in reduced units.

		Hotter interface					Colder interface				
Facet	ε_{LS}	ν_{cage}	ν_{BL}	ν_L^*	ν_S^*	ν_S^*/ν_L^*	ν_{cage}	ν_{BL}	ν_L^*	ν_S^*	ν_S^*/ν_L^*
[001]	0.1	0.69(0.04)	10.00(0.00)	1.15(0.02)	4.98(0.01)	4.32(0.05)	0.54(0.02)	8.33(0.00)	1.27(0.03)	5.12(0.01)	4.04(0.11)
[001]	0.2	0.68(0.04)	9.38(1.01)	1.20(0.04)	5.01(0.00)	4.18(0.13)	0.48(0.03)	8.82(0.90)	1.39(0.03)	5.14(0.00)	3.70(0.09)
[001]	0.3	0.66(0.03)	8.82(0.90)	1.27(0.03)	5.02(0.01)	3.97(0.08)	0.43(0.01)	9.38(1.01)	1.45(0.04)	5.16(0.01)	3.55(0.10)
[001]	0.4	0.64(0.04)	9.38(1.01)	1.32(0.05)	5.06(0.01)	3.83(0.13)	0.42(0.01)	8.33(0.00)	1.51(0.05)	5.21(0.01)	3.46(0.11)
[001]	0.5	0.65(0.01)	9.38(1.01)	1.38(0.01)	5.08(0.01)	3.69(0.04)	0.37(0.01)	9.38(1.01)	1.61(0.01)	5.23(0.00)	3.26(0.02)
[001]	0.6	0.59(0.03)	9.38(1.01)	1.40(0.03)	5.10(0.02)	3.64(0.07)	0.33(0.02)	8.33(0.00)	1.61(0.06)	5.29(0.01)	3.29(0.13)
[001]	0.7	0.59(0.01)	10.00(0.00)	1.50(0.02)	5.13(0.01)	3.43(0.06)	0.29(0.01)	9.38(1.01)	1.76(0.06)	5.32(0.01)	3.03(0.10)
[001]	0.8	0.59(0.02)	10.00(0.00)	1.52(0.06)	5.16(0.01)	3.41(0.13)	0.23(0.01)	9.38(1.01)	1.90(0.04)	5.38(0.01)	2.83(0.06)
[001]	0.9	0.56(0.04)	10.00(0.00)	1.55(0.03)	5.21(0.01)	3.36(0.05)	0.20(0.01)	9.38(1.01)	2.05(0.02)	5.44(0.01)	2.66(0.02)
[001]	1.0	0.55(0.01)	10.00(0.00)	1.62(0.01)	5.24(0.01)	3.24(0.01)	0.13(0.00)	8.33(0.00)	2.16(0.01)	5.50(0.01)	2.55(0.01)
[011]	0.1	0.46(0.04)	9.38(1.01)	1.14(0.02)	4.69(0.02)	4.13(0.08)	0.30(0.03)	8.33(0.00)	1.27(0.02)	4.81(0.03)	3.78(0.05)
[011]	0.2	0.48(0.03)	10.00(0.00)	1.22(0.02)	4.73(0.02)	3.89(0.07)	0.26(0.05)	8.33(0.00)	1.39(0.02)	4.85(0.02)	3.49(0.05)
[011]	0.3	0.38(0.04)	10.00(0.00)	1.26(0.02)	4.75(0.00)	3.77(0.06)	0.21(0.03)	8.82(0.90)	1.47(0.01)	4.87(0.01)	3.32(0.03)
[011]	0.4	0.44(0.03)	9.38(1.01)	1.32(0.03)	4.78(0.01)	3.62(0.07)	0.43(0.04)	7.14(0.00)	1.76(0.04)	4.89(0.01)	2.77(0.06)
[011]	0.5	0.37(0.04)	10.00(0.00)	1.41(0.02)	4.79(0.01)	3.41(0.06)	0.36(0.05)	7.14(0.00)	1.85(0.06)	4.93(0.02)	2.67(0.10)
[011]	0.6	0.36(0.04)	10.00(0.00)	1.48(0.06)	4.84(0.01)	3.26(0.12)	0.31(0.02)	7.14(0.00)	1.95(0.03)	4.96(0.02)	2.55(0.04)
[011]	0.7	0.30(0.06)	10.00(0.00)	1.53(0.05)	4.86(0.00)	3.17(0.10)	0.20(0.02)	7.14(0.00)	2.07(0.01)	5.00(0.01)	2.42(0.01)
[011]	0.8	0.47(0.02)	8.33(0.00)	1.86(0.03)	4.89(0.01)	2.63(0.04)	0.18(0.01)	7.14(0.00)	2.18(0.01)	5.02(0.01)	2.31(0.01)
[011]	0.9	0.48(0.01)	7.89(0.72)	1.91(0.02)	5.56(0.57)	2.91(0.27)	0.12(0.01)	7.14(0.00)	2.29(0.01)	5.09(0.01)	2.22(0.00)
[011]	1.0	0.44(0.02)	8.33(0.00)	1.99(0.02)	5.59(0.57)	2.82(0.31)	0.09(0.01)	6.52(0.49)	2.36(0.03)	5.72(0.50)	2.42(0.22)
[111]	0.1	1.42(0.02)	10.00(0.00)	1.23(0.02)	5.04(0.00)	4.11(0.08)	1.02(0.04)	10.00(0.00)	1.32(0.04)	5.20(0.00)	3.95(0.11)
[111]	0.2	1.28(0.06)	10.00(0.00)	1.26(0.02)	5.07(0.01)	4.01(0.07)	0.99(0.01)	10.00(0.00)	1.41(0.01)	5.22(0.01)	3.69(0.01)
[111]	0.3	1.23(0.06)	10.00(0.00)	1.35(0.04)	5.09(0.00)	3.77(0.11)	0.83(0.08)	10.00(0.00)	1.51(0.02)	5.24(0.00)	3.46(0.05)
[111]	0.4	1.19(0.12)	10.00(0.00)	1.37(0.03)	5.11(0.01)	3.72(0.09)	0.77(0.07)	10.00(0.00)	1.59(0.06)	5.26(0.01)	3.31(0.13)
[111]	0.5	1.13(0.04)	10.00(0.00)	1.41(0.04)	5.13(0.01)	3.63(0.11)	0.71(0.03)	10.00(0.00)	1.65(0.06)	5.28(0.01)	3.20(0.11)
[111]	0.6	1.10(0.04)	10.00(0.00)	1.50(0.06)	5.16(0.01)	3.45(0.13)	0.63(0.01)	10.00(0.00)	1.70(0.02)	5.31(0.01)	3.12(0.03)
[111]	0.7	1.04(0.00)	10.00(0.00)	1.54(0.01)	5.17(0.01)	3.37(0.02)	0.54(0.03)	10.00(0.00)	1.80(0.03)	5.33(0.01)	2.96(0.04)
[111]	0.8	1.01(0.05)	10.00(0.00)	1.63(0.06)	5.20(0.01)	3.20(0.12)	0.40(0.01)	10.71(1.33)	1.87(0.07)	5.36(0.00)	2.87(0.10)
[111]	0.9	0.98(0.05)	10.71(1.33)	1.67(0.05)	5.23(0.01)	3.14(0.10)	0.29(0.03)	10.00(0.00)	2.00(0.04)	5.40(0.00)	2.70(0.05)
[111]	1.0	1.01(0.01)	10.71(1.33)	1.75(0.04)	5.25(0.00)	3.00(0.07)	0.15(0.01)	10.00(0.00)	2.15(0.03)	5.44(0.00)	2.53(0.03)

Chapter 4

DEPENDENCE OF TBR ON STRUCTURAL AND DYNAMICAL COMMENSURABILITY BETWEEN LIQUID AND SOLID LAYERS

4.1 Overview of this chapter

In this chapter, we used non-equilibrium molecular dynamics (NEMD) simulations to study thermal transport in a simple monatomic liquid confined between two crystalline walls whose exterior layers are maintained at different temperatures. By varying the energy parameter (wettability) and length parameter (repulsive distance) characterizing the L/S interaction and the temperature difference imposed on the system, we observed correlations between the thermal jump or thermal slip length and structural properties of the contact layer and analyzed their dependence on the local temperature at the interface. We argue that common descriptions of the contact layer including the contact density and depletion layer thickness cannot serve as a single unifying descriptor reflecting the effect of simultaneously changing the length and energy parameters on TBR. As an alternative, the 2D static structure factor was used to quantify a degree of spatial commensurability between the contact layer and surface potential of the adjacent solid. In the context of the fluid velocity slip at solid surfaces, the static structure factor has proven useful to understanding the momentum transfer across L/S interfaces [57, 74], but its significance in thermal transport has been much underestimated. To the extent of our knowledge, no previous work has provided a quantitative description of how in-plane liquid ordering affects thermal energy exchange between liquid and solid particles. We report that a simultaneous variation of the length and energy parameters result in a strong correlation between the thermal slip length and structure factor, suggesting that in-plane liquid ordering in directions normal to the heat flux plays more fundamental role in heat transfer than simple density enhancement.

We also explored the role of harmonic vibrational coupling on the interfacial thermal transport by computing the DOS of the contact layer and first solid layer. Instead of the DOS overlap commonly employed in MD studies, we measured the ratio of peak frequencies of the first solid layer and contact layer to quantify a degree of proximity between the DOS distributions of these layers. From the result of simulations, we constructed two types of master curve relations for the thermal slip length, the first expressing the thermal slip length in terms of the peak value of the structure factor and contact layer temperature and the second describing the correlation between the thermal slip length and peak frequency ratio. Both master curves were confirmed to be in excellent agreement with the measurements simulations within the parametric range explored.

Table 4.1: Heat source temperature T_{source} and heat sink temperature T_{sink} used in three cases. All numerical values are reported in reduced units.

ΔT_{Lang}	T_{source}	T_{sink}
1.0	1.8	0.8
0.6	1.6	1.0
0.2	1.4	1.2

Variable	Value in scaled units
mass of each particle	1
LJ particle diameter	$\sigma_{LL} = \sigma_{SS} = 1.0$
	$\sigma_{LS} = 0.8, 1.0, 1.2$
LJ interaction energy	$\varepsilon_{LL} = 1.0$
	$\varepsilon_{LS} = 0.1 - 1.0$
	$\varepsilon_{SS} = 10$
FCC edge length	$a = 1.560$
integration time step	$\Delta t_{int} = 0.002$
source temperature	$T_{\text{source}} = 1.8$ ($\Delta T_{Lang} = 1.0$), 1.6 ($\Delta T_{Lang} = 0.6$)
	1.4 ($\Delta T_{Lang} = 0.2$)
sink temperature	$T_{\text{sink}} = 0.8$ ($\Delta T_{Lang} = 1.0$), 1.0 ($\Delta T_{Lang} = 0.6$)
	1.2 ($\Delta T_{Lang} = 0.2$)
bulk liquid density	$\rho_L \approx 0.84$
FCC unit cell density	$\rho_S = 1.0536$
FCC crystal facet	[001]

Table 4.2: List of simulation parameters employed in Chapter 4. All numerical values are reported in dimensionless units detailed in Table1.1.

4.2 Simulation parameters

In this project, the following three simulation parameters were varied simultaneously: The L/S repulsive distance σ_{LS}, the L/S interaction energy ε_{LS}, and the temperature difference $\Delta T_{Lang} = T_{source} - T_{sink}$. To exert sizeable effects on a degree of liquid layering at the interface, we used $\sigma_{LS} = 0.8, 1.0, 1.2$ for the length parameter of the L/S interaction potential. For each value of σ_{LS}, ε_{LS} was gradually increased from 0.1 to 1.0 in increments of 0.1 in order to study the wettability dependence of structural and thermal properties characterizing the L/S interface. Finally, we tested $\Delta T_{Lang} = 1.0, 0.6, 0.2$ to explore heat transfer in the presence of high, moderate, and low levels of thermal gradients, respectively. Temperatures of the heat source and heat sink corresponding to each value of ΔT_{Lang} are summarized in Table 4.1. The temperature dependence of TBR and other interfacial properties was analyzed by comparing the measurements taken at the hotter and colder interfaces for different choices of ΔT_{Lang}. The numerical values of other simulation parameters are summarized in Table 4.2.

4.3 Results

4.3.1 Heat flux and thermal jump across the interface

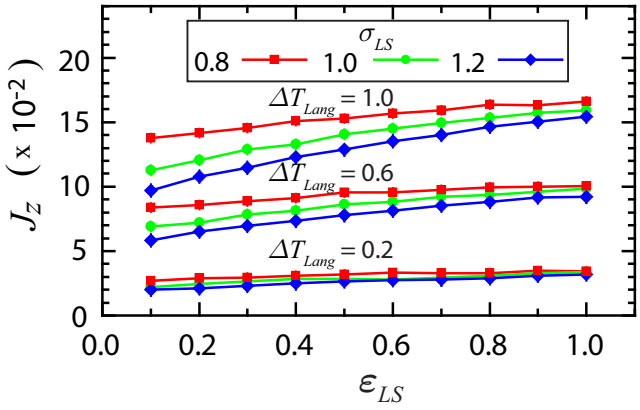

Figure 4.1: Dependence of steady thermal flux J_z on L/S interaction parameters ε_{LS} and σ_{LS} in the systems where $\Delta T_{Lang} = 1.0, 0.6, 0.2$. The connecting segments are only a guide to the eye.

The heat flux measurements in different systems employed in this work are shown in Fig. 4.1. A notable dependence on the energy parameter ε_{LS} as well as the length parameter σ_{LS} implies that the L/S interactions at the hotter and colder L/S interfaces have sizeable effects on the global heat transfer. It is trivially seen that J_z is greatest when $\Delta T_{Lang} = 1.0$ and lowest when $\Delta T_{Lang} = 0.2$ irrespective of the values of ε_{LS} and σ_{LS}. Holding other parameters constant, the heat flux gradually increases with increasing ε_{LS} or with decreasing σ_{LS}. The dependence on σ_{LS} appears strongest when the L/S interaction is non-wetting (small ε_{LS}), indicating that the influence of the corrugation of the crystal surface potential on thermal transport slowly diminishes as the L/S interface becomes more wetting.

Shown in Fig. 4.2 is the reduction in the thermal jump across the hotter and colder L/S interfaces for different choices of L/S interaction parameters. As a general behavior, the thermal jump gradually decreases with increasing ε_{LS}. This behavior is widely known, but it is still not well understood what physical mechanism contributes to the reduction of the thermal jump. The more important result is that ΔT decreases significantly upon reducing the repulsive distance σ_{LS}. In most cases, the reduction of σ_{LS} from 1.2 to 0.8 had impact on the thermal jump comparable to incrementing ε_{LS} from 0.1 to 1.0. For instance, the thermal jump at the colder L/S interface for $\varepsilon_{LS} = 0.1$ ($\Delta T_{Lang} = 1.0$) was observed to diminish from 0.316 ± 0.006 to 0.147 ± 0.007 (53 % reduction) by decrementing σ_{LS} from 1.2 to 0.8, whereas the thermal jump at the colder L/S interface for $\sigma_{LS} = 1.2$ ($\Delta T_{Lang} = 1.0$) decreased from 0.316 ± 0.006 to 0.156 ± 0.005 (51 % reduction) as ε_{LS} increased from 0.1 to 1.0. It was also found that the thermal jump varies with the local temperature at the interface but in a subtle manner depending on the L/S interaction parameters as well as the temperature difference between the heat source and heat sink ($T_{\text{source}} - T_{\text{sink}}$). In many cases,

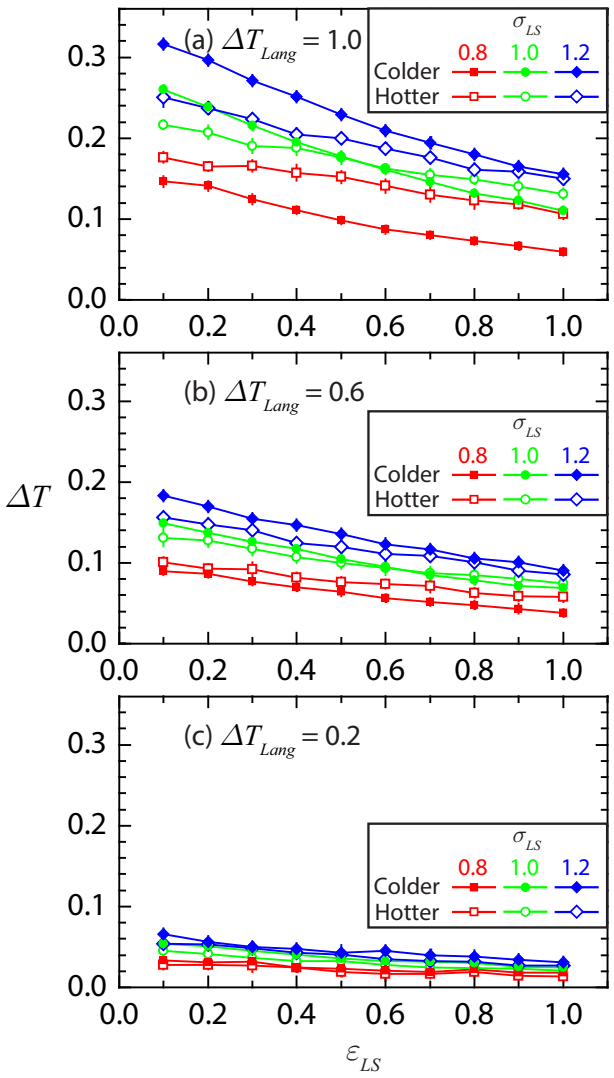

Figure 4.2: Reduction in thermal jump ΔT across the hotter and colder L/S interfaces with increasing L/S interaction energy ε_{LS} for three values of σ_{LS} when the macroscopic temperature difference ΔT_{Lang} is set to (a) 1.0, (b) 0.6, and (c) 0.2. Connecting segments are only a guide to the eye.

the colder interface yields larger thermal jump than the hotter interface, but there are some exceptions (e.g., $\sigma_{LS} = 0.8$ and $0.1 \leq \varepsilon_{LS} \leq 1.0$ when $\Delta T_{Lang} = 1.0$).

The reduction in thermal jump or TBR across the L/S interface is often attributed to the improvement in thermal contact between the liquid and solid particles due to the enhanced contact density (i.e., the liquid density peak immediately next to the solid surface) or smaller depletion layer thickness (the distance between density peaks corresponding to the first solid layer and liquid contact layer). In Table 4.3.1, we show the contact density ρ_c and depletion layer thickness δ at the colder and hotter L/S interfaces for different choices of ΔT_{Lang} and L/S interaction parameters. Irrespective of the choice of ε_{LS}, ρ_c was found to increase

			Hotter interface		Colder interface	
ΔT_{Lang}	σ_{LS}	ε_{LS}	ρ_c	δ	ρ_c	δ
1.0	0.8	0.1	0.92(0.02)	0.65(0.01)	0.10(0.02)	0.47(0.01)
1.0	0.8	1.0	1.34(0.02)	0.61(0.00)	3.59(0.03)	0.43(0.01)
1.0	1.2	0.1	1.44(0.03)	1.05(0.00)	1.80(0.03)	1.02(0.01)
1.0	1.2	1.0	2.26(0.03)	1.12(0.00)	3.82(0.05)	1.08(0.00)
0.6	0.8	0.1	0.95(0.03)	0.62(0.01)	0.99(0.02)	0.51(0.01)
0.6	0.8	1.0	1.48(0.02)	0.56(0.01)	2.79(0.04)	0.44(0.01)
0.6	1.2	0.1	1.51(0.02)	1.05(0.00)	1.70(0.02)	1.04(0.01)
0.6	1.2	1.0	2.44(0.04)	1.12(0.01)	3.30(0.05)	1.09(0.00)
0.2	0.8	0.1	0.97(0.02)	0.60(0.01)	0.95(0.02)	0.62(0.10)
0.2	0.8	1.0	1.77(0.02)	0.51(0.01)	2.20(0.03)	0.48(0.01)
0.2	1.2	0.1	1.58(0.03)	1.04(0.01)	1.64(0.03)	1.04(0.01)
0.2	1.2	1.0	2.67(0.04)	1.11(0.01)	2.92(0.05)	1.09(0.01)

Table 4.3: The contact density ρ_c and the depletion layer thickness δ at the hotter and colder L/S interfaces for $\sigma_{LS} = 0.8, 1.2$ and $\varepsilon_{LS} = 0.1, 1.0$. Numbers in parentheses are standard deviation values. All values are reported in reduced units.

upon incrementing the value of σ_{LS}. However, the results from Fig. 4.2 indicates that the thermal jump increases in the same manner, or, equivalently, the enhanced contact density does not necessarily lower the thermal jump. The depletion layer thickness, on the other hand, directly scales with σ_{LS} but unaffected by the value of ε_{LS}, making it unsuitable for describing the thermal jump reduction with respect to the interaction energy parameter. To summarize, neither the contact density nor depletion layer thickness alone satisfactorily explains the effects of varying both interaction parameters (σ_{LS} and ε_{LS}) simultaneously.

4.3.2 2D static structure factor

We employed the 2D static structure factor given in Eq. (1.10) to quantify a degree of commensurability between the liquid ordering in the contact layer and the crystal plane forming the first solid layer. As reported in the past computational studies, the liquid particles subject to the strongly-wetting L/S interaction display a high degree of translational long-range order which leads to pronounced peaks at the 2D reciprocal lattice vectors of the crystal plane next to the contact layer

The global maximum of the static structure factor is found at any one of the shortest reciprocal lattice vectors:

$$S_{max} = S_c^{\parallel}(\vec{k}_o) \ . \tag{4.1}$$

Here, $\vec{k}_o = (\pm 4.03, \pm 4.03)$ or $(\mp 4.03, \pm 4.03)$ is the shortest reciprocal lattice vector of the [001] crystal plane of the FCC lattice. In Fig. 4.3(a)–(c), S_{max} is plotted as a function of the L/S interaction energy ε_{LS}. As a general feature, stronger L/S interaction energy (larger ε_{LS})

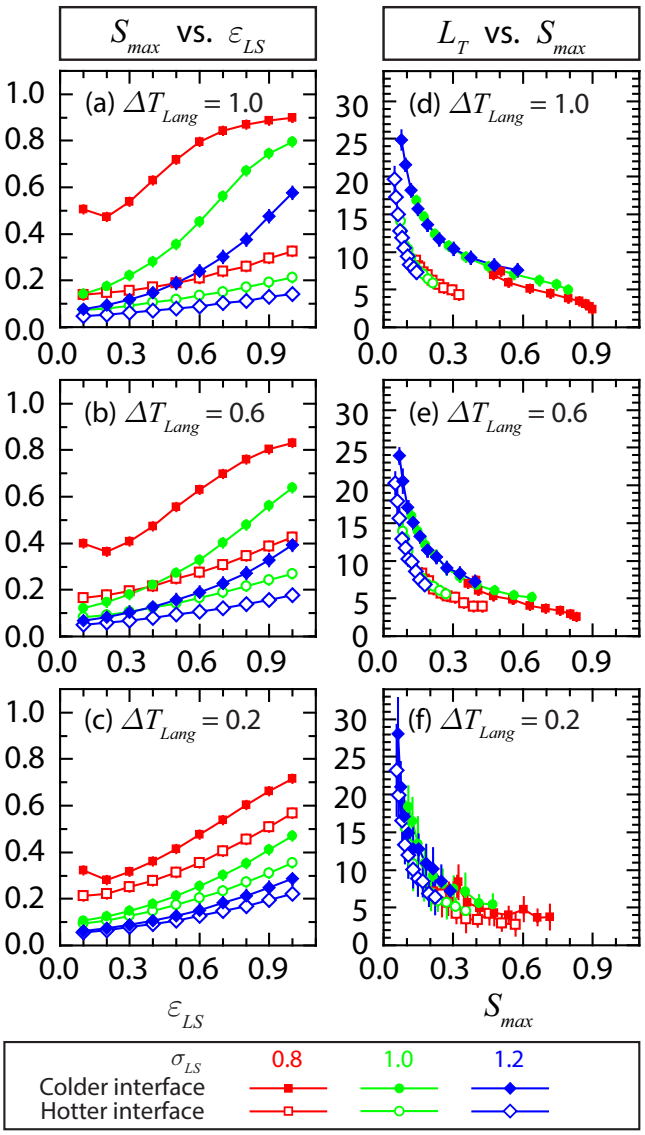

Figure 4.3: Structure factor and thermal slip length. Left: First peak S_{max} of the 2D static structure factor for particles in the hotter and colder L/S interfaces for $\sigma_{LS} = 0.8, 1.0, 1.2$ when ΔT_{Lang} is set to (a) 1.0, (b) 0.6, and (c) 0.2. Right: Reduction in the thermal slip length L_T with increasing S_{max} for $\sigma_{LS} = 0.8, 1.0, 1.2$ when ΔT_{Lang} is set to (d) 1.0, (e) 0.6, and (f) 0.2. Connecting segments are only a guide to the eye.

improves the in-plane liquid ordering within the contact layer (larger S_{max}) by enforcing the periodic pattern set by the corrugation of the crystal surface potential. The reduction in σ_{LS} leads to a sizeable increase in S_{max}. This is because the close proximity between the liquid and solid particles enhances the contributions from the short-range repulsive term in the LJ potential, thereby inducing highly correlated energy barriers which make the crystal surface potential more corrugated. Note that S_{max} does not increase indefinitely with ε_{LS}.

4.3.2.1 Master curve relation

The correlation between the thermal slip length L_T defined in Eq. (1.2) and S_{max} is shown in Fig. 4.3(d)–(f). For all interfaces, the thermal slip length was observed to decay monotonically with respect to S_{max} as ε_{LS} is increased or σ_{LS} is decreased. A number of past computational studies reported that the static structure factor is strongly correlated with strong correlated with the velocity slip across the L/S interface [74], but an analogous correlation with the thermal slip length have not explicitly analyzed in the previous works. Remarkably, the data points obtained using different values of L/S interaction parameters (ε_{LS} and σ_{LS}) collapse onto each other at both the hotter and colder interfaces. In each case, the thermal slip length across the hotter interface is consistently lower than its counterpart across the colder interface when plotted against S_{max}. Based on these observations, we may determine two types of mechanism which reduce TBR at the L/S interface. The first mechanism is the athermal coupling due to stronger commensurability between the liquid and solid layers. The second is the thermal excitation of high frequency modes which offer additional contribution to the energy transport across the interface.

It is possible to collapse all data points in Fig. 4.3(d)–(f) onto a single curve by explicitly taking the local temperature dependence into account, i.e., by scaling L_T with a suitable function of the contact layer temperature which was evaluated using the equipartition theorem. As shown in Fig. 4.4, the data points from all interfaces subject to different levels of thermal gradients ($\Delta T_{Lang} = 1.0$) collapse onto each other when $L_T T c^2$ is plotted against S_{max}. Here, the exponent of T_c was empirically determined to yield the best convergence among the data set. On the log-log scale, $L_T T c^2$ decreases almost linearly with S_{max} throughout the interval $0 < S_{max} \lesssim 0.7$, indicating that the "master curve" is given by the power-law fit:

$$L_T T_c^2 = \alpha S_{max}^{-\beta}. \tag{4.2}$$

Eq. (4.2) was fitted against all data points satisfying $S_{max} < 0.7$. The free parameters in Eq. (4.2) were found to be $\alpha = 4.09 \pm 0.07$ and $\beta = -0.80 \pm 0.01$. As indicated in Fig. 4.3, the proposed model is in excellent agreement with the data points when S_{max} is smaller than approximately 0.7. For higher values of S_{max}, $L_T T_c^2$ drops more rapidly than Eq. (4.2) likely because the contact layer enters the solid-like regime where S_{max} starts to asymptote towards a maximal level.

4.3.3 Frequency description of TBR

To gain additional insights into the effects of altering the two L/S interaction parameters, we computed the DOS of the first solid layer and contact layer using Eq. (1.16) and thereon evaluated the ratio of frequencies ν_S^*/ν_L^* where ν_S^* and ν_L^* are the dominant frequencies (i.e., where the DOS reaches its global maximum value) of the first solid layer and contact layer,

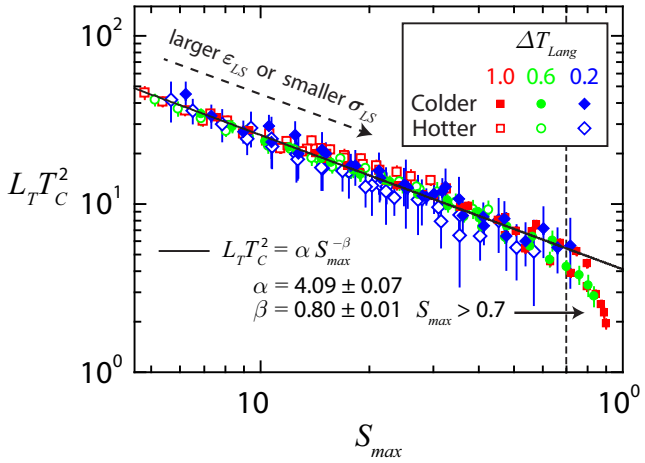

Figure 4.4: $L_T T_C^2$ plotted against S_{max} for $\Delta TLang = 1.0$ (blue squares), 0.6 (red circles), and 0.2 (green diamonds). The solid curve represents the master curve relation in Eq (4.2) with the fitted parameter values $\alpha = 3.82 \pm 0.07$ and $\beta = 0.83 \pm 0.01$. As explained in the text, data points from L/S interfaces where $S_{max} > 0.7$ (dashed vertical line) were excluded from the fitting analysis.

respectively. The contact layer is predominantly occupied by low-frequency modes, so we expect the ratio to be greater than unity. In Fig. 4.5, we find that the ratio is anomalously small when $\varepsilon_{LS} = 0.1$ and $\sigma_{LS} = 0.8$ (leftmost filled/empty squares). Excluding these anomalous data points, the ratio is observed to be a gradually decreasing function of ε_{LS}, indicating that stronger L/S interaction results in greater high-frequency contributions (i.e., higher ν_L^*) to the vibrational coupling between the interfacial liquid and solid structures. The ratio also decreases upon lowering the local temperature near the L/S interface. For the colder interfaces, the ratio tends to be smallest for $\sigma_{LS} = 0.8$ throughout the interval $0.1 \leq \varepsilon_{LS} \leq 1.0$. For the hotter interface, on the other hand, the ratio becomes nearly insensitive to the variation in σ_{LS}.

4.3.3.1 Master curve relation

We report that the ratio ν_S^*/ν_L^* serves as a useful variable reflecting the effect of L/S interactions on TBR. In Fig. 4.6, we demonstrate a strong correlation between ν_S^*/ν_L^* and the quantity $L_T T_c^{\gamma}/\sigma_{LS}^q$ where the scaling exponents were chosen to be $\gamma \sim 1.5$ and $q \sim 2$ through trial and error. The data points from the simulations were fitted against the following master curve relation:

$$\frac{L_T T_c^{1.5}}{\sigma^2} = A\left(\frac{\nu_S^*}{\nu_L^*}\right)^{-\gamma}, \tag{4.3}$$

with the fitting parameters $A = 0.34 \pm 0.02$ and $\gamma = 2.95 \pm 0.05$ determined using all data points excluding the six anomalous points obtained using $\varepsilon_{LS} = 0.1$ and $\sigma_{LS} = 0.8$).

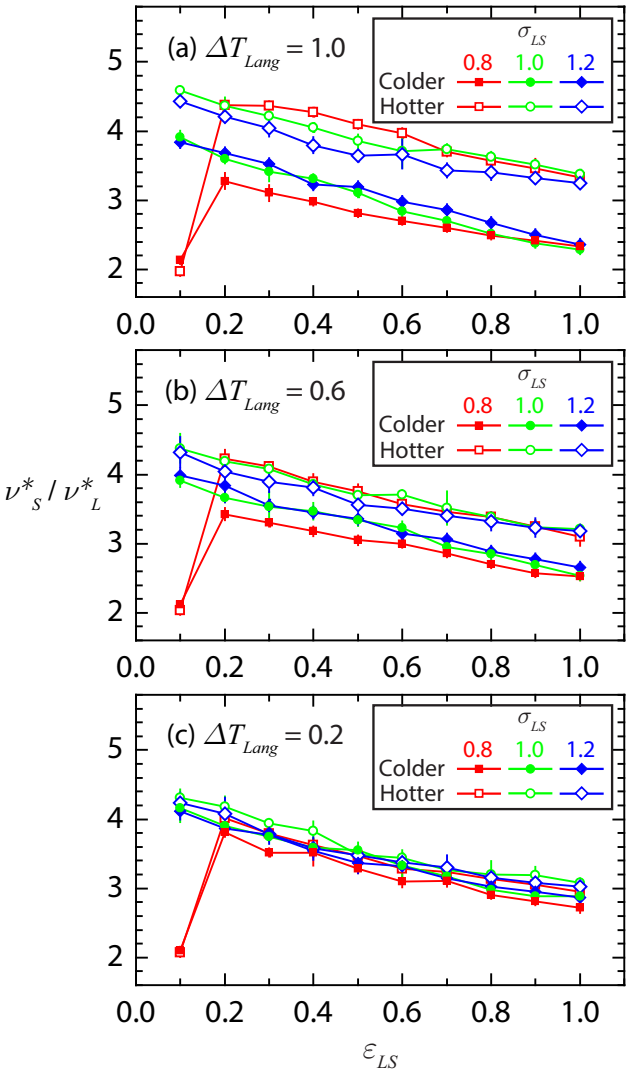

Figure 4.5: Dependence of peak frequency ratio ν_S/ν_L across hotter and colder L/S interfaces on L/S interaction energy when ΔT_{Lang} is set to (a) 1.0, (b) 0.6, and (c) 0.2. Connecting segments are only a guide to the eye.

The function form of Eq. (4.3) closely resembles that of the master curve relation in Eq. (3.3) which was obtained by changing the orientations of the crystal lattice (Section 3.3). Once again, the thermal slip length decreases upon lowering ν^*_S/ν^*_L (i.e., improving the vibrational matching across the interface) or increasing the contact layer temperature (i.e., exciting additional vibrational modes contributing to heat transfer). From the results in Fig. 4.5, smaller values of σ_{LS} tend to reduce the ratio ν^*_S/ν^*_L, indirectly lowering the TBR by diminishing the acoustic mismatch between the liquid and solid layers. However, the explicit dependence of Eq. (4.3) on σ_{LS} indicates that variation in σ_{LS} have an additional effect that reduces the thermal slip length besides the improvement in the vibrational matching. This effect is presumably due to an enhanced local ordering of liquid particles in the contact layer

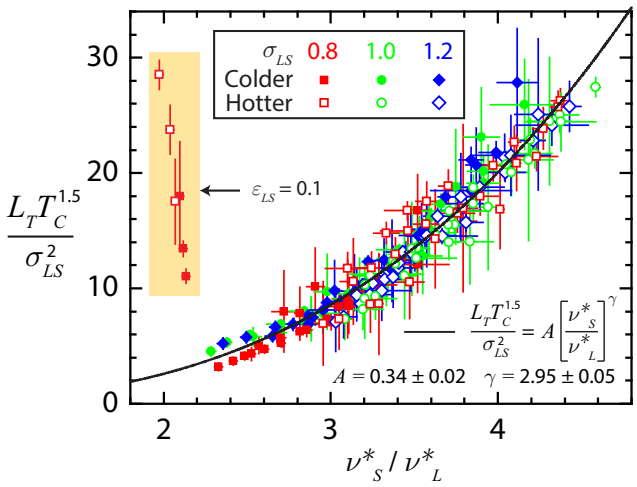

Figure 4.6: $L_T T_C^2/\sigma^2$ plotted against ν_S^*/ν_L^* for $\sigma_{LS} = 0.8$ (blue squares), 1.0 (red circles), and 1.2 (green diamonds). The solid curve represents the master curve relation in Eq. (4.3) with the fitted parameter values $A = 0.34 \pm 0.02$ and $\gamma = 2.95 \pm 0.05$. Six data points obtained using $\varepsilon_{LS} = 0.1$ and $\sigma_{LS} = 0.8$ (shaded region) were excluded from the fitting analysis.

(i.e., higher S_{max}) as seen in Fig. 4.3(d)–(f).

4.4 Discussion

As reported in numerous experiments [20, 46, 56] and particle-based simulations [2, 10, 17, 21, 22, 49, 50, 53, 59, 65, 66, 92], the reduction in TBR with respect to increasing L/S interaction energy or liquid pressure is often explained in terms of either the enhanced contact density or smaller depletion layer thickness, each of which improves the level of physical contact between the interfacial liquid and solid layers. This conventional description has proven useful in understanding the role of liquid layering on the interfacial thermal transport to certain extent [1, 21]. The results in Fig. 4.2 indicate that thermal jump undergoes sizeable reduction as ε_{LS} is increased or σ_{LS} is decreased. According to the conventional picture, stronger L/S interaction energy (ε_{LS}) results in the denser contact layer (i.e., higher contact density) which in turn increases the rate at which liquid particles exchange thermal energy with solid particles near the interface. The depletion layer thickness scales directly with the L/S repulsive distance(σ_{LS}), so it is reasonable that lower values of σ_{LS} result in smaller thermal jumps.

However, neither the contact density nor depletion layer thickness uniquely determines the relative magnitude of thermal jump or TBR at a given temperature. For instance, the contact density decreases upon reducing the value of σ_{LS}, but the resulting thermal jump diminishes nonetheless. Similarly, the depletion layer thickness is insensitive to the choice of ε_{LS}, so it is not suitable for representing the wettability dependence of TBR.

As an alternative characterization of the contact layer, the global maximum value of the 2D static structure factor in Eq. (1.10) was employed to quantity the commensurability between the local ordering of liquid particles in the contact layer and the spatial pattern of the periodic surface potential induced the nearby crystalline solid. The results in Fig. 4.3(a)–(c) indicate that the contact layer becomes more commensurate to the solid surface potential (i.e., higher S_{max}) as ε_{LS} is increased or σ_{LS} is decreased. Comparing the results in Fig. 4.2(a)–(c) and Fig. 4.3(a)–(c), we observe a direct correspondence between the reduction in thermal jump and the improvement in the local ordering of liquid particles upon varying the L/S interaction parameters simultaneously. Indeed, the results in Fig. 4.3(d)–(f) indicate that the dependence of thermal slip length on the simultaneous variation of two interaction parameters ε_{LS} and σ_{LS} is well described by a single variable S_{max}, thus indicating that the local ordering of liquid particles has far stronger impact on the TBR compared to the contact density or depletion layer thickness.

From the functional form of a master curve relation in Eq. (4.2), it is possible to identify two temperature dependent mechanisms that compete with each other to determine TBR. Ignoring the implicit temperature dependence of S_{max}, the thermal slip length is lowered upon increasing the contact layer temperature, presumably due to the excitation of high frequency modes participating in the interfacial heat conduction. At the same time, a higher contact later temperature perturbs the in-plane liquid ordering in the contact layer and thus deteriorates the physical contact between the liquid and solid layers at the interface.

A role played by L/S interaction in thermal transport was further explored by evaluating the DOS of the contact layer and first solid layer. The acoustic mismatch quantified by the ratio of dominant frequencies (ν_S^*/ν_L^*) exhibits colorful variation with respect to changes in the L/S interaction parameters. Furthermore, the dependencies of thermal slip length on the peak frequency ratio, local temperature, and L/S repulsive distance are well summarized by a master curve relation [Eq. (4.3)] which was shown to be in excellent agreement with most data points obtained from NEMD simulations. These results are consistent with the findings from our earlier simulations using different crystal facet orientations (Section 3.3.4).

Table 4.4: Results of NEMD simulations in the systems where $\Delta T_{Lang} = 1.0$ ($T_{\text{source}} = 1.8$ and $T_{\text{sink}} = 0.8$ showing the influence of L/S interaction parameters ε_{LS} and σ_{LS} on the bulk thermal properties including the thermal flux J_z [Eq. (1.8)], magnitude of the thermal gradient $|dT/dz|$, and thermal conductivity k [Eq. (1.3)] within the bulk solid and liquid away from the L/S interface.

			Liquid		Hotter solid		Colder solid	
σ_{LS}	ε_{LS}	$J_z \times 10^{-2}$	$\lvert dT/dz\rvert \times 10^{-2}$	k	$\lvert dT/dz\rvert \times 10^{-4}$	$k \times 10^2$	$\lvert dT/dz\rvert \times 10^{-4}$	$k \times 10^2$
0.8	0.1	13.74(0.05)	1.99(0.03)	6.93(0.10)	9.29(1.98)	1.52(0.37)	4.85(0.69)	2.86(0.44)
0.8	0.2	14.15(0.06)	2.04(0.03)	6.94(0.11)	9.89(1.89)	1.52(0.35)	4.95(0.73)	2.88(0.44)
0.8	0.3	14.55(0.08)	2.09(0.03)	6.95(0.10)	8.11(1.53)	1.81(0.32)	4.55(0.73)	3.18(0.44)
0.8	0.4	15.06(0.09)	2.15(0.03)	6.99(0.10)	9.34(1.58)	1.69(0.29)	4.58(0.93)	3.41(0.77)
0.8	0.5	15.26(0.08)	2.20(0.03)	6.92(0.11)	10.42(1.30)	1.51(0.19)	4.27(1.16)	3.56(0.87)
0.8	0.6	15.67(0.05)	2.28(0.02)	6.89(0.07)	10.08(2.06)	1.60(0.40)	5.19(1.01)	2.93(0.39)
0.8	0.7	15.94(0.04)	2.32(0.02)	6.89(0.07)	11.45(1.99)	1.47(0.29)	5.46(0.81)	3.03(0.39)
0.8	0.8	16.34(0.09)	2.37(0.03)	6.90(0.09)	10.86(1.85)	1.55(0.28)	5.36(1.09)	2.99(0.45)
0.8	0.9	16.33(0.06)	2.40(0.02)	6.80(0.07)	11.05(2.54)	1.54(0.32)	5.02(0.94)	3.48(0.85)
0.8	1.0	16.62(0.03)	2.46(0.02)	6.75(0.06)	9.98(1.18)	1.67(0.19)	5.58(1.08)	3.12(0.72)
1.0	0.1	11.26(0.05)	1.54(0.01)	7.30(0.07)	7.57(2.19)	1.57(0.47)	4.01(0.40)	2.87(0.30)
1.0	0.2	12.06(0.03)	1.63(0.04)	7.42(0.17)	8.14(1.18)	1.53(0.25)	4.42(0.94)	2.92(0.53)
1.0	0.3	12.87(0.04)	1.75(0.03)	7.38(0.12)	8.71(1.85)	1.55(0.32)	4.76(0.83)	2.79(0.70)
1.0	0.4	13.29(0.08)	1.82(0.02)	7.32(0.11)	9.14(2.15)	1.48(0.36)	4.59(0.92)	3.08(0.66)
1.0	0.5	14.06(0.05)	1.91(0.03)	7.37(0.11)	8.15(1.07)	1.77(0.25)	5.31(1.07)	2.74(0.63)
1.0	0.6	14.49(0.04)	2.00(0.02)	7.27(0.06)	9.61(2.25)	1.60(0.51)	5.38(0.96)	2.80(0.58)
1.0	0.7	14.94(0.05)	2.06(0.03)	7.26(0.09)	10.76(2.95)	1.39(0.34)	5.23(0.97)	2.99(0.66)
1.0	0.8	15.35(0.05)	2.12(0.02)	7.25(0.05)	9.76(1.34)	1.61(0.24)	5.61(0.68)	2.79(0.42)
1.0	0.9	15.71(0.05)	2.17(0.02)	7.23(0.05)	10.94(0.90)	1.44(0.12)	5.46(0.67)	2.92(0.40)
1.0	1.0	15.94(0.10)	2.25(0.03)	7.09(0.10)	9.68(2.07)	1.77(0.45)	5.32(1.11)	3.07(0.74)
1.2	0.1	9.72(0.10)	1.28(0.05)	7.60(0.24)	6.23(1.51)	1.69(0.67)	3.64(0.93)	2.88(1.00)
1.2	0.2	10.79(0.06)	1.37(0.02)	7.83(0.14)	6.58(1.54)	1.75(0.56)	4.20(0.72)	2.67(0.45)
1.2	0.3	11.48(0.04)	1.49(0.02)	7.70(0.10)	7.24(2.15)	1.72(0.55)	3.90(0.82)	3.10(0.82)
1.2	0.4	12.28(0.01)	1.60(0.02)	7.64(0.08)	8.64(0.87)	1.44(0.16)	3.96(1.02)	3.39(0.78)
1.2	0.5	12.86(0.04)	1.69(0.02)	7.64(0.11)	8.23(1.92)	1.62(0.44)	4.68(0.68)	2.85(0.48)
1.2	0.6	13.50(0.06)	1.79(0.02)	7.55(0.10)	8.41(1.74)	1.71(0.41)	4.62(1.43)	3.30(0.88)
1.2	0.7	13.99(0.09)	1.87(0.03)	7.49(0.16)	9.15(2.17)	1.66(0.45)	5.05(0.46)	2.79(0.27)
1.2	0.8	14.66(0.04)	1.94(0.03)	7.52(0.14)	10.52(1.64)	1.42(0.29)	5.32(0.72)	2.86(0.44)
1.2	0.9	15.05(0.06)	2.01(0.02)	7.49(0.06)	9.48(1.23)	1.64(0.20)	5.27(0.97)	3.03(0.52)
1.2	1.0	15.44(0.04)	2.06(0.03)	7.48(0.11)	9.33(1.92)	1.78(0.29)	5.01(0.95)	3.06(0.52)

Table 4.5: Results of NEMD simulations in the systems where $\Delta T_{Lang} = 1.0$ and $T_{\text{sink}} = 0.8$) showing the influence of L/S interaction parameters ε_{LS} and σ_{LS} on the structural properties including the contact density ρ_c, depletion layer thickness δ, and peak value S_{max} of the static in-plane structure factor [Eq. (1.10)], and the thermal properties including the contact layer temperature T_c, thermal jump ΔT and thermal slip length L_T [Eq. (1.2)]. Numbers in parentheses are standard deviation values. All values are reported in reduced units.

		Hotter interface						Colder interface					
σ_{LS}	ε_{LS}	ρ_c	δ	S_{max}	T_c	ΔT	L_T	ρ_c	δ	S_{max}	T_c	ΔT	L_T
0.8	0.1	0.922(0.018)	0.646(0.008)	0.139(0.001)	1.618(0.007)	0.176(0.007)	8.871(0.386)	0.995(0.019)	0.465(0.010)	0.507(0.008)	0.973(0.005)	0.147(0.007)	7.377(0.398)
0.8	0.2	1.021(0.009)	0.657(0.009)	0.147(0.002)	1.627(0.006)	0.165(0.005)	8.097(0.317)	1.263(0.015)	0.487(0.007)	0.473(0.003)	0.970(0.002)	0.141(0.006)	6.908(0.378)
0.8	0.3	1.075(0.029)	0.665(0.008)	0.156(0.002)	1.629(0.008)	0.166(0.007)	7.926(0.419)	1.474(0.031)	0.468(0.000)	0.539(0.004)	0.955(0.005)	0.124(0.006)	5.933(0.355)
0.8	0.4	1.116(0.013)	0.666(0.008)	0.171(0.001)	1.634(0.007)	0.157(0.010)	7.313(0.556)	1.774(0.031)	0.452(0.000)	0.631(0.006)	0.943(0.003)	0.111(0.004)	5.142(0.225)
0.8	0.5	1.153(0.011)	0.655(0.000)	0.190(0.002)	1.641(0.006)	0.152(0.008)	6.901(0.419)	2.113(0.028)	0.452(0.000)	0.720(0.004)	0.931(0.003)	0.098(0.003)	4.469(0.159)
0.8	0.6	1.195(0.018)	0.643(0.007)	0.209(0.002)	1.657(0.004)	0.141(0.008)	6.194(0.393)	2.492(0.039)	0.437(0.000)	0.796(0.003)	0.920(0.004)	0.087(0.005)	3.816(0.238)
0.8	0.7	1.217(0.014)	0.638(0.005)	0.238(0.003)	1.664(0.004)	0.130(0.009)	5.628(0.418)	2.845(0.048)	0.437(0.000)	0.842(0.003)	0.915(0.002)	0.080(0.004)	3.467(0.176)
0.8	0.8	1.245(0.032)	0.629(0.008)	0.261(0.002)	1.673(0.004)	0.123(0.010)	5.193(0.494)	3.134(0.044)	0.435(0.005)	0.870(0.002)	0.907(0.003)	0.073(0.004)	3.073(0.155)
0.8	0.9	1.293(0.026)	0.622(0.005)	0.295(0.002)	1.680(0.006)	0.118(0.005)	4.920(0.222)	3.383(0.049)	0.431(0.008)	0.887(0.001)	0.901(0.003)	0.067(0.005)	2.773(0.216)
0.8	1.0	1.340(0.019)	0.608(0.000)	0.325(0.003)	1.691(0.004)	0.106(0.006)	4.310(0.269)	3.589(0.027)	0.431(0.008)	0.899(0.001)	0.895(0.003)	0.060(0.003)	2.420(0.153)
1.0	0.1	1.292(0.036)	0.847(0.008)	0.073(0.001)	1.562(0.004)	0.217(0.005)	14.052(0.425)	1.641(0.029)	0.811(0.000)	0.142(0.002)	1.088(0.004)	0.260(0.006)	16.845(0.382)
1.0	0.2	1.381(0.022)	0.883(0.008)	0.081(0.001)	1.570(0.009)	0.207(0.008)	12.722(0.765)	1.822(0.009)	0.842(0.000)	0.174(0.002)	1.068(0.003)	0.239(0.006)	14.655(0.643)
1.0	0.3	1.456(0.021)	0.891(0.005)	0.092(0.001)	1.582(0.007)	0.190(0.009)	10.903(0.616)	1.994(0.026)	0.842(0.000)	0.222(0.003)	1.053(0.005)	0.216(0.005)	12.359(0.406)
1.0	0.4	1.536(0.025)	0.891(0.005)	0.106(0.001)	1.590(0.009)	0.188(0.009)	10.339(0.561)	2.160(0.026)	0.838(0.008)	0.281(0.003)	1.031(0.004)	0.195(0.005)	10.743(0.356)
1.0	0.5	1.596(0.024)	0.892(0.007)	0.119(0.001)	1.603(0.006)	0.176(0.008)	9.226(0.525)	2.386(0.037)	0.827(0.000)	0.356(0.006)	1.015(0.005)	0.178(0.007)	9.308(0.459)
1.0	0.6	1.646(0.034)	0.903(0.005)	0.135(0.001)	1.614(0.004)	0.163(0.004)	8.145(0.243)	2.630(0.041)	0.827(0.000)	0.453(0.005)	0.998(0.004)	0.161(0.004)	8.053(0.257)
1.0	0.7	1.716(0.035)	0.900(0.008)	0.152(0.002)	1.625(0.008)	0.154(0.007)	7.484(0.428)	3.016(0.051)	0.811(0.000)	0.561(0.005)	0.984(0.003)	0.146(0.005)	7.061(0.323)
1.0	0.8	1.770(0.017)	0.889(0.000)	0.171(0.001)	1.635(0.006)	0.149(0.005)	7.037(0.306)	3.390(0.030)	0.811(0.000)	0.670(0.004)	0.972(0.003)	0.132(0.003)	6.220(0.157)
1.0	0.9	1.862(0.029)	0.889(0.000)	0.192(0.001)	1.637(0.008)	0.140(0.009)	6.443(0.452)	3.759(0.052)	0.805(0.008)	0.746(0.004)	0.963(0.005)	0.123(0.005)	5.641(0.185)
1.0	1.0	1.933(0.023)	0.889(0.000)	0.214(0.002)	1.651(0.007)	0.131(0.007)	5.836(0.356)	4.079(0.053)	0.797(0.005)	0.795(0.002)	0.951(0.002)	0.110(0.004)	4.894(0.225)
1.2	0.1	1.439(0.027)	1.045(0.000)	0.048(0.001)	1.527(0.011)	0.250(0.012)	19.648(1.642)	1.797(0.030)	1.022(0.008)	0.076(0.001)	1.145(0.004)	0.316(0.006)	24.821(1.281)
1.2	0.2	1.574(0.019)	1.078(0.005)	0.054(0.001)	1.537(0.006)	0.237(0.007)	17.257(0.792)	1.991(0.022)	1.062(0.005)	0.094(0.002)	1.126(0.005)	0.297(0.004)	21.613(0.574)
1.2	0.3	1.672(0.024)	1.100(0.008)	0.062(0.001)	1.549(0.007)	0.224(0.007)	14.973(0.574)	2.170(0.030)	1.076(0.000)	0.118(0.002)	1.102(0.004)	0.271(0.005)	18.148(0.413)
1.2	0.4	1.754(0.035)	1.108(0.000)	0.070(0.001)	1.565(0.007)	0.205(0.008)	12.768(0.625)	2.339(0.040)	1.086(0.008)	0.149(0.002)	1.087(0.003)	0.252(0.005)	15.680(0.409)
1.2	0.5	1.851(0.017)	1.123(0.000)	0.080(0.001)	1.573(0.008)	0.200(0.006)	11.857(0.512)	2.544(0.031)	1.092(0.000)	0.189(0.003)	1.065(0.003)	0.229(0.004)	13.582(0.350)
1.2	0.6	1.913(0.030)	1.123(0.000)	0.090(0.001)	1.585(0.005)	0.187(0.007)	10.485(0.459)	2.777(0.035)	1.092(0.000)	0.238(0.003)	1.050(0.004)	0.210(0.006)	11.726(0.404)
1.2	0.7	2.021(0.033)	1.125(0.005)	0.104(0.001)	1.592(0.004)	0.176(0.005)	9.431(0.365)	2.983(0.035)	1.090(0.005)	0.302(0.005)	1.035(0.005)	0.194(0.007)	10.426(0.510)
1.2	0.8	2.078(0.024)	1.126(0.007)	0.114(0.002)	1.610(0.007)	0.161(0.008)	8.291(0.506)	3.215(0.033)	1.086(0.008)	0.375(0.007)	1.025(0.004)	0.180(0.005)	9.249(0.388)
1.2	0.9	2.172(0.026)	1.123(0.000)	0.131(0.002)	1.613(0.007)	0.159(0.004)	7.904(0.248)	3.534(0.034)	1.076(0.000)	0.475(0.006)	1.008(0.004)	0.165(0.006)	8.210(0.367)
1.2	1.0	2.259(0.031)	1.123(0.000)	0.142(0.001)	1.624(0.007)	0.150(0.007)	7.269(0.438)	3.824(0.047)	1.076(0.000)	0.577(0.008)	0.999(0.004)	0.156(0.005)	7.547(0.365)

Table 4.6: Peak frequencies ν_L^* and ν_S^* in the contact layer and first solid layer, respectively, and the ratio ν_S^*/ν_L^* obtained using different values of σ_{LS} and ε_{LS} in the systems where $\Delta T_{Lang} = 1.0$ ($T_{\text{source}} = 1.8$ and $T_{\text{sink}} = 0.8$). Numbers in parentheses are standard deviation values. All values are reported in reduced units.

		Hotter interface			Colder interface		
σ_{LS}	ε_{LS}	ν_L^*	ν_S^*	ν_S^*/ν_L^*	ν_L^*	ν_S^*	ν_S^*/ν_L^*
0.8	0.1	2.453(0.021)	4.843(0.006)	1.974(0.015)	2.377(0.006)	5.070(0.000)	2.133(0.005)
0.8	0.2	1.703(1.132)	4.873(0.012)	3.632(1.742)	1.563(0.055)	5.120(0.000)	3.278(0.115)
0.8	0.3	1.123(0.012)	4.900(0.000)	4.362(0.045)	1.660(0.062)	5.147(0.006)	3.103(0.118)
0.8	0.4	1.150(0.017)	4.913(0.006)	4.273(0.066)	1.740(0.017)	5.183(0.006)	2.979(0.026)
0.8	0.5	1.200(0.010)	4.920(0.000)	4.100(0.034)	1.857(0.015)	5.227(0.012)	2.815(0.023)
0.8	0.6	1.243(0.021)	4.937(0.006)	3.971(0.068)	1.947(0.012)	5.260(0.000)	2.702(0.016)
0.8	0.7	1.337(0.021)	4.950(0.010)	3.704(0.060)	2.037(0.012)	5.300(0.000)	2.602(0.015)
0.8	0.8	1.390(0.026)	4.967(0.006)	3.574(0.066)	2.150(0.010)	5.343(0.012)	2.485(0.013)
0.8	0.9	1.443(0.055)	4.987(0.006)	3.458(0.137)	2.230(0.010)	5.387(0.006)	2.416(0.013)
0.8	1.0	1.503(0.031)	5.007(0.012)	3.331(0.076)	2.330(0.010)	5.427(0.006)	2.329(0.008)
1.0	0.1	1.073(0.006)	4.923(0.006)	4.587(0.019)	1.317(0.032)	5.150(0.000)	3.913(0.097)
1.0	0.2	1.133(0.029)	4.950(0.000)	4.370(0.113)	1.437(0.006)	5.173(0.006)	3.601(0.013)
1.0	0.3	1.177(0.031)	4.963(0.006)	4.220(0.104)	1.527(0.060)	5.203(0.006)	3.412(0.137)
1.0	0.4	1.230(0.020)	4.983(0.006)	4.052(0.066)	1.583(0.025)	5.243(0.006)	3.312(0.049)
1.0	0.5	1.300(0.030)	5.007(0.006)	3.853(0.093)	1.700(0.040)	5.283(0.006)	3.109(0.070)
1.0	0.6	1.360(0.090)	5.030(0.010)	3.709(0.239)	1.877(0.064)	5.327(0.012)	2.840(0.088)
1.0	0.7	1.350(0.026)	5.050(0.010)	3.742(0.067)	1.990(0.061)	5.377(0.006)	2.704(0.085)
1.0	0.8	1.403(0.032)	5.083(0.006)	3.624(0.078)	2.160(0.020)	5.430(0.017)	2.514(0.017)
1.0	0.9	1.450(0.026)	5.100(0.017)	3.518(0.053)	2.313(0.023)	5.503(0.006)	2.379(0.025)
1.0	1.0	1.527(0.038)	5.147(0.025)	3.372(0.072)	2.433(0.006)	5.560(0.000)	2.285(0.005)
1.2	0.1	1.120(0.017)	4.960(0.000)	4.429(0.068)	1.347(0.025)	5.170(0.000)	3.840(0.072)
1.2	0.2	1.183(0.021)	4.980(0.000)	4.209(0.075)	1.410(0.017)	5.197(0.012)	3.686(0.042)
1.2	0.3	1.240(0.035)	5.010(0.010)	4.043(0.122)	1.487(0.031)	5.237(0.012)	3.523(0.074)
1.2	0.4	1.330(0.040)	5.047(0.006)	3.797(0.114)	1.633(0.021)	5.267(0.015)	3.225(0.032)
1.2	0.5	1.393(0.032)	5.070(0.010)	3.640(0.082)	1.670(0.010)	5.323(0.012)	3.188(0.014)
1.2	0.6	1.397(0.076)	5.110(0.010)	3.666(0.211)	1.800(0.017)	5.360(0.000)	2.978(0.029)
1.2	0.7	1.500(0.046)	5.143(0.012)	3.431(0.098)	1.897(0.006)	5.427(0.006)	2.861(0.006)
1.2	0.8	1.523(0.045)	5.183(0.012)	3.405(0.107)	2.053(0.025)	5.480(0.010)	2.669(0.031)
1.2	0.9	1.573(0.012)	5.227(0.006)	3.322(0.021)	2.213(0.021)	5.523(0.006)	2.496(0.026)
1.2	1.0	1.627(0.035)	5.283(0.012)	3.249(0.076)	2.363(0.012)	5.567(0.012)	2.355(0.016)

Table 4.7: Results of NEMD simulations in the systems where $\Delta T_{Lang} = 0.6$ ($T_{\text{source}} = 1.6$ and $T_{\text{sink}} = 1.0$ showing the influence of L/S interaction parameters ε_{LS} and σ_{LS} on the bulk thermal properties including the thermal flux J_z [Eq. (1.8)], magnitude of the thermal gradient $|dT/dz|$, and thermal conductivity k [Eq. (1.3)] within the bulk solid and liquid away from the L/S interface. The numerical values in each column are to be multiplied by the multiplicative factor appearing in the column heading. Thermal gradient values were extracted from least squares fits across the linear portion of the thermal profile within each region. Numbers in parentheses are standard deviation values. All values are reported in reduced units.

			Liquid		Hotter solid		Colder solid	
σ_{LS}	ε_{LS}	$J_z \times 10^{-2}$	$\lvert dT/dz\rvert \times 10^{-2}$	k	$\lvert dT/dz\rvert \times 10^{-4}$	$k \times 10^{2}$	$\lvert dT/dz\rvert \times 10^{-4}$	$k \times 10^{2}$
0.8	0.1	8.35(0.05)	1.21(0.03)	6.92(0.14)	4.74(1.61)	1.86(0.66)	3.44(0.85)	2.52(0.62)
0.8	0.2	8.59(0.03)	1.24(0.02)	6.91(0.11)	4.52(1.12)	2.13(0.80)	3.14(0.86)	3.09(1.43)
0.8	0.3	8.84(0.03)	1.27(0.03)	7.01(0.17)	5.56(1.28)	1.58(0.32)	3.89(1.65)	2.29(0.86)
0.8	0.4	9.12(0.02)	1.32(0.02)	6.94(0.12)	5.66(1.66)	1.79(0.60)	3.81(1.04)	2.55(0.85)
0.8	0.5	9.55(0.02)	1.35(0.03)	7.12(0.12)	6.03(1.78)	1.73(0.49)	4.05(1.26)	2.50(1.15)
0.8	0.6	9.54(0.06)	1.38(0.02)	6.89(0.13)	5.44(1.41)	1.93(0.65)	3.62(0.88)	2.83(0.68)
0.8	0.7	9.76(0.03)	1.40(0.03)	6.97(0.16)	5.11(2.42)	2.48(1.96)	4.11(1.10)	2.48(0.75)
0.8	0.8	9.96(0.03)	1.44(0.02)	6.95(0.10)	6.26(1.92)	1.68(0.48)	4.27(0.77)	2.44(0.50)
0.8	0.9	10.02(0.08)	1.47(0.02)	6.81(0.11)	5.51(1.37)	1.84(0.41)	3.84(1.30)	3.04(1.06)
0.8	1.0	10.02(0.04)	1.48(0.02)	6.77(0.11)	5.95(1.94)	1.98(0.72)	4.53(1.38)	2.67(1.53)
1.0	0.1	6.91(0.08)	0.94(0.03)	7.38(0.24)	4.54(1.58)	1.89(1.00)	2.87(0.97)	2.49(0.94)
1.0	0.2	7.19(0.03)	0.99(0.02)	7.29(0.16)	4.68(1.81)	1.95(1.05)	3.20(0.84)	2.44(0.53)
1.0	0.3	7.84(0.03)	1.05(0.04)	7.46(0.30)	4.41(2.15)	2.14(1.15)	3.58(1.10)	2.27(0.71)
1.0	0.4	8.14(0.02)	1.10(0.03)	7.39(0.18)	4.92(1.97)	1.83(0.73)	3.48(1.66)	2.56(1.33)
1.0	0.5	8.60(0.03)	1.17(0.03)	7.35(0.19)	4.31(1.15)	2.14(0.65)	3.42(0.67)	2.61(0.54)
1.0	0.6	8.82(0.05)	1.22(0.03)	7.27(0.19)	4.87(2.04)	2.38(1.47)	3.27(1.34)	2.77(1.10)
1.0	0.7	9.21(0.07)	1.27(0.03)	7.28(0.25)	5.22(1.69)	2.06(0.76)	3.60(1.33)	2.74(1.18)
1.0	0.8	9.34(0.07)	1.29(0.03)	7.24(0.15)	5.21(1.59)	1.92(0.94)	3.32(1.08)	2.84(0.85)
1.0	0.9	9.62(0.05)	1.33(0.02)	7.25(0.13)	5.64(1.25)	1.75(0.36)	3.95(0.92)	2.51(0.78)
1.0	1.0	9.84(0.05)	1.35(0.03)	7.26(0.15)	6.11(1.64)	1.66(0.43)	3.85(1.34)	3.01(1.62)
1.2	0.1	5.84(0.04)	0.77(0.03)	7.60(0.29)	4.07(1.56)	1.90(1.29)	2.32(0.80)	2.65(0.94)
1.2	0.2	6.53(0.05)	0.83(0.04)	7.88(0.35)	4.06(1.70)	2.14(1.49)	3.06(0.89)	2.19(0.61)
1.2	0.3	6.94(0.09)	0.90(0.03)	7.69(0.25)	3.89(1.16)	2.01(0.98)	2.45(0.92)	3.23(1.09)
1.2	0.4	7.33(0.02)	0.97(0.03)	7.56(0.23)	4.15(2.09)	2.19(1.24)	3.61(0.90)	2.13(0.65)
1.2	0.5	7.79(0.02)	1.02(0.02)	7.67(0.15)	4.56(1.34)	1.86(0.84)	3.60(1.16)	2.49(1.15)
1.2	0.6	8.15(0.03)	1.08(0.02)	7.53(0.14)	5.45(1.94)	2.03(1.72)	3.25(1.65)	3.35(1.48)
1.2	0.7	8.53(0.03)	1.11(0.02)	7.69(0.17)	5.46(1.82)	1.74(0.60)	3.31(0.99)	2.93(0.86)
1.2	0.8	8.81(0.10)	1.17(0.03)	7.53(0.23)	5.30(1.91)	1.87(0.75)	3.59(1.27)	3.43(3.27)
1.2	0.9	9.18(0.05)	1.21(0.02)	7.61(0.15)	6.13(1.17)	1.57(0.37)	3.23(0.61)	2.74(0.34)
1.2	1.0	9.18(0.04)	1.26(0.02)	7.31(0.11)	5.82(1.39)	1.66(0.38)	3.70(0.74)	2.61(0.60)

Table 4.8: Results of NEMD simulations in the systems where $\Delta T_{Lang} = 0.6$ ($T_{\text{source}} = 1.6$ and $T_{\text{sink}} = 1.0$) showing the influence of L/S interaction parameters ε_{LS} and σ_{LS} on the structural properties including the contact density ρ_c, depletion layer thickness δ, and peak value S_{max} of the static in-plane structure factor [Eq. (1.10)], and the thermal properties including the contact layer temperature T_c, thermal jump ΔT and thermal slip length L_T [Eq. (1.2)]. Numbers in parentheses are standard deviation values. All values are reported in reduced units.

		Hotter interface						Colder interface					
σ_{LS}	ε_{LS}	ρ_c	δ	S_{max}	T_c	ΔT	L_T	ρ_c	δ	S_{max}	T_c	ΔT	L_T
0.8	0.1	0.946(0.029)	0.624(0.007)	0.166(0.002)	1.493(0.003)	0.100(0.007)	8.330(0.739)	0.993(0.020)	0.512(0.010)	0.400(0.007)	1.101(0.004)	0.090(0.004)	7.440(0.354)
0.8	0.2	1.066(0.025)	0.629(0.008)	0.178(0.002)	1.500(0.005)	0.093(0.004)	7.472(0.430)	1.198(0.030)	0.546(0.000)	0.365(0.002)	1.102(0.003)	0.086(0.003)	6.928(0.317)
0.8	0.3	1.129(0.017)	0.640(0.000)	0.195(0.002)	1.500(0.005)	0.092(0.009)	7.268(0.833)	1.300(0.024)	0.537(0.008)	0.409(0.002)	1.095(0.003)	0.077(0.004)	6.075(0.427)
0.8	0.4	1.168(0.018)	0.632(0.008)	0.216(0.002)	1.507(0.007)	0.082(0.006)	6.221(0.558)	1.444(0.029)	0.513(0.005)	0.474(0.004)	1.089(0.004)	0.070(0.005)	5.332(0.393)
0.8	0.5	1.224(0.015)	0.627(0.007)	0.247(0.003)	1.514(0.007)	0.076(0.006)	5.679(0.556)	1.615(0.022)	0.493(0.008)	0.555(0.003)	1.082(0.005)	0.065(0.006)	4.800(0.476)
0.8	0.6	1.258(0.014)	0.616(0.008)	0.276(0.002)	1.518(0.007)	0.074(0.004)	5.334(0.373)	1.844(0.027)	0.484(0.000)	0.629(0.005)	1.075(0.004)	0.056(0.005)	4.049(0.379)
0.8	0.7	1.312(0.017)	0.607(0.005)	0.308(0.002)	1.520(0.006)	0.072(0.008)	5.125(0.659)	2.083(0.025)	0.468(0.000)	0.699(0.003)	1.071(0.003)	0.052(0.004)	3.685(0.330)
0.8	0.8	1.349(0.016)	0.593(0.000)	0.345(0.004)	1.531(0.006)	0.063(0.006)	4.380(0.479)	2.339(0.031)	0.468(0.000)	0.759(0.003)	1.066(0.004)	0.048(0.005)	3.337(0.393)
0.8	0.9	1.415(0.032)	0.576(0.005)	0.386(0.004)	1.534(0.004)	0.058(0.006)	3.974(0.463)	2.581(0.037)	0.456(0.007)	0.803(0.002)	1.060(0.004)	0.043(0.006)	2.939(0.407)
0.8	1.0	1.479(0.018)	0.560(0.005)	0.425(0.002)	1.537(0.005)	0.058(0.006)	3.932(0.473)	2.792(0.042)	0.443(0.008)	0.832(0.001)	1.057(0.003)	0.038(0.005)	2.546(0.332)
1.0	0.1	1.350(0.027)	0.841(0.005)	0.082(0.002)	1.454(0.008)	0.131(0.010)	13.930(1.421)	1.552(0.025)	0.813(0.005)	0.120(0.001)	1.171(0.005)	0.149(0.007)	15.911(1.003)
1.0	0.2	1.462(0.021)	0.872(0.005)	0.093(0.001)	1.458(0.007)	0.128(0.008)	12.975(1.070)	1.710(0.033)	0.842(0.000)	0.147(0.002)	1.157(0.004)	0.137(0.006)	13.913(0.698)
1.0	0.3	1.550(0.022)	0.889(0.000)	0.107(0.001)	1.471(0.008)	0.118(0.008)	11.241(1.139)	1.872(0.020)	0.849(0.008)	0.180(0.003)	1.148(0.007)	0.126(0.007)	12.070(1.085)
1.0	0.4	1.623(0.020)	0.889(0.000)	0.124(0.001)	1.474(0.007)	0.107(0.007)	9.701(0.797)	1.995(0.023)	0.858(0.000)	0.220(0.002)	1.139(0.003)	0.118(0.005)	10.652(0.653)
1.0	0.5	1.716(0.020)	0.886(0.007)	0.143(0.002)	1.483(0.007)	0.100(0.007)	8.588(0.805)	2.139(0.037)	0.852(0.008)	0.273(0.003)	1.127(0.007)	0.105(0.008)	8.992(0.855)
1.0	0.6	1.794(0.015)	0.881(0.008)	0.165(0.003)	1.492(0.005)	0.093(0.008)	7.688(0.823)	2.303(0.050)	0.842(0.000)	0.329(0.006)	1.118(0.004)	0.095(0.006)	7.819(0.580)
1.0	0.7	1.869(0.035)	0.878(0.008)	0.189(0.003)	1.498(0.006)	0.087(0.008)	6.893(0.780)	2.505(0.023)	0.839(0.007)	0.402(0.003)	1.110(0.004)	0.085(0.006)	6.718(0.566)
1.0	0.8	1.954(0.027)	0.875(0.005)	0.215(0.002)	1.498(0.007)	0.085(0.005)	6.596(0.536)	2.721(0.037)	0.833(0.008)	0.479(0.004)	1.102(0.004)	0.078(0.005)	6.067(0.515)
1.0	0.9	2.025(0.030)	0.875(0.005)	0.242(0.002)	1.504(0.006)	0.080(0.008)	6.017(0.666)	2.989(0.033)	0.816(0.008)	0.562(0.005)	1.095(0.005)	0.071(0.007)	5.361(0.568)
1.0	1.0	2.112(0.025)	0.874(0.000)	0.270(0.002)	1.515(0.008)	0.075(0.005)	5.536(0.476)	3.279(0.031)	0.811(0.000)	0.640(0.007)	1.089(0.007)	0.069(0.008)	5.122(0.681)
1.2	0.1	1.514(0.017)	1.045(0.000)	0.051(0.001)	1.431(0.006)	0.156(0.007)	20.334(1.460)	1.701(0.020)	1.039(0.008)	0.069(0.001)	1.197(0.003)	0.183(0.003)	23.918(1.048)
1.2	0.2	1.637(0.029)	1.076(0.000)	0.059(0.001)	1.436(0.008)	0.148(0.008)	17.882(1.652)	1.897(0.035)	1.073(0.007)	0.084(0.001)	1.188(0.007)	0.170(0.006)	20.539(1.536)
1.2	0.3	1.752(0.034)	1.094(0.005)	0.069(0.001)	1.443(0.006)	0.141(0.009)	15.586(1.435)	2.077(0.021)	1.081(0.008)	0.103(0.002)	1.176(0.005)	0.154(0.003)	17.080(0.793)
1.2	0.4	1.856(0.024)	1.108(0.000)	0.080(0.001)	1.457(0.005)	0.125(0.004)	12.851(0.638)	2.208(0.016)	1.092(0.000)	0.126(0.002)	1.167(0.005)	0.147(0.006)	15.092(0.962)
1.2	0.5	1.968(0.024)	1.109(0.005)	0.093(0.001)	1.465(0.008)	0.120(0.006)	11.744(0.748)	2.390(0.045)	1.092(0.000)	0.157(0.003)	1.155(0.005)	0.135(0.002)	13.289(0.417)
1.2	0.6	2.031(0.027)	1.119(0.008)	0.105(0.001)	1.471(0.009)	0.111(0.009)	10.240(0.916)	2.541(0.026)	1.092(0.000)	0.188(0.003)	1.148(0.007)	0.123(0.008)	11.407(0.862)
1.2	0.7	2.149(0.039)	1.123(0.000)	0.121(0.002)	1.473(0.007)	0.109(0.004)	9.831(0.520)	2.717(0.040)	1.092(0.000)	0.227(0.003)	1.136(0.004)	0.117(0.006)	10.540(0.727)
1.2	0.8	2.251(0.019)	1.123(0.000)	0.139(0.001)	1.481(0.007)	0.100(0.007)	8.606(0.805)	2.863(0.032)	1.092(0.000)	0.273(0.003)	1.129(0.004)	0.105(0.006)	9.010(0.705)
1.2	0.9	2.346(0.022)	1.123(0.000)	0.158(0.001)	1.487(0.006)	0.091(0.006)	7.497(0.548)	3.046(0.020)	1.092(0.000)	0.329(0.004)	1.124(0.004)	0.100(0.006)	8.324(0.626)
1.2	1.0	2.439(0.035)	1.115(0.008)	0.177(0.002)	1.495(0.005)	0.086(0.005)	6.835(0.422)	3.300(0.054)	1.092(0.000)	0.394(0.004)	1.113(0.005)	0.090(0.005)	7.183(0.459)

Table 4.9: Peak frequencies ν_L^* and ν_S^* in the contact layer and first solid layer, respectively, and the ratio ν_S^*/ν_L^* obtained using different values of σ_{LS} and ε_{LS} in the systems where $\Delta T_{Lang} = 0.6$ ($T_{\text{source}} = 1.6$ and $T_{\text{sink}} = 1.0$). Numbers in parentheses are standard deviation values. All values are reported in reduced units.

		Hotter interface			Colder interface		
σ_{LS}	ε_{LS}	ν_L^*	ν_S^*	ν_S^*/ν_L^*	ν_L^*	ν_S^*	ν_S^*/ν_L^*
0.8	0.1	2.407(0.012)	4.903(0.006)	2.037(0.007)	2.383(0.006)	5.047(0.006)	2.117(0.004)
0.8	0.2	1.170(0.036)	4.947(0.006)	4.230(0.125)	1.483(0.038)	5.080(0.000)	3.426(0.089)
0.8	0.3	1.207(0.006)	4.963(0.006)	4.113(0.018)	1.547(0.025)	5.110(0.010)	3.304(0.057)
0.8	0.4	1.280(0.036)	4.980(0.000)	3.893(0.111)	1.617(0.038)	5.137(0.006)	3.178(0.072)
0.8	0.5	1.330(0.035)	4.997(0.006)	3.759(0.102)	1.697(0.038)	5.170(0.000)	3.048(0.067)
0.8	0.6	1.403(0.029)	5.010(0.000)	3.571(0.074)	1.733(0.031)	5.200(0.000)	3.001(0.053)
0.8	0.7	1.453(0.067)	5.023(0.012)	3.461(0.162)	1.833(0.021)	5.237(0.006)	2.857(0.030)
0.8	0.8	1.490(0.010)	5.047(0.006)	3.387(0.019)	1.957(0.023)	5.283(0.006)	2.700(0.031)
0.8	0.9	1.563(0.049)	5.067(0.015)	3.243(0.100)	2.070(0.017)	5.320(0.000)	2.570(0.022)
0.8	1.0	1.643(0.070)	5.090(0.000)	3.101(0.133)	2.120(0.010)	5.353(0.006)	2.525(0.012)
1.0	0.1	1.137(0.051)	4.970(0.010)	4.379(0.208)	1.307(0.032)	5.113(0.006)	3.915(0.096)
1.0	0.2	1.193(0.025)	5.003(0.006)	4.194(0.089)	1.407(0.023)	5.147(0.006)	3.659(0.057)
1.0	0.3	1.230(0.026)	5.020(0.010)	4.083(0.097)	1.467(0.087)	5.167(0.006)	3.531(0.211)
1.0	0.4	1.310(0.020)	5.047(0.006)	3.853(0.055)	1.500(0.053)	5.200(0.000)	3.469(0.120)
1.0	0.5	1.370(0.000)	5.073(0.006)	3.703(0.004)	1.570(0.040)	5.243(0.006)	3.341(0.085)
1.0	0.6	1.377(0.021)	5.103(0.006)	3.708(0.059)	1.633(0.042)	5.277(0.012)	3.232(0.087)
1.0	0.7	1.463(0.101)	5.127(0.012)	3.514(0.238)	1.803(0.067)	5.323(0.006)	2.955(0.108)
1.0	0.8	1.523(0.025)	5.157(0.006)	3.386(0.053)	1.890(0.053)	5.383(0.006)	2.850(0.081)
1.0	0.9	1.607(0.049)	5.197(0.015)	3.236(0.092)	2.020(0.030)	5.437(0.006)	2.692(0.040)
1.0	1.0	1.633(0.032)	5.237(0.006)	3.207(0.061)	2.173(0.040)	5.510(0.000)	2.536(0.047)
1.2	0.1	1.160(0.062)	5.007(0.015)	4.324(0.216)	1.287(0.032)	5.130(0.000)	3.989(0.101)
1.2	0.2	1.247(0.021)	5.037(0.006)	4.041(0.064)	1.350(0.085)	5.170(0.000)	3.840(0.241)
1.2	0.3	1.303(0.047)	5.067(0.006)	3.891(0.145)	1.463(0.032)	5.200(0.000)	3.555(0.077)
1.2	0.4	1.340(0.036)	5.100(0.000)	3.808(0.104)	1.523(0.032)	5.250(0.010)	3.447(0.071)
1.2	0.5	1.440(0.017)	5.130(0.000)	3.563(0.043)	1.577(0.015)	5.287(0.015)	3.353(0.023)
1.2	0.6	1.477(0.006)	5.173(0.006)	3.503(0.012)	1.697(0.040)	5.333(0.015)	3.145(0.080)
1.2	0.7	1.530(0.026)	5.213(0.015)	3.408(0.059)	1.760(0.036)	5.387(0.006)	3.061(0.065)
1.2	0.8	1.587(0.065)	5.267(0.012)	3.323(0.131)	1.883(0.012)	5.443(0.012)	2.890(0.022)
1.2	0.9	1.647(0.071)	5.317(0.006)	3.233(0.138)	1.980(0.035)	5.493(0.015)	2.775(0.048)
1.2	1.0	1.683(0.029)	5.350(0.010)	3.179(0.055)	2.090(0.035)	5.543(0.015)	2.653(0.046)

Table 4.10: Results of NEMD simulations in the systems where $\Delta T_{Lang} = 0.2$ ($T_{\text{source}} = 1.4$ and $T_{\text{sink}} = 1.2$ showing the influence of L/S interaction parameters ε_{LS} and σ_{LS} on the bulk thermal properties including the thermal flux J_z [Eq. (1.8)], magnitude of the thermal gradient $|dT/dz|$, and thermal conductivity k [Eq. (1.3)] within the bulk solid and liquid away from the L/S interface. The numerical values in each column are to be multiplied by the multiplicative factor appearing in the column heading. Thermal gradient values were extracted from least squares fits across the linear portion of the thermal profile within each region. Numbers in parentheses are standard deviation values. All values are reported in reduced units.

			Liquid		Hotter solid		Colder solid	
σ_{LS}	ε_{LS}	$J_z \times 10^{-2}$	$\lvert dT/dz\rvert \times 10^{-2}$	k	$\lvert dT/dz\rvert \times 10^{-4}$	$k \times 10^{2}$	$\lvert dT/dz\rvert \times 10^{-4}$	$k \times 10^{2}$
0.8	0.1	2.67(0.04)	0.41(0.03)	6.64(0.55)	2.24(1.07)	1.55(0.80)	1.08(0.91)	7.54(8.04)
0.8	0.2	2.89(0.06)	0.42(0.02)	6.93(0.36)	1.46(0.86)	2.49(1.70)	0.99(1.01)	8.58(10.23)
0.8	0.3	2.92(0.04)	0.41(0.04)	7.23(0.59)	1.92(1.50)	3.20(3.41)	1.55(1.30)	4.01(4.66)
0.8	0.4	3.08(0.04)	0.44(0.02)	7.02(0.41)	2.13(1.29)	2.31(2.18)	1.77(1.09)	15.50(40.90)
0.8	0.5	3.18(0.04)	0.47(0.02)	6.84(0.31)	2.26(1.03)	1.86(1.32)	1.18(0.69)	4.68(4.26)
0.8	0.6	3.32(0.03)	0.48(0.02)	6.88(0.29)	2.11(1.10)	3.52(4.71)	1.30(0.92)	14.13(30.41)
0.8	0.7	3.28(0.03)	0.49(0.02)	6.73(0.22)	1.36(1.60)	6.64(6.66)	0.99(0.99)	9.77(11.11)
0.8	0.8	3.26(0.06)	0.47(0.03)	7.03(0.50)	1.92(1.44)	3.26(4.03)	1.68(1.25)	5.31(7.72)
0.8	0.9	3.47(0.03)	0.49(0.02)	7.08(0.27)	1.54(0.77)	3.35(2.41)	1.59(1.33)	18.50(40.33)
0.8	1.0	3.42(0.07)	0.49(0.02)	6.93(0.34)	2.06(1.19)	2.47(1.53)	1.85(1.10)	5.23(7.45)
1.0	0.1	2.23(0.02)	0.30(0.03)	7.73(0.72)	1.76(1.13)	3.86(6.72)	1.89(1.18)	2.53(3.85)
1.0	0.2	2.45(0.03)	0.31(0.04)	7.88(0.95)	2.33(1.79)	9.41(22.71)	0.83(0.52)	4.52(2.78)
1.0	0.3	2.66(0.04)	0.35(0.04)	7.87(0.74)	1.56(1.15)	8.15(14.80)	1.84(1.34)	2.11(1.37)
1.0	0.4	2.84(0.07)	0.37(0.03)	7.63(0.49)	1.97(1.63)	6.16(10.34)	1.10(0.81)	5.83(6.36)
1.0	0.5	2.84(0.04)	0.39(0.03)	7.34(0.61)	1.72(1.23)	3.63(4.71)	1.82(1.38)	7.43(14.99)
1.0	0.6	2.82(0.04)	0.41(0.04)	6.93(0.59)	2.30(1.18)	1.63(0.71)	1.98(1.21)	2.69(3.40)
1.0	0.7	2.93(0.03)	0.43(0.03)	6.92(0.39)	1.90(1.17)	4.21(5.75)	1.57(1.33)	10.83(18.10)
1.0	0.8	3.10(0.04)	0.43(0.04)	7.25(0.65)	1.88(0.93)	2.56(1.98)	1.72(1.00)	6.66(14.53)
1.0	0.9	3.28(0.02)	0.46(0.02)	7.23(0.31)	2.13(1.37)	3.60(4.59)	1.04(0.99)	5.39(3.76)
1.0	1.0	3.38(0.02)	0.46(0.02)	7.46(0.26)	1.71(0.99)	3.28(2.79)	1.86(1.18)	4.94(8.89)
1.2	0.1	1.99(0.02)	0.24(0.03)	8.63(0.92)	1.22(1.30)	5.52(4.64)	1.51(1.36)	9.00(17.51)
1.2	0.2	2.10(0.07)	0.27(0.02)	7.83(0.80)	0.70(0.48)	5.19(4.74)	1.37(0.94)	1.94(1.16)
1.2	0.3	2.32(0.05)	0.30(0.02)	7.91(0.71)	1.71(1.37)	2.77(3.32)	1.50(0.64)	4.67(9.31)
1.2	0.4	2.48(0.01)	0.32(0.03)	7.73(0.67)	1.34(0.69)	2.71(2.42)	1.70(1.18)	2.50(2.39)
1.2	0.5	2.66(0.06)	0.34(0.04)	7.97(0.70)	1.28(0.59)	2.32(1.08)	1.89(1.27)	9.55(21.16)
1.2	0.6	2.75(0.07)	0.35(0.02)	7.89(0.56)	1.62(1.22)	9.61(22.48)	1.14(0.60)	3.43(2.15)
1.2	0.7	2.79(0.02)	0.37(0.03)	7.58(0.61)	2.12(1.46)	9.80(24.50)	1.65(0.82)	2.40(2.24)
1.2	0.8	2.87(0.07)	0.38(0.03)	7.59(0.63)	1.60(1.31)	14.86(36.81)	1.67(1.44)	4.31(5.32)
1.2	0.9	3.07(0.04)	0.41(0.03)	7.66(0.63)	2.15(1.14)	7.33(17.54)	1.67(0.95)	3.36(3.06)
1.2	1.0	3.17(0.05)	0.43(0.02)	7.46(0.46)	1.52(1.52)	21.41(54.65)	1.14(0.76)	8.50(13.81)

Table 4.11: Results of NEMD simulations in the systems where $\Delta T_{Lang} = 0.2$ ($T_{\text{source}} = 1.4$ and $T_{\text{sink}} = 1.2$) showing the influence of L/S interaction parameters ε_{LS} and σ_{LS} on the structural properties including the contact density ρ_c, depletion layer thickness δ, and peak value S_{max} of the static in-plane structure factor [Eq. (1.10)], and the thermal properties including the contact layer temperature T_c, thermal jump ΔT and thermal slip length L_T [Eq. (1.2)]. Numbers in parentheses are standard deviation values. All values are reported in reduced units.

		Hotter interface						Colder interface					
σ_{LS}	ε_{LS}	ρ_c	δ	S_{max}	T_c	ΔT	L_T	ρ_c	δ	S_{max}	T_c	ΔT	L_T
0.8	0.1	0.973(0.019)	0.599(0.008)	0.213(0.003)	1.366(0.007)	0.028(0.004)	7.023(1.477)	0.949(0.018)	0.619(0.104)	0.324(0.009)	1.235(0.004)	0.033(0.007)	8.382(2.217)
0.8	0.2	1.106(0.019)	0.615(0.008)	0.223(0.002)	1.371(0.006)	0.028(0.005)	6.722(1.352)	1.145(0.017)	0.580(0.007)	0.280(0.003)	1.234(0.003)	0.031(0.004)	7.388(0.910)
0.8	0.3	1.186(0.017)	0.610(0.005)	0.252(0.002)	1.369(0.007)	0.027(0.008)	6.769(2.898)	1.247(0.016)	0.582(0.008)	0.318(0.002)	1.234(0.004)	0.032(0.003)	7.819(1.441)
0.8	0.4	1.248(0.016)	0.608(0.000)	0.278(0.002)	1.369(0.005)	0.025(0.006)	5.712(1.689)	1.317(0.023)	0.566(0.008)	0.362(0.003)	1.231(0.004)	0.025(0.004)	5.657(1.132)
0.8	0.5	1.282(0.023)	0.599(0.008)	0.315(0.002)	1.374(0.004)	0.019(0.005)	4.189(1.259)	1.390(0.023)	0.544(0.005)	0.414(0.004)	1.228(0.005)	0.023(0.005)	4.939(1.131)
0.8	0.6	1.353(0.029)	0.580(0.007)	0.354(0.002)	1.376(0.003)	0.016(0.008)	3.433(1.727)	1.526(0.024)	0.521(0.008)	0.477(0.004)	1.226(0.003)	0.021(0.007)	4.283(1.590)
0.8	0.7	1.418(0.014)	0.563(0.009)	0.404(0.003)	1.379(0.005)	0.017(0.004)	3.413(0.953)	1.660(0.021)	0.499(0.000)	0.539(0.004)	1.224(0.006)	0.019(0.005)	4.009(1.124)
0.8	0.8	1.511(0.026)	0.540(0.008)	0.454(0.004)	1.378(0.003)	0.019(0.006)	4.186(1.465)	1.822(0.030)	0.495(0.008)	0.603(0.002)	1.227(0.005)	0.022(0.006)	4.781(1.573)
0.8	0.9	1.614(0.024)	0.516(0.005)	0.508(0.004)	1.380(0.006)	0.014(0.005)	2.900(1.025)	2.018(0.055)	0.484(0.000)	0.661(0.004)	1.224(0.005)	0.018(0.005)	3.695(1.087)
0.8	1.0	1.771(0.015)	0.505(0.008)	0.567(0.003)	1.382(0.005)	0.013(0.007)	2.745(1.429)	2.196(0.033)	0.480(0.007)	0.715(0.002)	1.225(0.005)	0.018(0.008)	3.780(1.657)
1.0	0.1	1.414(0.033)	0.839(0.007)	0.094(0.001)	1.352(0.004)	0.045(0.006)	15.579(3.516)	1.472(0.016)	0.822(0.008)	0.105(0.002)	1.260(0.004)	0.054(0.004)	18.331(2.761)
1.0	0.2	1.531(0.036)	0.864(0.008)	0.107(0.002)	1.352(0.011)	0.041(0.010)	13.439(4.419)	1.628(0.026)	0.847(0.008)	0.125(0.002)	1.253(0.004)	0.051(0.006)	16.480(3.067)
1.0	0.3	1.638(0.029)	0.874(0.000)	0.126(0.001)	1.358(0.006)	0.036(0.008)	10.760(3.410)	1.742(0.025)	0.858(0.000)	0.148(0.002)	1.251(0.005)	0.046(0.008)	13.431(3.536)
1.0	0.4	1.736(0.029)	0.875(0.005)	0.149(0.002)	1.357(0.006)	0.033(0.006)	8.869(2.284)	1.874(0.031)	0.858(0.000)	0.178(0.002)	1.246(0.004)	0.040(0.004)	10.904(1.702)
1.0	0.5	1.839(0.030)	0.880(0.008)	0.175(0.002)	1.360(0.005)	0.032(0.008)	8.467(2.537)	1.966(0.039)	0.858(0.000)	0.214(0.002)	1.242(0.007)	0.036(0.007)	9.263(2.347)
1.0	0.6	1.925(0.039)	0.877(0.007)	0.203(0.002)	1.364(0.007)	0.028(0.008)	6.953(2.313)	2.111(0.016)	0.858(0.000)	0.255(0.003)	1.242(0.005)	0.033(0.006)	8.112(1.942)
1.0	0.7	2.027(0.033)	0.867(0.008)	0.234(0.002)	1.369(0.005)	0.025(0.004)	5.818(1.220)	2.215(0.041)	0.858(0.000)	0.302(0.004)	1.239(0.004)	0.032(0.006)	7.474(1.686)
1.0	0.8	2.132(0.020)	0.863(0.008)	0.272(0.003)	1.370(0.004)	0.024(0.007)	5.695(2.158)	2.341(0.028)	0.852(0.008)	0.352(0.003)	1.233(0.006)	0.030(0.008)	7.095(2.375)
1.0	0.9	2.238(0.021)	0.858(0.000)	0.310(0.002)	1.373(0.004)	0.023(0.005)	5.094(1.096)	2.529(0.040)	0.842(0.000)	0.412(0.004)	1.229(0.003)	0.025(0.005)	5.542(1.161)
1.0	1.0	2.344(0.021)	0.855(0.007)	0.354(0.003)	1.373(0.006)	0.021(0.005)	4.574(1.118)	2.687(0.025)	0.841(0.005)	0.471(0.003)	1.230(0.005)	0.025(0.006)	5.394(1.397)
1.2	0.1	1.575(0.027)	1.041(0.008)	0.057(0.001)	1.342(0.006)	0.054(0.009)	23.224(6.058)	1.637(0.026)	1.044(0.005)	0.062(0.001)	1.268(0.005)	0.065(0.006)	28.098(4.700)
1.2	0.2	1.710(0.025)	1.076(0.000)	0.065(0.001)	1.343(0.005)	0.053(0.005)	19.911(3.191)	1.800(0.019)	1.076(0.000)	0.073(0.001)	1.261(0.008)	0.056(0.005)	21.058(3.257)
1.2	0.3	1.845(0.023)	1.092(0.000)	0.078(0.001)	1.347(0.006)	0.048(0.007)	16.513(3.461)	1.958(0.023)	1.090(0.005)	0.090(0.001)	1.258(0.004)	0.050(0.005)	17.104(2.421)
1.2	0.4	1.947(0.019)	1.100(0.008)	0.092(0.002)	1.351(0.006)	0.042(0.005)	13.374(2.473)	2.087(0.022)	1.108(0.000)	0.107(0.001)	1.256(0.006)	0.047(0.005)	14.870(2.902)
1.2	0.5	2.079(0.035)	1.108(0.000)	0.108(0.002)	1.355(0.009)	0.041(0.009)	12.002(3.082)	2.224(0.028)	1.103(0.008)	0.128(0.002)	1.251(0.006)	0.043(0.009)	12.753(3.622)
1.2	0.6	2.223(0.031)	1.108(0.000)	0.127(0.002)	1.354(0.006)	0.035(0.007)	10.064(2.430)	2.346(0.042)	1.101(0.008)	0.152(0.002)	1.252(0.004)	0.045(0.005)	12.803(1.907)
1.2	0.7	2.312(0.041)	1.109(0.005)	0.147(0.003)	1.360(0.005)	0.033(0.007)	8.908(2.334)	2.514(0.037)	1.098(0.008)	0.183(0.002)	1.247(0.004)	0.040(0.007)	10.875(2.502)
1.2	0.8	2.434(0.027)	1.108(0.000)	0.168(0.002)	1.363(0.006)	0.032(0.006)	8.517(2.008)	2.651(0.045)	1.097(0.008)	0.212(0.003)	1.244(0.005)	0.038(0.008)	10.158(2.714)
1.2	0.9	2.556(0.036)	1.114(0.008)	0.195(0.002)	1.365(0.005)	0.027(0.005)	6.823(1.653)	2.762(0.025)	1.097(0.008)	0.249(0.002)	1.240(0.004)	0.034(0.007)	8.481(2.092)
1.2	1.0	2.669(0.042)	1.111(0.007)	0.222(0.002)	1.365(0.006)	0.027(0.008)	6.427(2.324)	2.924(0.047)	1.094(0.005)	0.286(0.002)	1.237(0.004)	0.031(0.002)	7.228(0.766)

Table 4.12: Peak frequencies ν_L^* and ν_S^* in the contact layer and first solid layer, respectively, and the ratio ν_S^*/ν_L^* obtained using different values of σ_{LS} and ε_{LS} in the systems where $\Delta T_{Lang} = 0.2$ ($T_{\text{source}} = 1.4$ and $T_{\text{sink}} = 1.2$). Numbers in parentheses are standard deviation values. All values are reported in reduced units.

		Hotter interface			Colder interface		
σ_{LS}	ε_{LS}	ν_L^*	ν_S^*	ν_S^*/ν_L^*	ν_L^*	ν_S^*	ν_S^*/ν_L^*
0.8	0.1	2.397(0.015)	4.960(0.000)	2.070(0.013)	2.390(0.017)	5.010(0.000)	2.096(0.015)
0.8	0.2	1.243(0.006)	4.990(0.000)	4.013(0.019)	1.323(0.023)	5.040(0.000)	3.809(0.066)
0.8	0.3	1.323(0.029)	5.017(0.006)	3.792(0.086)	1.440(0.026)	5.067(0.006)	3.519(0.062)
0.8	0.4	1.390(0.036)	5.037(0.006)	3.625(0.097)	1.450(0.078)	5.093(0.006)	3.519(0.186)
0.8	0.5	1.457(0.038)	5.053(0.006)	3.471(0.085)	1.557(0.032)	5.117(0.006)	3.288(0.065)
0.8	0.6	1.543(0.006)	5.073(0.006)	3.287(0.009)	1.657(0.050)	5.137(0.006)	3.102(0.091)
0.8	0.7	1.577(0.031)	5.100(0.010)	3.236(0.069)	1.663(0.042)	5.167(0.006)	3.108(0.080)
0.8	0.8	1.637(0.040)	5.127(0.006)	3.134(0.077)	1.790(0.035)	5.203(0.006)	2.908(0.052)
0.8	0.9	1.690(0.040)	5.150(0.010)	3.049(0.075)	1.860(0.017)	5.233(0.015)	2.814(0.029)
0.8	1.0	1.753(0.050)	5.177(0.006)	2.954(0.086)	1.940(0.053)	5.273(0.006)	2.719(0.070)
1.0	0.1	1.167(0.032)	5.023(0.012)	4.308(0.127)	1.220(0.062)	5.067(0.006)	4.160(0.205)
1.0	0.2	1.210(0.044)	5.057(0.006)	4.183(0.149)	1.307(0.035)	5.097(0.006)	3.902(0.106)
1.0	0.3	1.287(0.015)	5.073(0.006)	3.943(0.044)	1.367(0.015)	5.123(0.006)	3.749(0.039)
1.0	0.4	1.333(0.046)	5.107(0.006)	3.833(0.138)	1.437(0.006)	5.157(0.006)	3.589(0.010)
1.0	0.5	1.473(0.045)	5.130(0.000)	3.484(0.106)	1.463(0.047)	5.190(0.000)	3.549(0.116)
1.0	0.6	1.500(0.030)	5.160(0.000)	3.441(0.069)	1.573(0.100)	5.227(0.006)	3.331(0.220)
1.0	0.7	1.590(0.036)	5.193(0.006)	3.267(0.072)	1.663(0.029)	5.273(0.012)	3.171(0.059)
1.0	0.8	1.640(0.104)	5.237(0.006)	3.201(0.194)	1.787(0.045)	5.317(0.006)	2.977(0.076)
1.0	0.9	1.657(0.061)	5.283(0.006)	3.192(0.123)	1.860(0.017)	5.363(0.006)	2.884(0.028)
1.0	1.0	1.733(0.023)	5.343(0.012)	3.083(0.038)	1.880(0.036)	5.420(0.017)	2.884(0.064)
1.2	0.1	1.193(0.040)	5.057(0.006)	4.241(0.140)	1.240(0.036)	5.100(0.000)	4.115(0.118)
1.2	0.2	1.250(0.072)	5.087(0.006)	4.078(0.235)	1.323(0.021)	5.120(0.000)	3.870(0.061)
1.2	0.3	1.357(0.015)	5.127(0.012)	3.779(0.051)	1.370(0.046)	5.167(0.012)	3.774(0.127)
1.2	0.4	1.443(0.067)	5.153(0.006)	3.576(0.165)	1.467(0.021)	5.197(0.006)	3.544(0.054)
1.2	0.5	1.493(0.021)	5.193(0.015)	3.478(0.059)	1.560(0.066)	5.243(0.006)	3.365(0.143)
1.2	0.6	1.553(0.032)	5.237(0.006)	3.372(0.067)	1.593(0.021)	5.287(0.012)	3.318(0.039)
1.2	0.7	1.600(0.082)	5.280(0.000)	3.306(0.172)	1.700(0.020)	5.340(0.010)	3.141(0.034)
1.2	0.8	1.690(0.036)	5.333(0.006)	3.157(0.064)	1.787(0.021)	5.400(0.010)	3.023(0.034)
1.2	0.9	1.750(0.046)	5.380(0.000)	3.076(0.081)	1.843(0.070)	5.440(0.000)	2.954(0.113)
1.2	1.0	1.793(0.032)	5.430(0.010)	3.029(0.059)	1.917(0.029)	5.493(0.012)	2.867(0.049)

Chapter 5

CONCLUSION

The objective of this research was to elucidate the fundamental physical mechanism by which the formation of dense fluid layers adjacent to solid surfaces promote conductive thermal transport across the L/S interface. NEMD simulations were conducted to quantify numerous structural and dynamical properties characterizing the contact layer and explore their impact on TBR. A brief description of the significant results of each project are summarized below.

In Chapter 2, we simultaneously changed the L/S interaction energy and the orientation of the crystal lattice comprising the solid substrates to alter both the density and local ordering of liquid particles in the contact layer. From our findings of the enhanced thermal transfer across the [011] FCC facet, we identify two distinguishing features of the contact layer which strongly correlate with smaller thermal slip lengths. Stronger registration between the contact layer and adjacent crystal, as quantified by the maximum of the in-plane structure factor, contributes to longer range ordering of liquid particles commensurate with the periodic solid surface potential. A surface potential with strong anisotropy is especially advantageous. For the [011] case examined, the motion of particles in the contact layer beyond the ballistic regime is suppressed by very large and rather wide repulsive barriers along one axis. The motion is also severely hindered by the presence of other particles centered about attractive basins periodically aligned along the perpendicular axis. We refer to such strong in-plane localization as 2D caged motion. Results of the self-intermediate scattering function confirm that smaller thermal slip lengths correlate positively with larger values of the non-ergodicity parameter. Hindered motion in-plane and the correlated exit of particles from the contact layer due to strong alignment when occupying that layer leads to more rapid and more efficient escape of particles out-of-plane, which ultimately funnels thermal energy more effectively from warmer to cooler regions.

In Chapter 3, we used the same system from Chapter 2 to analyze thermodynamic properties in the frequency domain to analyze vibrational dynamics that plays a crucial role in the interfacial thermal transport. The convective energy exchange between the liquid and solid particles were quantified by the spectral heat flux which was decomposed into in-plane (i.e., along the x- and y-axes) and out-of-plane (i.e., along the z-axis) to quantitatively compare thermal contributions along the respective directions. The results indicated that the in-plane component grows significantly by increasing the temperature and/or the interaction energy between the liquid and solid particles, whereas the out-of-plane component is insensitive to these changes. Furthermore, the in-plane component was observed to be largest across the [011] facet (i.e., the facet with the lowest TBR among the three facet orientations), suggesting that thermal exchange along the x- and y-axes is a contributing factor in the

interfacial thermal transport. The peak analysis of the DOS distributions indicated that dominant frequencies of the normal modes in the contact layer approach those of the first solid layers upon improving the surface commensurability between the liquid and solid layers, e.g., by enhancing the L/S interaction strength. Finally, we constructed a master curve for the thermal slip length requiring only two variables: the ratio of dominant frequencies in the first solid and liquid layers and the contact layer temperature.

In Chapter 4, the length and energy parameters characterizing the L/S interaction and the macroscopic thermal gradients applied to the system were systematically varied to investigate a correlation between TBR and local ordering of liquid particles. We demonstrated that common structural properties such as the contact density and depletion layer thickness are not suitable for describing the dependence of TBR on the contact layer since neither quantity cannot reliably nor uniquely predict the thermal jump or TBR by itself. Instead, the results of this study identify the in-plane liquid ordering within the contact layer as one of the key factors governing the magnitude of TBR across the L/S interface. We constructed a master curve relation that predicts thermal slip length based on the peak value of the static structure factor and the local temperature in the contact layer, implying that improved in-plane liquid ordering is the primary factor that lowers TBR across the L/S interface. Furthermore, it was shown that higher in-plane ordering in the contact layer reduces the ratio of dominant frequencies in the first solid and liquid layers. From this observation, we constructed another master curve relation which gives the thermal slip length in terms of the peak frequency ratio, contact layer temperature, and L/S repulsive distance (i.e., the length scale of L/S interaction). The functional form of this master curve closely resembles that obtained in Chapter 3, suggesting that the peak frequency ratio (i.e., the acoustic mismatch between the solid and liquid layers) is a crucially important factor that controls heat flux across the L/S interface.

The fundamental nature of this study suggests broader applicability of these findings and a paradigm for designing interfacial properties which can maximize thermal transport across a L/S interface.

BIBLIOGRAPHY

[1] D. Alexeev, J. Chen, J. H. Walther, K. P. Giapis, P. Angelikopoulos, and P. Koumoutsakos. "Kapitza resistance between few–layer graphene and water: Liquid layering effects." In: *Nano Lett.* 15.9 (2015), pp. 5744–5749 (cit. on pp. 5, 56, 71).

[2] S. Alosious, S. K. Kannam, S. P. Sethian, and B. D. Todd. "Prediction of Kapitza resistance at fluid–solid interfaces." In: *J. Chem. Phys.* 151 (2019), p. 194502 (cit. on pp. 45, 71).

[3] G. Balasubramanian, S. Banerjee, and I. K. Puri. "Unsteady nanoscale thermal transport across a solid–fluid interface." In: 104 (2008), p. 064306 (cit. on p. 4).

[4] M. Barisik and A. Beskok. "Temperature dependence of thermal resistance at the water/silicon interface." In: *Int. J. Therm. Sci* 77 (2014), pp. 47–54 (cit. on pp. 19, 24).

[5] J.-L. Barrat and F. Chiaruttini. "Kapitza resistance at the liquid–solid interface." In: *Mol. Phys.* 101 (2003), pp. 1605–1610 (cit. on pp. 4, 24).

[6] C. S. Barrett and L. Meyer. "X–ray diffraction of solid argon." In: *J. Chem. Phys.* 41 (1964), pp. 1078–1081 (cit. on p. 8).

[7] P. H. Berens, D. H. J. Mackay, G. M. White, and K. R. Wilson. "Thermodynamics and quantum corrections from molecular dynamics for liquid water." In: *J. Chem. Phys.* 79 (1983), pp. 2375–2389 (cit. on p. 15).

[8] D. Bolmatov, V. V. Brazhkin, and Trachenko K. "The phonon theory of liquid thermodynamics." In: *Sci. Rep.* 2.421 (2012) (cit. on p. 3).

[9] B.-Y. Cao, J.-H. Zou, G.-J. Hu, and G.-X. Cao. "Enhanced thermal transport across multilayer graphene and water by interlayer functionalization." In: *Appl. Phys. Lett.* 112 (2018), p. 041603 (cit. on p. 5).

[10] M. E. Caplan, A. Giri, and P. E. Hopkins. "Analytical model for the effects of wetting on thermal boundary conductance across solid/classical liquid interfaces." In: *J. Chem. Phys.* 140 (2014), p. 154701 (cit. on pp. 45, 50, 71).

[11] J. Chen, G. Zhang, and B. Li. "Tunable thermal conductivity of $Si_{1-x}Ge_x$ nanowires." In: *Appl. Phys. Lett.* 95 (2009). For the definition of the spectral overlap, refer to (1) in page 3., p. 073117 (cit. on p. 56).

[12] D. P. Dean and J. N. Kushick. "On the role of attractive forces in the cage effect in simple liquids." In: *J. Chem. Phys.* 76 (1982), pp. 619–621 (cit. on p. 38).

[13] Y. Endo and Endo. H. "Microscopic mechanism of the cage effect in simple liquids." In: *Phys. Lett.* 95A (1983), pp. 92–94 (cit. on p. 38).

[14] J. Frenkel. *Kinetic theory of liquids*. Oxford Univ. Press, 1947 (cit. on p. 50).

[15] M. Fuchs, W. Götze, and M. R. Mayr. "Asymptotic laws for tagged-particle motion in glassy systems." In: *Phys. Rev. E* 58 (1998), pp. 3384–3399 (cit. on p. 37).

[16] J. Gao, W. D. Luedtke, and U. Landman. "Layering transitions and dynamics of confined liquid films." In: *Phys. Rev. Lett.* 79.4 (1997), pp. 705–708 (cit. on pp. 3, 19).

[17] S. Ge and M. Chen. "Temperature dependence of thermal resistance at a solid/liquid interface." In: *Mol. Phys.* 111 (2013), pp. 903–908 (cit. on pp. 4, 25, 45, 71).

[18] S. Ge and M. Chen. "Vibrational coupling and Kapitza resistance at a –liquid interface." In: *Int. J. Thermophys.* 34 (2013), pp. 64–77 (cit. on pp. 5, 56).

[19] K. Gordiz and A. Henry. "Examining the effects of stiffness and mass difference on the thermal interface conductance between Lennard–Jones solids." In: *Sci. Rep.* 5 (2015), p. 18361 (cit. on p. 60).

[20] A. Hamasaiid, M.S. Dargusch, T. Loulou, and G. Dour. "A predictive model for the thermal contact resistance at liquid–solid interfaces: Analytical developments and validation." In: *Int. J. Therm. Sci* 50 (2011), pp. 1445–1459 (cit. on pp. 45, 71).

[21] H. Han, S. Mérabia, and F. Müller-Plathe. "Thermal transport at solid–liquid interfaces: High pressure facilitates heat flow through nonlocal liquid structuring." In: *J. Phys. Chem. Lett.* 8.9 (2017), pp. 1946–1951 (cit. on pp. 4, 10, 19, 25, 45, 46, 71).

[22] M. Han. "Effect of liquid bulk density on thermal resistance at a liquid–solid interface." In: *J. Mech. Sci. Tech* 25.1 (2011), pp. 37–42 (cit. on pp. 45, 71).

[23] M. R. Hasan, T. Q. Vo, and B.H. Kim. "Manipulating thermal resistance at the solid–fluid interface through monolayer deposition." In: *RSC Adv.* 9 (2019), pp. 4948–4956 (cit. on pp. 56, 58).

[24] E. Helfand and S. A. Rice. "Principle of corresponding states for transport properties." In: *J. Chem. Phys.* 32 (2016), pp. 1642–1644 (cit. on p. 3).

[25] J. R. Henderson and F. van Swol. "On the interface between a fluid and a planar wall: Theory and simulations of a hard sphere fluid at a hard wall." In: *Mol. Phys.* 51.4 (1984), pp. 991–1010 (cit. on pp. 3, 19).

[26] E. J. Hinch. "Application of the Langevin equation to fluid suspensions." In: 72 (1975), pp. 495–511 (cit. on p. 36).

[27] B. L. Holian and D. J. Evans. "Shear viscosities away from the melting line: A comparison of equilibrium and nonequilibrium molecular dynamics." In: *J. Chem. Phys.* 78 (1983), pp. 5147–5150 (cit. on pp. xiii, 8, 46).

[28] W. G. Hoover. "Canonical dynamics: Equilibrium phase–space distributions." In: *Phys. Rev. A* 31 (1985), pp. 1695–1697 (cit. on p. 10).

[29] S. W. Hung, G. Kikugawa, and J. Shiomi. "Mechanism of temperature dependent thermal transport across the interface between self-assembled monolayer and water." In: *J. Phys. Chem. C* 120.47 (2016), pp. 26678–26685 (cit. on pp. 4, 25, 56).

[30] P. L. Kapitza. "Heat transfer and superfluidity of helium II." In: *Phys. Rev.* 60 (1941), pp. 354–355 (cit. on p. 1).

[31] I. M. Khalatnikov. *An Introduction to the Theory of Superfludity*. CRC Press. English translation of Russian edition by P. C. Hohenberg. Boca Raton, FL: Taylor & Francis, 2018 (cit. on p. 25).

[32] I. M. Khalatnikov. “TEPLOOBMEN MEZHDU TVERDYM TELOM I GELIEM-II.” In: *Zh. Eksp. Teor. Fiz.* 22.6 (1952), pp. 687–704 (cit. on pp. 4, 56).

[33] B. H. Kim, A. Beskok, and T. Cagin. “Molecular dynamics simulations of thermal resistance at the liquid-solid interface.” In: *J. Chem. Phys.* 129 (2008), p. 174701 (cit. on pp. 4, 58).

[34] W. Kob. “Computer simulations of supercooled liquids and glasses.” In: *J. Phys.: Condens. Matter* 11 (1999), R85–R115 (cit. on p. 37).

[35] W. Kob and H. C. Andersen. “Scaling behavior in the β–relaxation regime of a supercooled Lennard-Jones mixture.” In: *Phys. Rev. Lett.* 73 (1994), pp. 1376–1379 (cit. on pp. 37, 41).

[36] P. Langevin. “Sur la théorie du mouvement Brownien.” In: *C.R. Acad. Sci. Paris* 146 (1908), pp. 530–533 (cit. on p. 35).

[37] Z. Liang and P. Keblinski. “Finite–size effects on molecular dynamics interfacial thermal–resistance predictions.” In: *Phys. Rev. B* 90 (2014), p. 075411 (cit. on pp. 10, 46).

[38] S. T. Lin, M. Blanco, and W. A. Goddard. “The two-phase model for calculating thermodynamic properties of liquids from molecular dynamics: Validation for the phase diagram of Lennard-Jones fluids.” In: *J. Chem. Phys.* 119 (2003), pp. 11792–11805 (cit. on p. 56).

[39] L. L. Liou, B. Bayraktaroglu, and C. I. Huang. “Theoretical thermal runaway analysis of heterojunction bipolar transistors: Junction temperature rise threshold.” In: *Solid–State Electron.* 39.1 (1996), pp. 165–172 (cit. on p. 1).

[40] V. Lubchenko and P. G. Wolynes. “Theory of structural glasses and supercooled liquids.” In: *Annu. Rev. Phys. Chem* 58 (2007), pp. 235–266 (cit. on p. 46).

[41] S. Maruyama and T. Kimura. “A study on thermal resistance over a solid–liquid interface by the molecular dynamics method.” In: *Thermal Sci. Eng.* 7.1 (1999), pp. 63–68 (cit. on pp. 4, 19).

[42] S. Maruyama and T. Kimura. “Intermolecular energy transfer at a solid–liquid interface.” In: *Micro. Thermophys. Eng.* 4 (2000), pp. 189–196 (cit. on p. 4).

[43] S. Maruyama and T. Kimura. “Liquid droplet in contact with a solid surface.” In: *Micro. Thermophys. Eng.* 2 (1998), pp. 49–62 (cit. on pp. 4, 19).

[44] S. Matsumoto. “Molecular dynamics simulation of a liquid droplet on a solid surface.” In: *J. Jap. Soc. Tribologists* 42.2 (1997), pp. 93–98 (cit. on p. 4).

[45] A. Michels, H.U.B. Wijker, and H.K. Wijker. “Isotherms of argon between 0°C and 150°C and pressures up to 2900 atmospheres.” In: *Physica* XV.7 (1949), pp. 627–633 (cit. on pp. xiii, 8).

[46] S. Y. Misyura. “Dependence of wettability of microtextured wall on the heat and mass transfer: Simple estimates for convection and heat transfer.” In: *Int. J. Therm. Sci* 170 (2020), p. 105353 (cit. on pp. 45, 71).

[47] A. K. M. M. Morshed, T.C. Paul, and J. A. Khan. “Atomistic simulation of temperature dependent thermal transport across nanoconfined liquid.” In: *Physica E* 47 (2013), pp. 246–251 (cit. on p. 4).

[48] R. D. Mountain and D. Thirumalai. “Relationship between the fluctuation metric and the non-ergodicity parameter: incoherent scattering function.” In: *Physica A* 192 (1993), pp. 543–549 (cit. on p. 41).

[49] S. Murad and I. K. Puri. “Molecular simulation of thermal transport across hydrophilic interfaces.” In: *Chem. Phys. Lett.* 467 (2008), pp. 110–113 (cit. on pp. 4, 45, 71).

[50] S. Murad and I. K. Puri. “Thermal transport across nanoscale solid–fluid interfaces.” In: *Appl. Phys. Lett.* 92.13 (2008), p. 133105 (cit. on pp. 4, 10, 45, 71).

[51] T. Ohara and D. Torii. “Molecular dynamics study of thermal phenomena in an ultrathin liquid film sheared between solid surfaces: The influence of the crystal plane on energy and momentum transfer at solid-liquid interfaces.” In: *J. Chem. Phys.* 122 (2005), p. 214717 (cit. on p. 4).

[52] G. Parsafar, F. Kermanpour, and B. Najafi. “Prediction of the temperature and density dependencies of the parameters of the average effective pair potential using only the LIR equation of state.” In: *J. Chem. Phys. B* 103 (1999), pp. 7287–7292 (cit. on p. 44).

[53] A. Pham, M. Barisik, and B. Kim. “Pressure dependence of Kapitza resistance at gold/water and silicon/water interfaces.” In: *J. Chem. Phys.* 139.24 (2013), p. 244702 (cit. on pp. 4, 45, 71).

[54] S. Plimpton. “Fast parallel algorithms for short–range molecular dynamics.” In: *J. Comput. Phys.* 117 (1995), pp. 1–19 (cit. on p. 9).

[55] G. L. Pollack. “Kapitza resistance.” In: *Rev. Mod. Phys.* 41 (1969), pp. 48–81 (cit. on p. 25).

[56] R. S. Prasher. “Surface chemistry and characteristics based model for the thermal contact resistance of fluidic interstitial thermal interface materials.” In: *J. Heat Transfer* 123 (2001), pp. 969–975 (cit. on pp. 45, 71).

[57] N. V. Priezjev, A. A. Darhuber, and S. M. Troian. “Slip behavior in liquid films on surfaces of patterned wettability: Comparison between continuum and molecular dynamics.” In: *Phys. Rev. E* 71 (2005), p. 041608 (cit. on pp. 6, 19, 62).

[58] A. Rahman. “Correlations in the motion of atoms in liquid argon.” In: *Phys. Rev.* 136 (1964), A405–411 (cit. on p. 15).

[59] B. Ramos-Alvarado, S. Kumar, and G. P. Peterson. “Solid–liquid thermal transport and its relationship with wettability and the interfacial liquid structure.” In: *J. Phys. Chem. Lett.* 7 (2016), pp. 3497–3501 (cit. on pp. 4, 25, 45, 71).

[60] K. Sääskilahti, J. Oksanen, J. Tulkki, and S Volz. “Frequency-dependent phonon mean free path in carbon nanotubes from nonequilibrium molecular dynamics.” In: *Phys. Rev. B* 91 (2015), p. 115426 (cit. on pp. 15, 16).

[61] K. Sääskilahti, J. Oksanen, J. Tulkki, and S Volz. “Role of anharmonic phonon scattering in the spectrally decomposed thermal conductance at planar interfaces.” In: *Phys. Rev. B* 90 (2014), p. 134312 (cit. on pp. 15, 60).

[62] K. Sääskilahti, J. Oksanen, J. Tulkki, and S. Volz. “Spectral mapping of heat transfer mechanisms at liquid-solid interfaces.” In: *Phys. Rev. E* 93 (2016), p. 052141 (cit. on pp. 15, 50).

[63] S. Sadasivam, N. Ye, J. P. Feser, J. Charles, K. Miao, T. Kubis, and T. S. Fisher. "Thermal transport across metal silicide–silicon interfaces: First–principles calculations and Green's function transport simulations." In: *Phys. Rev. B* 95 (2017). For discussion on inelastic contributions to interfacial thermal conductance, see pgs 12–13., p. 085310 (cit. on p. 60).

[64] T. Schneider and E. Stoll. "Molecular–dynamics study of a three–dimensional one–component model for distortive phase transitions." In: *Phys. Rev. B* 17 (1978), pp. 1302–1322 (cit. on p. 10).

[65] N. Shenogina, R. Godawat, P. Keblinski, and S. Garde. "How wetting and adhesion affect thermal conductance of a range of hydrophobic to hydrophilic aqueous interfaces." In: *Phys. Rev. Lett.* 102 (2009), p. 156101 (cit. on pp. 45, 71).

[66] M. Shibahara and K. Takeuchi. "A molecular dynamics study on the effects of nanostructural clearances on thermal resistance at a Lennard-Jones liquid-solid interface." In: *J. Thermal Sci. Tech.* (2011), pp. 9–20 (cit. on pp. 45, 71).

[67] S. A. Somers and H. T. Davis. "Microscopic dynamics of fluids confined between smooth and atomically structured solid surfaces." In: *J. Chem. Phys.* 96 (1992), pp. 5389–5407 (cit. on pp. 3, 19).

[68] R. J. Stevens, L. V. Zhigilei, and P. M. Norris. "Effects of temperature and disorder on thermal boundary conductance at solid–solid interfaces: Nonequilibrium molecular dynamics simulations." In: *Int. J. Mech. Sci.* 50.19 (2007), pp. 3977–3989 (cit. on pp. 8, 10, 46).

[69] E. T. Swartz and R. O. Pohl. "Thermal boundary resistance." In: *Rev. Mod. Phys.* 61.3 (1989), pp. 605–668 (cit. on pp. 2, 4, 50, 56, 60).

[70] E. T. Swartz and R. O. Pohl. "Thermal resistance at interfaces." In: *Appl. Phys. Lett.* 51.26 (1987), pp. 2200–2202 (cit. on p. 2).

[71] A. Tenenbaum, G. Ciccotti, and R. Gallico. "Stationary nonequilibrium states by molecular dynamics. Fourier's law." In: *Phys. Rev. A* 25.5 (1982), pp. 2778–2787 (cit. on p. 3).

[72] M. Thol, G. Rutkai, A. Köster, R. Lustig, R. Span, and J. Vrabec. "Equation of state for the Lennard-Jones fluid." In: *J. Phys. Chem. Ref. Data* 45.2 (2016), p. 023101 (cit. on p. 8).

[73] A. P. Thompson, H. M. Aktulga, R. Berger, D. S. Bolintineanu, W. M. Brown, P. S. Crozier, P. J. intVelde, A. Kohlmeyer, S. G. Moore, T. D. Nguyen, R. Shan, M. J. Stevens, J. Tranchida, C. Trott, and S. J. Plimpton. "LAMMPS – A flexible simulation tool for particle–based materials modeling at the atomic, meso, and continuum scales." In: *Comp. Phys. Comm.* 271 (2022), p. 108171 (cit. on p. 9).

[74] P. A. Thompson and M. O. Robbins. "Shear flow near solids: Epitaxial rrder and flow boundary conditions." In: *Phys. Rev. A* 41.12 (1990), pp. 6830–6837 (cit. on pp. 6, 19, 62, 68).

[75] Z. Tian, K. Esfarjani, and G. Chen. "Enhancing phonon transmission across a Si/Ge interface by atomic roughness: first-principles study with the Green's function method." In: *Phys. Rev. B* 86 (2012), p. 235304 (cit. on p. 5).

[76] B. D. Todd and D. J. Evans. “The heat flux vector for highly inhomogeneous nonequilibrium fluids in very narrow pores.” In: *J. Chem. Phys.* 103.22 (1995), pp. 9804–9809 (cit. on p. 19).

[77] D. Torii, T. Ohara, and K. Ishida. “Molecular-scale mechanism of thermal resistance at the solid–liquid interfaces: Influence of interaction parameters between solid and liquid molecules.” In: *J. Heat Transfer* 132 (2010), p. 012402 (cit. on p. 4).

[78] S. Toxvaerd. “The structure and thermodynamics of a solid–fluid interface.” In: *J. Chem. Phys.* 74 (1981), p. 1998 (cit. on pp. 19, 21).

[79] D. B. Tuckerman and R. F. W. Pease. “High-performance heat sinking for VLSI.” In: *IEEE Electron Device Lett.* 2.5 (1981), pp. 126–129 (cit. on p. 2).

[80] E. Velasco and P. Tarazona. “Phase transitions at solid–fluid interfaces: Theoretical description of the transverse structure.” In: *Surf. Sci.* 251/252 (1991), pp. 628–634 (cit. on p. 19).

[81] L. Verlet. “Computer “experiments” on classical fluids. I. Thermodynamical properties of Lennard-Jones molecules.” In: *Phys. Rev.* 159.1 (1967), pp. 98–103 (cit. on pp. xiii, 8, 9).

[82] V. Vladimirsky and Y. A. Terletzky. “Hydrodynamical theory of translational Brownian motion.” In: *Zh. Eksp. Teor. Fiz.* 15 (1945), pp. 258–263 (cit. on p. 36).

[83] T. Q. Vo and B. H. Kim. “Transport phenomena of water in molecular fluidic channels.” In: *Sci. Rep.* 6 (2016), p. 33881 (cit. on pp. 5, 56).

[84] M. Vuorio. “Role of wetting and nanoscale roughness on thermal conductance at liquid–solid interface.” In: *Appl. Phys. Lett.* 99 (2011), p. 073112 (cit. on p. 4).

[85] G. Wahnström. “Molecular–dynamics study of a supercooled two-component Lennard–Jones system.” In: *Phys. Rev. A* 44 (1991), pp. 3752–3764 (cit. on p. 41).

[86] Y. Wang, H. F. Zhan, Y. Xiang, C. Yang, C. M. Wang, and Y. Y. Zhang. “Effect of Covalent functionalization on thermal transport across graphene-polymer interfaces.” In: *J. Phys. Chem. C* 119 (2015), pp. 12731–12738 (cit. on p. 5).

[87] Z. Wang. “A molecular dynamics study of the thermal transport in silicon/germanium nanostructures: from cross-plane to in-plane.” In: *Mater. Today. Commun.* 22 (2020), p. 100822 (cit. on p. 5).

[88] R. J. Warzoha, A. A. Wilson, B. F. Donovan, A. Clark, X. Cheng, L. An, E. Lee, X. Liu, and G. Feng. “Confined transducer geometries to enhance sensitivity to thermal boundary conductance in frequency–domain thermoreflectance measurements.” In: *ASME 2021 International Technical Conference and Exhibition on Packaging and Integration of Electronic and Photonic Microsystems*. ASME. Virtual, Oct. 2021, IPACK2021–66842 (cit. on p. 3).

[89] L. Xue, P. Keblinski, S. R. Phillpot, S. U.-S. Choi, and J. A. Eastman. “Effect of liquid layering at the liquid–solid interface on thermal transport.” In: *Int. J. Mech. Sci.* 47 (2004), pp. 4277–4284 (cit. on p. 46).

[90] L. Xue, P. Keblinski, S. R. Phillpot, S. U.-S. Choi, and J. A. Eastman. “Two regimes of thermal resistance at a liquid–solid interface.” In: *J. Chem. Phys.* 118 (2003), pp. 337–339 (cit. on pp. 4, 24).

[91] K. Yu, R. Enright, and D. McCloskey. “Quantifying interfacial thermal conductance at solid–liquid interfaces using frequency-domain thermoreflectance and analytical methods.” In: *21st IEEE Intersociety Conference on Thermal and Thermomechanical Phenomena in Electronic Systems (iTherm)*. IEEE. San Diego, CA, 2022, pp. 1–6 (cit. on p. 3).

[92] J. Zhang, F. Leroy, and F. Müller-Plathe. “Evaporation of nanodroplets on heated substrates: A molecular dynamics simulation study.” In: *Langmuir* 29 (2013), pp. 9770–978 (cit. on pp. 45, 71).

[93] T. Zhou, H. K. Chilukoti, Z. Wu, and F. Müller-Plathe. “Effect of defects on the interfacial thermal conductance between n-heneicosane in solid and liquid phases and a graphene monolayer.” In: *J. Phys. Chem. C* 125 (2021), pp. 14149–14162 (cit. on p. 5).